

Copyright

by

Madisen A. Holbrook

2021

**The Dissertation Committee for Madisen Holbrook Certifies that this is the approved
version of the following Dissertation:**

**Engineering Two-Dimensional Materials: Discovery, Defects, and
Environment**

Committee:

Chih-Kang (Ken) Shih, Supervisor

Xiaoqin (Elaine) Li

Keji Lai

Li Shi

**Engineering Two-Dimensional Materials: Discovery, Defects, and
Environment**

by

Madisen A. Holbrook

Dissertation

Presented to the Faculty of the Graduate School of

The University of Texas at Austin

in Partial Fulfillment

of the Requirements

for the Degree of

Doctor of Philosophy

The University of Texas at Austin

May 2021

Dedication

For my mother and Franki,
two brilliant women who always believed in me.

Acknowledgements

The last seven years have truly tested my limits, and I wouldn't have had the strength to get through the challenges without the support of many people; as they say, it takes a village. First I would like to thank my mother, not only for setting example for me to look up to by obtaining a higher education as woman in my family, but for pushing me to succeed as well. I am grateful for the innumerable conversations where she has patiently listened when I have been at my lowest, but she always lifted me up and reminded me that everything works out with time. Her deep love and sacrifices throughout the years are the foundation that this dissertation is built upon. I also want to thank the rest of my family for their support, especially my "little" brothers Alex and Garret, and my cousin Michael, who have listened to me ramble on about physics for years without complaint. They truly see and understand all sides of me, and always put a smile on my face. Being far away from my family through the years has been an immense sacrifice, and I am grateful for their understanding and endless encouragement.

I also want to acknowledge my advisor, Dr. Ken Shih, for shaping me into a real scientist from the sloppy lump of clay he was given. From the first day I walked into his office announcing that I wanted to build an STM, he has given me the freedom to direct my scientific exploration, while holding me accountable to finish what I start. Although it wasn't always easy, his high expectations pushed me to achieve more than I thought possible, shown me my strengths and weaknesses, and made me not only a better scientist, but a better person. His passion for physics and creativity have set the standard for the rest of my career, and I am extremely grateful to have had him as a mentor.

I next want to thank my lab mates past and present for their help and support. I would like to give special thanks to Dr. Hui Zhang and Dr. Jungdae Kim for their patience

in teaching me the skills I needed to be a successful researcher. I also want to thank my lab sisters, Mengke Liu, Hyunsue Kim, and Lisa Frammolino for helping me create a fun, productive, and supportive environment where we have shared many laughs and had stimulating physics conversations, even when the work has been tough. I want to thank my other lab mates that I have made the many hours in the lab easier through helping hands, kind words, and good laughs: Dr. Alex Johnson, Dr. Hyoungdo Nam, Dr. Yuxuan Chen, Dr. Ping-Hsiang Su, Dr. Chengdong Zhang, Dr. Wei-Ting Hsu, Dr. Chunyuan Wang, Woojoo Lee, Yanxing Li, and Jia Yu.

I extend my deep gratitude to all of my collaborators who made this work possible, including Dr. Feliciano Giustino, Dr. Mei-Yin Chou, and Dr. Allan McDonald for their theoretical work, and Dr. Wen Hao Zhang, Dr. Wei-Ting Hsu, and Dr. Li-Syuan Lu for sample preparation, and Dr. Philipp Ebert for helpful conversations. A special thanks to Dr. Chao Lei for the time and effort he invested in the beautiful theoretical calculations for my defect project. Thank you to Dr. Hui Zhang, my close collaborator and mentor on the BeO project, for his unwavering confidence in my ability to figure out the science behind this project and establishing the growth process. Thanks to Dr. Yuxuan Chen for providing the ground-work for the MoSe₂/hBN/Ru intercalation project, as his early work would later evolve into this project.

I would also like to thank the support staff of the physics department, including the cryogenics, machine, and electronic shops. They have all saved my experiments on numerous occasions, but deep thanks to Allan Schoeder, Kenny Schneider, and Jack Clifford for their patience and kindness. I would also like to thank the UT MRSEC for funding my research over almost the entirety of my degree, and all of the professional development and research opportunities I was. I would also like to thank my committee members, Dr. Elaine Li, Dr. Li Shi, and Dr. Keji Lai for their valuable time.

Finally, I would like to thank my friends from all facets of my life who have all provided immense support throughout the years on my physics journey. Thanks to all of my close friends in the physics department, especially Dr. Max Porter and Dr. James Oliver for listening and lifting me up over pints at Crown after rough days in the lab. My deepest gratitude for my best friends Candace, Leslie, and Michael, for the emotional support you have provided me over the more than twenty years of friendship, and for remaining close as I have chased my dreams far away. Finally, my deepest thanks to Franki Aymond, one of the first friends I ever made at UT, whose kind heart and brilliant mind will continue to inspire me to be the best researcher and person I can be. Her passing was an extreme loss to the physics community, but I will continue our shared passion for equality in physics in her memory. Rest in peace sweet Franki, you are sorely missed.

MADISEN HOLBROOK

Abstract

Engineering Two-Dimensional Materials: Discovery, Defects, and Environment

Madisen A. Holbrook, Ph.D.

The University of Texas at Austin, 2021

Supervisor: Chih-Kang (Ken) Shih

The discovery of graphene and its unprecedented properties inspired an extraordinary increase in research progress, launching an era of two-dimensional (2D) electronic materials. These stable crystalline atomic layers enable the design of ultrathin 2D devices by combining different 2D materials as the foundational components. In order to control the properties of these devices, materials with a variety of electronic properties must be available. In this dissertation, we explore three distinct paths to achieve this goal: expanding the library of 2D materials, post synthesis defect engineering, and proximity engineering of the electrostatic environment. First, we report the MBE synthesis and STM/S characterization of a new 2D insulator, honeycomb structure BeO. In addition to determining the atomic structure and density of states, we used moiré pattern analysis to demonstrate the high crystallinity of the BeO and determined the work function modulation across the moiré pattern. We illustrate that the scalable growth, weak substrate interactions, and long-range crystallinity make honeycomb BeO an attractive candidate for future technological applications. The next focus of this work was defect engineering of monolayer WS₂ by UHV annealing. A high concentration of S vacancies was generated by

UHV annealing of the WS₂, leading to S vacancy defect-defect coupling. Using STM/S we determined that the interaction of nearby S vacancies leads to an increase of deep in-gap states for different divacancy geometries. This indicates that vacancy engineering can be a useful tool to controllably manipulate 2D material electronic properties. Finally, we demonstrate the creation of a nanoscale planar p-n junction within a single monolayer of MoSe₂ by modulating the electronic properties of the underlying substrate. By intercalating Se at the interface of the hBN/Ru substrate, the hBN becomes decoupled from the Ru, changing its conductivity and work function. We find that this change in the electronic landscape tunes the band gap of the overlying MoSe₂, by screening and shifting the MoSe₂ work function. Thus, this dissertation shines a light on the vast opportunities 2D materials provide for exploration of novel approaches to materials engineering, and demonstrates a tool set for manipulating the electronic properties of these fascinating materials.

Table of Contents

| | |
|--|------|
| List of Figures | xiii |
| Chapter 1: Introduction and Motivation | 1 |
| Chapter 2: Scanning Tunneling Microscopy Background..... | 3 |
| 2.1 History | 3 |
| 2.2 Tunneling Theory | 4 |
| 2.2.1 1D Barrier Model..... | 4 |
| 2.2.2 Bardeen Tunneling Model | 6 |
| 2.2.3 Tersoff-Hamann Approximation | 8 |
| 2.3 STM Operation | 10 |
| 2.3.1 Constant Current Imaging - Topography..... | 12 |
| 2.3.2 I-V Tunneling Spectroscopy..... | 12 |
| 2.3.3 Z-V Field Emission Resonance Spectroscopy..... | 14 |
| 2.4 Summary..... | 15 |
| Chapter 3: Epitaxial Growth of Novel Two-Dimensional Insulator Monolayer Honeycomb BeO..... | 16 |
| 3.1 Introduction and Motivation | 16 |
| 3.2 Beryllium Oxide Background..... | 17 |
| 3.3 MBE Synthesis of Honeycomb BeO | 19 |
| 3.3.1 Determination of the BeO Growth Rate | 20 |
| 3.4 Monolayer Honeycomb BeO Crystal Structure..... | 23 |
| 3.4.1 BeO Monolayer..... | 23 |
| 3.4.2 Honeycomb BeO Atomic Structure..... | 26 |
| 3.4.3 Long Range Crystallinity..... | 30 |

| | |
|---|----|
| 3.5 STM/S characterization of Honeycomb BeO Electronic Properties | 32 |
| 3.5.1 I-V Spectroscopy: BeO DOS and Interaction with Ag(111) Substrate | 32 |
| 3.5.2 Z-V Spectroscopy: Moiré Modulation of Work Function | 33 |
| 3.6 First Principles Calculation of BeO/Ag(111) Heterostructure | 35 |
| 3.7 Conclusion and Future Outlook..... | 38 |
| Chapter 4: Sulfur Vacancy Defect-Defect Interactions in Monolayer WS ₂ | 40 |
| 4.1 Introduction and Background | 40 |
| 4.2 WS ₂ UHV Thermal Annealing | 43 |
| 4.3 WS ₂ Defect Characterization | 47 |
| 4.3.1 Defect Geometry..... | 48 |
| 4.3.2 Defect Electronic Properties | 50 |
| 4.4 Understanding TMD Chalcogen Vacancy Electronic Structure..... | 52 |
| 4.4.1 Crystal Field Theory | 52 |
| 4.4.2 TMD Band Structure | 53 |
| 4.4.3 Spin-Orbit Coupling | 54 |
| 4.4.4 Chalcogen Vacancy In-Gap States | 55 |
| 4.5 WS ₂ Sulfur Vacancy Defect-Defect Interactions..... | 58 |
| 4.5.1 Column Divacancy | 59 |
| 4.5.2 Lateral Divacancy | 64 |
| 4.5.3 Vacancy Aggregate..... | 66 |
| 4.5.4 Line Defect | 69 |
| 4.6 First Principles Calculations of Defect-Defect Interaction..... | 73 |
| 4.7 Conclusion | 79 |

| | |
|---|-----|
| Chapter 5: Tailoring the Lateral Potential Landscape of 2D Electronic Materials at the Nanoscale via Environmental Proximity Engineering..... | 81 |
| 5.1 Introduction..... | 81 |
| 5.2 Synthesis and Intercalation of hBN/Ru(0001) Platform..... | 89 |
| 5.3 First Principles Calculation of the Intercalated hBN/Se/Ru | 91 |
| 5.4 Synthesis and Intercalation of MoSe ₂ /hBN/Ru Heterostructure | 94 |
| 5.5 Influence of Intercalation on the Electronic Structure of the MoSe ₂ /hBN/Ru Heterostructure..... | 96 |
| 5.6 Nanoscale P-N Junction..... | 98 |
| 5.6.1 Bandgap Renormalization..... | 99 |
| 5.6.2 Work Function Tuning | 101 |
| 5.6.3 Theoretical Model for the Nanoscale P-N Junction..... | 103 |
| 5.6.4 Summary of the Band Offsets and Work Function of MoSe ₂ P-N Junction..... | 106 |
| 5.7 Conclusion | 107 |
| Appendices..... | 109 |
| Appendix A: STM Methods..... | 109 |
| Appendix B: Determination of the BeO Atomic Fraction with XPS..... | 110 |
| Appendix C: STM Calibration..... | 113 |
| Appendix D: Methods of BeO/Ag(111) First Principles Theoretical Calculation | 114 |
| Appendix E: Methods of WS ₂ S Vacancy First Principles DFT Calculation | 115 |
| Appendix F: Methods of hBN/Ru(0001) and hBN/Se/Ru(0001) First Principles Theoretical Calculation..... | 116 |
| References..... | 117 |

List of Figures

| | |
|---|----|
| Figure 2.1: Topographic STM image of the Si(111) 7×7 reconstruction (adopted from Ref. [14])..... | 3 |
| Figure 2.2: Schematic of a metal-vacuum-metal tunneling junction | 5 |
| Figure 2.3 Schematic representing the Bardeen treatment of STM tunnelling | 7 |
| Figure 2.4 A basic map of the STM setup..... | 11 |
| Figure 2.5 A cartoon of the tunneling process with different applied sample bias. | 14 |
| Figure 3.1 Schematic of the bulk wurtzite and layered graphitic honeycomb phases of BeO | 17 |
| Figure 3.2 Schematic of the growth process of the honeycomb BeO | 20 |
| Figure 3.3 STM images of three BeO growths with different growth times..... | 21 |
| Figure 3.4 Plot of BeO coverage as a function of growth time..... | 22 |
| Figure 3.5 STM images of BeO islands with profiles showing the growth is a single monolayer | 23 |
| Figure 3.6 STM image of an Ag (111) film and full coverage monolayer h-BeO..... | 25 |
| Figure 3.7 XPS measurements of the Ag 3d and Be 1s core levels | 25 |
| Figure 3.8 Atomic resolution STM image of honeycomb BeO | 27 |
| Figure 3.9 LEED measurements on Ag(111) and h-BeO | 28 |
| Figure 3.10 STM image showing the BeO/Ag(111) moiré pattern..... | 29 |
| Figure 3.11 (a) Characterization of the BeO crystallinity using moiré pattern analysis..... | 31 |
| Figure 3.12 STS dI/dV characterization of the BeO electronic properties | 33 |
| Figure 3.13 Analysis of the work function modulation of the BeO across the moiré pattern using dZ/dV spectroscopy | 35 |
| Figure 3.14 First principles calculation of the h-BeO/Ag(111) interaction. | 37 |

| | | |
|-------------|--|----|
| Figure 4.1 | STM image of WS ₂ after thermal annealing showing different defects. Images taken from Ref. [109]. | 42 |
| Figure 4.2 | Optical images of CVD grown WS ₂ sample | 44 |
| Figure 4.3 | STM images of WS ₂ after thermal annealing. STS dI/dV spectroscopy of the WS ₂ band gap before and after annealing | 45 |
| Figure 4.4 | STM image of a the WS ₂ showing a variety of different sulfur vacancy defects, and correspodng schematics and DFT STM simulations | 47 |
| Figure 4.5 | STM and DFT analysis of S vacancy structure | 49 |
| Figure 4.6 | STS dI/dV measurements taken on different S vacancies | 51 |
| Figure 4.7 | Schematic explaining crystal field splitting of of the trigonal prismatic geometry of the TMD H phase. Images taken from Ref. [124], Ref. [125], and Ref. [126]. | 52 |
| Figure 4.8 | First principles calculation of TMD band structure, images were taken from Ref. [128] and Ref. [129] | 54 |
| Figure 4.9 | A schematic showing the origin of the S vacancy IGS. | 56 |
| Figure 4.10 | A schematic showing the origin of the IGS from S divacancies | 57 |
| Figure 4.11 | An STM image showing a variety of agglomerate S vacancies | 59 |
| Figure 4.12 | STM image of a point defect assumed to be a column vacancy, and dI/dV spectroscopy obtained on a line across the defect | 60 |
| Figure 4.13 | Comparison of DFT STM simulation and orbital density calculation of S top vacancy and column vacancy | 61 |
| Figure 4.14 | Comparison of DFT calculation of a column vacancy and STS dI/dV measurement on S column vacancy | 62 |
| Figure 4.15 | STM image and correspodng schematic of S lateral divacancy structure | 65 |
| Figure 4.16 | STM images of aggregate S vacancy defect | 66 |

| | | |
|-------------|--|----|
| Figure 4.17 | STM image of the aggregate S vacancy defect with corresponding dI/dV spectroscopy taken across the defect | 67 |
| Figure 4.18 | STM images of S vacancy line defects | 70 |
| Figure 4.19 | TEM image showing a WS ₂ line defect composed of S column vacancies taken from Ref. [106]..... | 71 |
| Figure 4.20 | STM image of a S vacancy line defect and corresponding dI/dV spectra obtained on the defect | 72 |
| Figure 4.21 | DFT calculation of DOS and band structure for two vacancies separated in the zig-zag atomic direction with increasing separation..... | 74 |
| Figure 4.22 | DFT calculation of DOS and band structure for two vacancies separated in the armchair atomic direction with increasing separation | 75 |
| Figure 4.23 | STM image of the lateral divacancy from Fig. 4.15 and a schematic and simulated STM images showing two S vacancies separated nearest and next nearest neighbors in the armchair direction | 76 |
| Figure 4.24 | Simulated STM images of lateral top and bottom S vacancies separated by one and two lattice constants. | 78 |
| Figure 4.25 | DOS calculation for a lateral top and bottom divacancy separated by one lattice constant | 79 |
| Figure 5.1 | Schematic showing the electric field of charges in a 2D TMD layer and a theoretical prediction showing a substrate with segments with different dielectric constants can modulate the bandgap of the overlying TMD layer to create a heterojunction. Images taken from Ref. [150]..... | 83 |
| Figure 5.2 | STM characterization of MoSe ₂ on a hBN/Ru substrate showing band gap renormalization. Images taken from Ref. [66]..... | 84 |

| | | |
|-------------|--|-----|
| Figure 5.3 | STM characterization of MoSe ₂ on hBN/Ru showing work function modulation of the MoSe ₂ across the hBN/Ru moiré pattern using dZ/dV spectroscopy. Images taken from Ref. [66] | 86 |
| Figure 5.4 | A schematic showing environmental proximity engineering of MoSe ₂ on hBN/Ru by Se intercalation to create a lateral p-n heterojunction. | 87 |
| Figure 5.5 | STM images of hBN on Ru before and after Se intercalation | 90 |
| Figure 5.6 | STM analysis comparing the surface topography of the hBN/Ru before and after intercalation | 91 |
| Figure 5.7 | DFT first principles calculation of the Se intercalated hBN/Ru platform | 93 |
| Figure 5.8 | STM analysis of MoSe ₂ on Se intercalated hBN and unintercalated hBN on Ru including topography and atomic structure | 95 |
| Figure 5.9 | dI/dV spectroscopy on MoSe ₂ /hBN/Ru, Se intercalated MoSe ₂ /hBN/Se/Ru, hBN/Ru and Se intercalated hBN/Se/Ru | 97 |
| Figure 5.10 | STM characterization of the change in electronic properties of the MoSe ₂ across boundary between the corrugated MoSe ₂ and Se intercalated flat MoSe ₂ by dI/dV spectroscopy | 98 |
| Figure 5.11 | Characterization of the band gap renormalization of the MoSe ₂ across the Se intercalation boundary by dI/dV spectroscopy | 100 |
| Figure 5.12 | dZ/dV spectroscopy on Se intercalated and unintercalated MoSe ₂ and hBN | 102 |
| Figure 5.13 | STM characterization of the work function tuning of the MoSe ₂ across the Se intercalation boundary by dZ/dV and dI/dV spectroscopy obtained along the same line..... | 103 |
| Figure 5.14 | Schematic of the 2D depletion region of a symmetric and asymmetric doped p-n junction. Images taken from Ref. [169] | 104 |

| | | |
|-------------|---|-----|
| Figure 5.15 | Plot of the MoSe ₂ CBM position at the Se intercalation boundary with a fitted model of the electrostatic potential..... | 106 |
| Figure B | Schematic of the BeO surface on top of the atomic layers of the Ag substrate for monolayer and bilayer BeO | 112 |
| Figure C | STM image showing atomic resolution of a Pb film | 114 |

Chapter 1

Introduction and Motivation

In his 1959 lecture “There's Plenty of Room at the Bottom: An Invitation to Enter a New Field of Physics,” Richard Feynman mused, “What could we do with layered structures with just the right layers? What would the properties of the materials be if we could really arrange the atoms the way we want them?” [1]. At the time of this prescient question, the realization of atomically thin materials seemed like a distant reality, possibly unattainable. Little did he know, merely forty-five years later, the discovery of graphene and its unprecedented properties would launch a new nanoscale era of condensed matter physics centered on 2D materials [2-4]. Early exploration of 2D materials focused on van der Waals (vdW) crystals, which have a naturally occurring bulk layered structure, leading to the existence of stable crystalline atomic layers. These single atomic layers have already shown immense potential for applications in nanoelectronics, with the creation of many conceptual 2D devices comprised of combinations of different 2D atomic layers [5-7]. However, device design is limited by the ability to tune the electronic properties of the 2D materials that form the basic elements of these devices. Now that we have landed at the “bottom,” having reached the geometric limit of atomically thin materials, there is plenty of room for exploration in this exciting 2D materials landscape.

In this work, we adopt a three pronged approach to expanding the library of electronic properties of 2D materials available for device design: discovery of new materials with attractive electronic properties, manipulation of the electronic structure of existing 2D materials by defect engineering, and utilizing the environmental sensitivity of 2D materials to tune their electronic properties via proximity engineering. Currently, the

main candidate filling the insulator role in 2D devices is hexagonal boron nitride (hBN), but in Chapter 3, we discuss the discovery of a new 2D insulator, honeycomb beryllium oxide (BeO) [8]. Although bulk BeO is not a layered vdW material, we demonstrate the epitaxial synthesis of a single atomic layer of honeycomb BeO, and characterize its structural and electronic properties for the first time. Within the class of existing layered vdW materials, much research has focused on the semiconducting transition metal dichalcogenides (TMDs), owing to their attractive properties such as a direct band gap at the monolayer limit [9, 10], interesting spin-valley physics [11], and high carrier mobilities [6], to name a few. In Chapter 4, we deliberately manipulate the electronic properties of TMD WS_2 by introducing a high concentration of S vacancies by thermal annealing. We show that defect-defect interactions cause a dramatic increase of states within the WS_2 , indicating that defect engineering provides a useful tool for manipulating the properties of existing 2D materials. Finally, in Chapter 5 we establish that environmental proximity engineering is an effective approach to designing a nanoscale lateral p-n junction in a single monolayer TMD. By applying Se intercalation at the interface of a hBN/Ru heterostructure, the hBN becomes decoupled from the Ru, altering its electronic properties. We directly show that the band profile of a MoSe_2 layer that transverses a Se intercalation boundary of the underlying hBN/Ru experiences dramatic band bending and band gap renormalization, creating a p-n junction in a single homogeneous 2D TMD monolayer. Thus, the three diverse directions of this work illustrate that the field of 2D materials is an immense playground for condensed matter research that is only limited by the imagination of the experimentalist.

Chapter 2

Scanning Tunneling Microscopy Background

2.1 HISTORY

The breakthrough invention of the first scanning tunneling microscope (STM) enabled the direct visualization of the atomic structure and nanoscale electronic properties of materials, ushering in a new era of nanoscale surface science. The inventors Binnig and Rohrer at IBM Zurich first demonstrated the power of this tool (along with Gerber and Weibel) by atomically resolving the now famous Si(111) – 7×7 surface reconstruction in real space for the first time (Fig. 2.1)[12-14]. The novelty of the STM was not lost on the greater science community, and Binnig and Rohrer were awarded the Nobel Prize just five years later in 1986. STM not only provides the ability to visualize atomic structure, but also to measure properties like superconductivity and magnetism, and manipulate individual atoms and molecules to create nanoscale structures. This capability has contributed to numerous innovations in basic science, and 40 years later, continues to be a fundamentally crucial instrument in the continued development of nanotechnology.

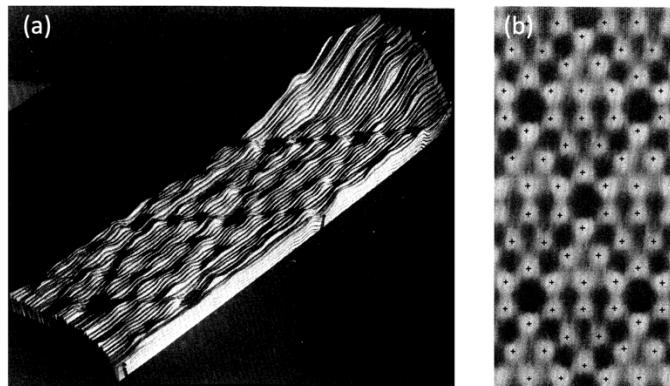


Figure 2.1: The first topographic image of the Si(111) 7×7 reconstruction taken by STM (adopted from Ref. [14])

2.2 TUNNELING THEORY

2.2.1 1D Barrier Model

The base operating principle of STM is the phenomenon of electron tunneling that arises from quantum mechanics. Tunneling is achieved by bringing an extremely sharp metallic tip close to a surface and applying a bias between them; the close proximity and applied bias enables the electrons to tunnel through the vacuum gap. To understand this tunneling concept, one can first consider the simple case of an electron tunneling through a one dimensional potential barrier [15]. If an electron with a mass m an energy E is incident on an energy barrier with a height U , the wavefunction ψ that describes the electron state must satisfy the Schrödinger equation:

$$-\frac{\hbar^2}{2m} \frac{d^2}{dz^2} \psi(x) + U(x)\psi(x) = E\psi(x). \quad (2.1)$$

In the classically forbidden region inside the tunneling barrier, this equation will have a solution of the form:

$$\psi(x) = \psi(0)e^{-\kappa z}, \quad (2.2)$$

where,

$$\kappa = \frac{\sqrt{2m(U - E)}}{\hbar}, \quad (2.3)$$

is the decay constant. If the barrier has a width $z = d$, then the probability density of the electron tunneling through the barrier is proportional to $|\psi(d)|^2 = |\psi(0)|^2 e^{-2\kappa d}$. Thus, this elementary picture illustrates that the transmission probability will decrease exponentially with barrier width, or in this case, the tunneling current will decrease exponentially with tip and sample distance. Taking this model one step further, we can examine the specific case of an electron tunneling from a metal, through vacuum, to an identical metal with a work function ϕ . Assuming a small applied bias of $V \ll \phi$ and neglecting thermal excitations, the decay constant can be approximated as $\kappa = \frac{\sqrt{2m\phi}}{\hbar}$ for an

electron near the Fermi level. For a typical work function around 4 eV, we find that the decay constant is $\kappa \sim 1 \text{ \AA}^{-1}$, which indicates that the tunneling probability will drop by a fraction of $e^{-2} = 1/7.4$ per angstrom, almost an order of magnitude. This example demonstrates why precise control of the tip-sample distance is a necessity for STM measurement.

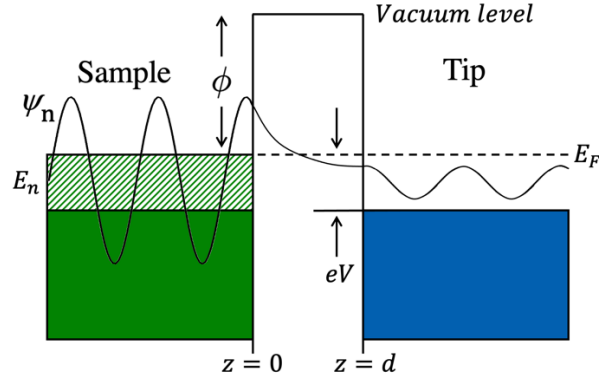


Figure 2.2: Schematic of a metal-vacuum-metal tunneling junction where ϕ is the work function. The sample is on the left, and the tip is on the right. The green striped area represents the states available for tunneling.

Continuing our investigation of metal-vacuum-metal tunneling, we expand our view from a single tunneling electron to the net tunneling current. When a bias voltage V is applied, only electrons in states ψ_n with energies E_n lying within the interval between $E_F - eV$ and E_F can tunnel and therefore contribute to the tunneling current (Fig. 2.2). Thus, the tunneling current (I_t) is proportional to the total number of states available within the energy window of eV :

$$I_t \propto \sum_{E_n=E_F-eV}^{E_F} |\psi_n(d)|^2. \quad (2.4)$$

If we assume that the density of electronic states can be approximated as constant for small $V = \epsilon$, then the sum of electronic states can be written in the form of the local density of states (LDOS) of the sample $\rho_S(x, E)$ at a location x and energy E_n near the Fermi level:

$$\rho_S(x, E) = \frac{1}{\epsilon} \sum_{E_n=E_F-eV}^{E_F} |\psi_n(x)|^2. \quad (2.5)$$

We can use this relation to conveniently express the tunneling current (Equation 2.4) at a location $x = d$ in terms of the LDOS $\rho(d, E_F)$ near the Fermi level as expressed in Equation 2.5:

$$I_t \propto \rho(d, E_F)V. \quad (2.6)$$

Although Equation 2.6 was derived using a simple 1D approximation, we are able to draw a remarkable conclusion: STM tunneling can be used to directly probe the local density of states of a sample.

2.2.2 Bardeen Tunneling Model

The basic 1D barrier treatment of STM tunneling demonstrates some important basic concepts, but it is missing principles that are essential for interpreting STM measurements. In reality, not only is the tip sample system three dimensional, but both the tip and the sample density of states cannot be approximated as constant. Therefore, a more precise formalism must be adopted to determine the details of the physical properties contributing to the tunneling current. To address this issue, Bardeen developed an approach that treats the electronic states of the tip and sample separately, and then applies time dependent perturbation theory to calculate the tunneling rate [16]. First, the electronic states of the tip (φ) and sample (χ) are calculated separately by solving the stationary Schrödinger equation. These wave functions decay into the vacuum gap and have some amount of overlap (Fig 2.3); Bardeen utilized time dependent perturbation theory to show that the electron transfer depends on the amount of this overlap, expressed by the tunneling matrix element $M_{\varphi\chi}$:

$$M_{\varphi\chi} = \frac{\hbar}{2m} \int_{z=z_0} (\varphi^* \frac{\partial \chi}{\partial z} - \chi \frac{\partial \varphi^*}{\partial z}) dS, \quad (2.7)$$

where z is a location within the vacuum region. Applying Fermi's Golden Rule [17], the probability w of tunneling from tip state φ with energy E_φ to sample state χ with energy E_χ is shown to obey the following equation:

$$w = \frac{\hbar}{2m} |M_{\varphi\chi}|^2 \delta(E_\varphi - E_\chi), \quad (2.8)$$

where the delta function indicates that only tunneling between states with the same energy is allowed, therefore only elastic processes are considered.

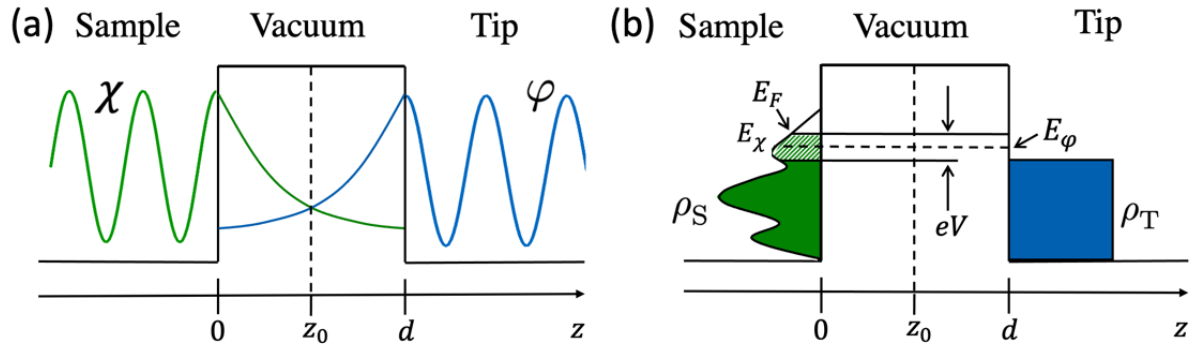


Figure 2.3 (a) Schematic representing the Bardeen approach where the sample (χ) and tip (φ) wave functions (left) are treated separately and decay into the vacuum. The tunneling probability is proportional to the amount of overlap of the wave functions. (b) By using perturbation theory and applying Fermi's golden rule the tunneling current is determined from the convolution of the density of states in the tip and sample.

Following a similar approach to the previous 1D metal-vacuum-metal tunneling example, the tunneling current I_t can be calculated by summing over all the states from the Fermi level to the applied bias voltage eV :

$$I_t = \frac{4\pi e}{\hbar} \int_{-\infty}^{\infty} f(E_F - eV + \epsilon) - f(E_F + \epsilon) \times \rho_S(E_F - eV + \epsilon) \rho_T(E_F + \epsilon) |M_{\varphi\chi}|^2 d\epsilon, \quad (2.9)$$

where $f(E) = \left[1 + \exp\left(\frac{E - E_F}{k_B T}\right)\right]^{-1}$ is the Fermi distribution function at a finite temperature T , and ρ_S and ρ_T are the density of states of the tip and sample, respectively. Assuming

that $k_B T$ is much smaller than the energy resolution of the measurement, the Fermi distribution can be approximated as a step function, simplifying the expression:

$$I_t = \frac{4\pi e}{\hbar} \int_0^{eV} \rho_S(E_F - eV + \epsilon) \rho_T(E_F + \epsilon) |M_{\varphi\chi}|^2 d\epsilon. \quad (2.10)$$

If we further assume that the tunneling matrix element $M_{\varphi\chi}$ does not change much within the energy interval of interest, then Equation 2.10 can be simplified even further:

$$I_t \propto \int_0^{eV} \rho_S(E_F - eV + \epsilon) \rho_T(E_F + \epsilon) d\epsilon. \quad (2.11)$$

From this formula, one can draw an important conclusion: the tunneling current is a convolution of both the density of states of the tip and the sample. In most cases, the goal of STS experiments is to probe only the density of states of the sample, and Equation 2.11 exposes the importance of the choice of tip to tease apart the electronic properties of the sample. One can cleverly choose a metallic tip with a density of states that is fairly constant to distinguish the contribution of the sample density of states to the tunneling current. In this case, taking the derivative of Equation 2.11 one finds:

$$\frac{dI}{dV} \propto \rho_S(E_F - eV). \quad (2.12)$$

This result establishes that the tunneling conductance is proportional to the density of states of the sample, an implication of extreme relevance for STM study. This suggests that by measuring the changes in tunneling current while varying the applied bias voltage, the local density of states of the sample can be mapped out directly. This is the theoretical foundation of scanning tunneling spectroscopy (STS) which will be discussed further in Section 2.3.2.

2.2.3 Tersoff-Hamann Approximation

Bardeen's description of electron tunneling made an important assumption that the tunneling matrix element $M_{\varphi\chi}$ does not change appreciably within the tunneling energy interval. This implies that the tunneling probability does not depend on the states involved;

put more directly, the likelihood of a tunneling event from a specific state in the sample to a state with corresponding energy in the tip is equal for all states. Equation 2.7 indicates that the tunneling matrix element $M_{\varphi\chi}$ depends on the degree of overlap of the tip and sample states participating in the tunneling event, but the decay of the electron wave function into the vacuum gap might be depend on the particular sample electron state. Put this way, it becomes clear that the presumption of constant $M_{\varphi\chi}$ doesn't seem like a factor that can be taken for granted, and requires further investigation.

The theory of Bardeen was further refined by Tersoff and Hamann, who included a realistic representation of the tip and sample surface wave functions by including the geometry of the tip-sample system [18, 19]. Rather than assuming the tunneling matrix elements $M_{\varphi\chi}$ can be considered a constant, they seek to evaluate them with these approximated wave functions. The crystalline sample surface has a two dimensional periodicity, therefore the sample wave function $\psi_{\vec{k}_{\parallel}}(\vec{r})$ can be written in the form of a two dimensional Bloch wave:

$$\psi_{\vec{k}_{\parallel}}(\vec{r}) = e^{-i\vec{k}_{\parallel}\vec{r}_{\parallel}} \sum_{\vec{G}_{\parallel}} c_{\vec{G}_{\parallel}} e^{-z\sqrt{\kappa^2 + \tilde{\kappa}^2}} e^{i\vec{G}_{\parallel}\vec{r}_{\parallel}}. \quad (2.13)$$

Here, the vector \vec{G}_{\parallel} is the surface reciprocal lattice vector, $c_{\vec{G}_{\parallel}}$ are the coefficients of the Fourier components, and \vec{r}_{\parallel} is the component of the vector \vec{r} parallel to the sample surface. In this formulation, z is the direction perpendicular to the sample surface, therefore the wave function is made up of plane waves that travel parallel to the sample surface, and decay exponentially into the vacuum. The tunneling decay is governed by $\sqrt{\kappa^2 + \tilde{\kappa}^2}$, where κ is the same as the 1D barrier case (Eq. 2.3) and $\tilde{\kappa} = \vec{k}_{\parallel} + \vec{G}_{\parallel}$. We see that unlike the previous 1D model (Eq. 2.2), the electron decay into the vacuum depends on the parallel momentum of the electron. One can immediately deduce that the wave functions at the Γ point of the corresponding two dimensional Brillouin zone ($\vec{k}_{\parallel} = 0$) will decay the least,

while critical points at the edge of the Brillouin zone such as the K point will decay much faster. This has important implications for materials such as the TMDs, where the CBM or VBM are at the K point, because states at the nearby Γ point will dominate the tunneling process and drown out tunneling from the K point. This phenomenon was carefully investigated by Zhang et. al., showing the tip must be very close to the surface in order to detect tunneling from the K point, therefore special care must be taken when interpreting scanning tunneling spectroscopy and assigning the band edge locations [20].

2.3 STM OPERATION

Scanning tunneling microscope operation is centered on the ability to bring a metallic tip within angstroms of a sample surface, enabling tunneling as discussed in the previous section 2.2.1. It is easy enough to imagine the possibility of such a tunneling process, but the exercise of actually implementing and controlling the tunneling is dependent on some key components. First, in order to measure a sample surface, it should ideally be atomically clean with few adsorbates; thus, most STM systems are housed in an ultra-high vacuum (UHV) environment. The essential elements of the STM instrument design include the tip, piezo scanner, coarse approach, controlling electronics, and vibration isolation. These elements work together to bring the tip atomically close to the sample surface, maintaining the vacuum gap without crashing into the surface. Here, a brief overview of the operation of the STM is provided.

An atomically sharp metallic tip is necessary to obtain atomic resolution images with STM (see Appendix A for tip preparation details). Further, the tip sample distance and the lateral motion must be maintained with fine control and subatomic precision. This is achieved by mounting the tip on a piezoelectric (PZT) scanner, which uses the piezo electric effect to finely control the tip position with picometer scale precision in the x, y,

and z directions by applying voltages to the outer electrodes. The piezo scanner is mounted on a faster coarse approach called a walker to safely move the tip close enough to the sample surface for the piezo scanner to engage the fine approach.

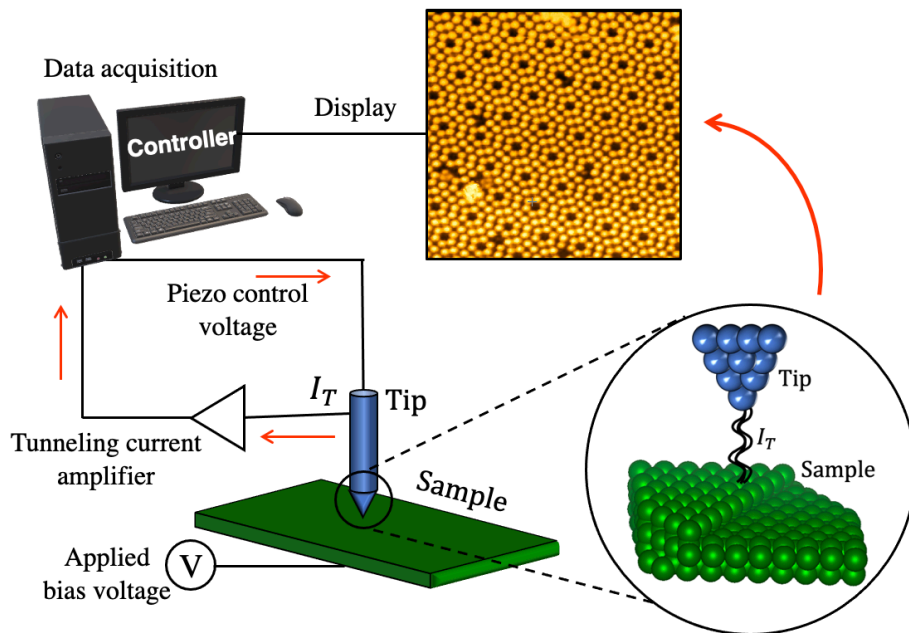


Figure 2.4 A basic map of the STM setup shows a bias is applied to the sample, the tip scans and the tunneling current is amplified and sent to the computer and recorded. The controller sends a bias to the piezo scanner adjusting the tip position. Data is recorded and displayed in an image of the sample surface.

Once the tip is in tunneling range, the tunneling current amplitude is in the range of picoamperes to nanoamperes, thus, a current preamplifier with a gain of $\sim 10^9$ V/nAmp converts this low current to a voltage. This signal is sent to a controller that regulates the x-y tip movement, maintains a constant current with a feedback loop that constantly adjusts the tip-sample distance, and acquires data (see Figure 2.4). However, this angstrom scale tip sample distance cannot be protected by the piezo scanner feedback loop alone, as floor vibrations can introduce strong instability to the tip-sample gap. Thus, vibration isolation of the STM system is the final vital element of STM operation.

2.3.1 Constant Current Imaging - Topography

The most common mode of STM operation is the constant current imaging mode. In this mode, the current is maintained at a constant value or “setpoint” by the z-feedback loop while the tip is scanned across x-y plane of the sample surface. During the measurement, the value of the tip height z is recorded at each x-y position. Since the tunneling current is extremely sensitive to the tip-sample distance, changes in the sample height will result in adjustments to the tip height z to maintain the current setpoint. Thus, an atomic scale topographic image can be obtained by plotting the recorded z values with a color scale that reflects the height variation at each x-y position. However, there is one caveat when interpreting these topographic images. As was demonstrated by Equation 2.6, the magnitude of the tunneling current reflects the local density of states of the sample, which may vary in real space. Thus, the STM does not merely “take pictures” of the surface topography, but rather shows a convolution of the surface structure and the local density of states in real space. This is especially important to keep in mind when interpreting constant current images where there may be localized changes in the electronic properties of a material, as we will see later.

2.3.2 I-V Tunneling Spectroscopy

Direct observation of nanoscale atomic structure is an impressive capability, but the true power of STM lies in the ability to obtain the local density of states of a sample surface with nanoscale resolution. As outlined above in section 2.2.2, Equation 2.12 shows that the LDOS of a sample is proportional to change in tunneling current as a function of applied bias voltage (dI/dV) when a metallic tip is used. This property can be utilized to obtain the LDOS by placing the tip above a point of interest on the surface and performing I-V spectroscopy. In order to probe only the LDOS, the tip height must be held constant,

therefore the feedback loop is paused during this procedure. Then a voltage sweep is performed, where the applied bias is changed by small increments while the tunneling current is recorded at each voltage. By taking a numerical derivative of the recorded I-V curve, the change in the tunneling current as a function of voltage is acquired. Plotting the resulting dI/dV curve, the LDOS of the sample can be directly visualized.

Taking a closer look at the details of the I-V tunneling process, Figure 2.5 shows a schematic of the tunneling between the sample and tip. Note that the DOS of the metallic tip is flat (constant) across all voltages, while the sample DOS varies at different energies. When a positive bias is applied to the sample, electrons will flow from the tip, to the available empty states in the sample. The changes in the tunneling current here will reflect the changes in the LDOS of the sample, therefore the unfilled “empty” states of the sample can be mapped. When a negative bias is applied, electrons will tunnel from the sample to the empty states in the tip, resulting in a sample “filled” state LDOS map. It is important to note that this description describes a configuration of bias applied to the sample (the configuration of the STM used in this study); the opposite tunneling scenario will be true when the bias is applied to the tip.

A significant feature of I-V spectroscopy is that the LDOS of the sample directly beneath the tip is probed. If an atomically sharp tip is prepared, then the LDOS can be mapped in real space at the atomic scale by performing spectra at different locations across a feature of interest. Harnessing this STM capability has made many scientific innovations attainable: the measurement of molecular vibrational modes, demonstration of high T_c superconducting gap, visualization of electron standing waves, and plotting semiconductor band offsets, to name just a few [21-24]. Indeed, this powerful technique opened up unlimited possibilities for nanoscale scientific exploration.

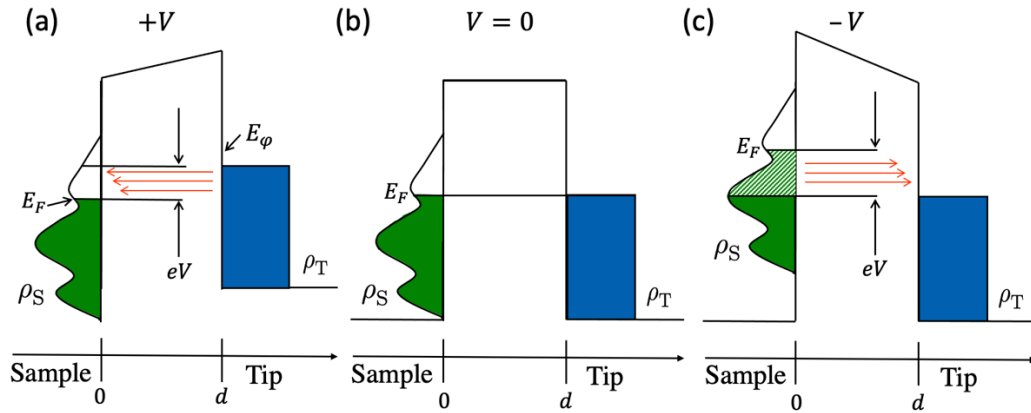


Figure 2.5 A cartoon of the tunneling process with different applied sample bias. (a) At positive bias voltage, the sample Fermi level is lower than the tip, and tunneling from the tip to sample “unfilled” states occurs. (b) No bias, the Fermi level of the tip and sample are aligned. (c) At negative applied sample bias, electrons from the sample filled states tunnel to the unfilled tip states.

2.3.3 Z-V Field Emission Resonance Spectroscopy

Another less commonly used spectroscopy technique is Z-V spectroscopy. In this spectroscopic technique, the tunneling current is held constant while the tip-sample distance (Z) versus bias sweep is recorded. When the applied bias exceeds the tunneling barrier, the electron tunneling enters the kinetic field emission regime, where the electron wave functions form plane waves. Some of the incident electrons will be reflected, and at specific bias voltages, interference between these incident and reflected electrons will form standing waves in the tip-sample gap [25-27]. At the onset of each standing wave, called a field emission resonance (FER), there is a steep increase in the tunneling current. Since the feedback is left on during the measurement, the tip height z will then increase to maintain constant current. Therefore, plotting the derivative $(\partial Z/\partial V)_I$ denotes the locations of the FER.

As discussed in section 2.2.1, the tunneling barrier height depends on the work functions of both the tip and the sample. Therefore, the onset of the first FER can be used as a good approximation of the work function of the sample [25, 26]. Calculating the precise measure of the sample work function is difficult as the tunneling barrier height also depends on the work function of the tip. However, the relative differences in the onset of the FER measured with the same tip will give accurate values for the relative change in work function between different locations of interest on the sample surface. We exploited this this property in our studies to show how structural changes in our sample systems affect the work function.

2.4 SUMMARY

In conclusion, the scanning tunneling microscope is a truly unique tool that enables the direct visual observation of both the nanoscale atomic structure and electronic structure of surfaces. For atomically thin 2D materials, the low dimensionality leads to extreme surface to volume ratio, that is, the surface is the bulk of the material. Thus, as STM is a surface characterization technique, it provides an exceptional tool for the direct observation of 2D materials at the nanoscale. As we will see in the next chapters, the experimental studies reported here hinge on the capability of measuring the electronic properties of 2D materials at the nanometer scale, therefore the STM is the main character and most valuable player of all the characterization techniques utilized in this work.

Chapter 3

Epitaxial Growth of Novel Two-Dimensional Insulator Monolayer Honeycomb BeO

3.1 INTRODUCTION AND MOTIVATION

One property 2D materials share is strong in-plane bonding with weak interlayer interactions, leading to the existence of stable isolated crystalline atomic layers. This enables the design of ultrathin 2D devices with different crystalline atomic layers as the building blocks. While many conceptual devices are fabricated by mechanical exfoliation, in order to create a scalable technology platform, it is critical to develop an epitaxial growth method for single crystalline 2D materials. Early exploration of 2D materials focused on van der Waals (vdW) crystals, which have a naturally occurring bulk layered structure, and have already demonstrated significant potential for 2D technological applications. Synthesis of epitaxial wafer scale monolayers has been achieved for graphene and hBN [28, 29], proving that large scale growth is feasible for vdW materials. While the success of vdW crystals is promising, the family of layered bulk solids is limited, constraining the variety of structural and electronic properties available for device design.

Driven by the desire to expand the library of 2D materials, there has been increased exploration into the synthesis of stable atomically thin phases of electronic materials without a bulk layered structure. For example, 2D allotropes of elements such as silicene [30, 31], germanene [32], stanene [33, 34], and borophene [35, 36], among others, have been successfully grown and are predicted to have attractive electronic properties. However, unlike graphene, these elements do not favor sp^2 hybridization and adopt a mixed sp^2 - sp^3 hybridization, resulting in a buckled honeycomb structure. This lack of a stable planar phase creates challenges such as multi-phase growth, buckled superstructures, and

strong substrate interactions [30-34]. By contrast, polar wurtzite structure materials were surprisingly predicted to circumvent the bulk thermodynamic constraint at the few layer limit, resulting in a stable planar sp^2 hybridized graphitic phase [37]. In the thin regime of a few atomic layers, polar ionic bonds may turn into the in-plane direction, forming a honeycomb structure to diminish unstable surface polarization (shown schematically in Figure 3.1) [37, 38]. This theory indicates that initial growth forms a graphitic film, and at a critical layer number, the crystal becomes unstable and converts to a wurtzite structure [37]. These predictions have stimulated intensive experimental investigations of the graphitic phases of bulk wurtzite structure materials [39, 40], with ZnO grown on (Ag, Au) substrates drawing the most attention [41-43]. Motivated by the success of these experimental studies, the question naturally arises as to whether other wurtzite structure materials can be epitaxially grown as a 2D graphitic layer.

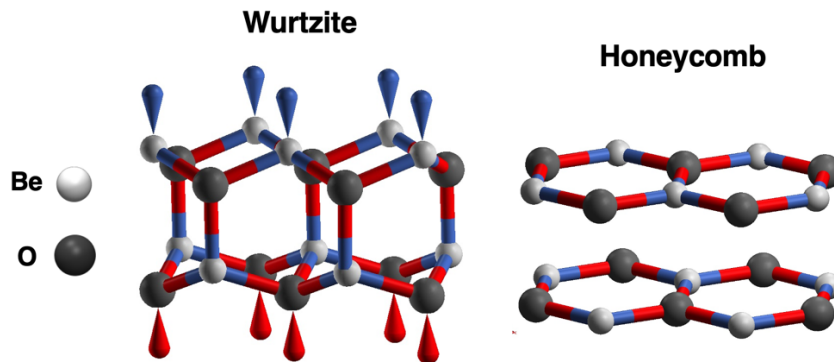


Figure 3.1 Schematic of the bulk wurtzite (left) and layered graphitic honeycomb (right) phases of BeO. The Be and O atoms are white and grey, respectively.

3.2 BERYLLIUM OXIDE BACKGROUND

Beryllium oxide (BeO) is a polar wurtzite structure material with attractive physical and mechanical properties, such as a high thermal conductivity and hardness, and a large insulating bandgap of 10.7 eV. These attractive properties have inspired significant

theoretical research interest concerning the existence of other possible structural phases of BeO. In particular, as a member of the isoelectronic series of first row elements like graphene and hBN, studies predicted BeO might also exist in a sp^2 hybridized atomic layer with a honeycomb structure (h-BeO) [44, 45]. Later, monolayer graphitic h-BeO was predicted to be energetically stable in free space, and that it could be synthesized from BeO molecules [46]. Further, not only was h-BeO predicted to have the most stable graphitic phase of wurtzite materials [37], but theoretical surveys of possible monolayer honeycomb structures of II-VI semiconductors predicted h-BeO has the lowest formation energy corresponding to the bulk phase [47], and was deemed the most experimentally achievable [38]. Though h-BeO is predicted to exist at the ultra-thin limit, synthesis of this intriguing material has remained elusive. There have been efforts to synthesize atomically thin BeO on a supporting substrate [48, 49], but thus far no convincing evidence of honeycomb structure BeO has been provided until recently. The only experimental evidence of planar h-BeO to date was achieved by a wet chemistry approach in a graphene liquid cell, but the growth was ~ 20 layers thick and polycrystalline on the order of tens of nanometers [50]. Nevertheless, these promising theoretical and experimental results strongly suggest that the epitaxial growth of crystalline, monolayer h-BeO is experimentally achievable.

In this work, we report the realization of the epitaxial growth of a single atomic sheet of h-BeO grown on an Ag(111) thin film which is also grown epitaxially on a Si (111) substrate using molecular beam epitaxy (MBE). Here, we employ scanning tunneling microscopy (STM) to directly characterize the atomic and electronic structure of the BeO, and further show that the monolayers maintain high crystallinity across the Ag terraces. Using low energy electron diffraction (LEED), we reveal that the h-BeO nanosheet covers a macroscopic length scale wafer ($5 \times 5 \text{ mm}^2$) and maintains uniform crystallinity at this

length scale. Finally, using STS and complimentary density functional theory (DFT) calculations, we show that the h-BeO weakly interacts with the Ag surface.

3.3 MBE SYNTHESIS OF HONEYCOMB BeO

Our experiments were performed in a UHV system that combines a homebuilt STM with two homebuilt MBE systems, one for growth of the Ag thin films, and one for BeO growth and LEED measurements. All of the chambers have base pressures below 1×10^{-10} Torr. The honeycomb structure BeO was epitaxially grown on Ag(111) substrates using the growth process shown schematically in Figure 3.2. The growth of the Ag(111) thin film substrate begins first with preparing Si(111) wafers with 0.5 mm thickness by cutting them into $10 \times 4 \text{ mm}^2$ pieces, compatible with the STM sample holders. The sample is prepared following the standard procedure of flashing (1400 °C) and annealing (950 °C) in UHV to prepare an atomically clean surface with a well-defined 7×7 reconstruction. Next, growth of the Ag(111) thin films was carried out at room temperature with a deposition rate of 3 nm/min. The average thickness of the Ag films used in this study is 150 nm. The as-grown Ag film already has a well-defined (111) orientation; however, the surface is relatively rough. Annealing the film at 500 °C for one hour yields a much smoother surface with well-defined triangular terraces whose step edges are parallel to the $\langle 110 \rangle$ directions (see Ref. [51] for details). Next, a monolayer sheet of BeO was grown epitaxially on the epitaxial Ag(111) thin films. A Knudsen-cell with a BeO crucible purchased from Fermi Instruments (> 99% purity) was used as the evaporation source with a source temperature of 1200 °C. The Ag(111) substrate was maintained at 500 °C during the growth. Under these conditions, the initial growth rate is roughly ~ 0.1 ML per minute, discussed further below. After the desired coverage was reached, the shutter to the BeO source was closed, and the BeO sample was annealed at the growth

temperature for 15 minutes. The chamber pressure during the growth reached 8×10^{-10} Torr.

This simple two-step epitaxial growth method, (see Fig 3.2) makes the h-BeO growth conveniently scalable. Figure 3.2 shows the typical sample wafer size; however, we note that the sample size is constrained by the STM stage, and larger film growth is likely possible. The use of Si wafer substrates, as well as a the completely *in situ* growth process makes BeO an attractive candidate for use as a substrate for future device applications. In addition, as we show below, the BeO growth rate decreases as the coverage increases, suggesting that the growth might be self-limited to a monolayer, similar to that of hBN on transition metal surfaces.

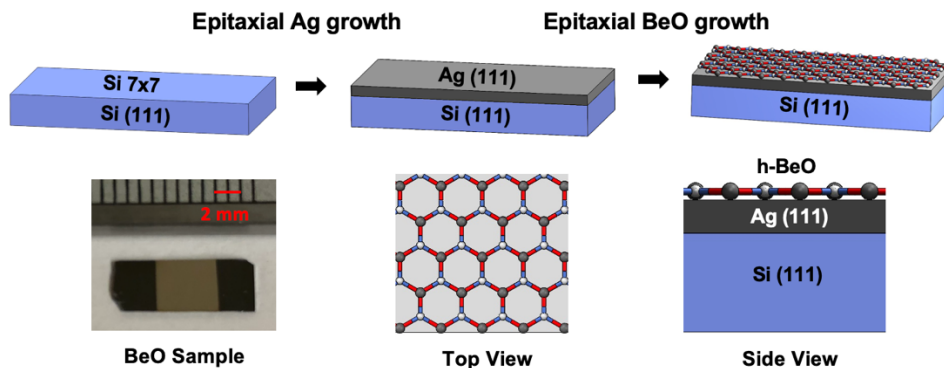


Figure 3.2 Schematic of the growth process of the honeycomb BeO. From left to right, a Si(111) substrate is prepared with a 7x7 reconstruction, a 150 nm Ag film is epitaxially grown, and honeycomb BeO is grown epitaxially on top. Below is an image of the BeO sample and a schematic of the top and side view of the heterostructure.

3.3.1 Determination of the BeO Growth Rate

In order to understand the behavior of the BeO growth, we first investigated the growth rate. To determine the BeO coverage as a function of growth time, we analyzed STM images of BeO samples with different growth times (see Appendix A for STM

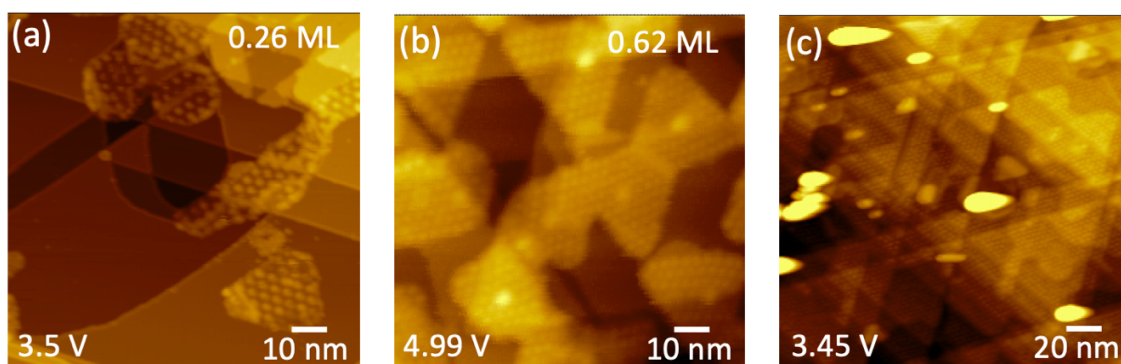


Figure 3.3 STM images of (a) 2 minute, (b) 7 minute, and (c) 30 minute BeO growth. After a long deposition (c) the excess BeO forms clusters on the surface.

methods). Figure 3.3 above shows (a) a 2 minute, (b) a 7 minute, and (c) a 30 minute BeO growth. We analyzed images from both the 2, 6, 7, and 12 minute growths to determine the BeO coverage of the Ag substrate as a function of time (Figure 3.4). This analysis gave a growth rate of 0.13 ML/min for the 2 minute growth, which suggests that if the growth was linear, there should be a complete monolayer growth of the BeO after <10 minutes. We find that at longer growth times past the full coverage regime, additional deposition doesn't result in additional growth past the monolayer. Figure 3.3 (c) shows a 30 minute growth of BeO, and with this much longer deposition time, and we see BeO clusters forming. Note that if the epitaxial growth continues linearly after the first monolayer, a 30 minute deposition would lead to a 4 ML thick layer. It would be difficult to tunnel through such a thick insulating film, and the tip should crash, but we obtained a clear image. Next, a determination of the volume of the clusters for the 30 minute growth was made based on the measured topography. Even though this analysis gives an over-estimation due to the tip shape convolution, in an area of 200 nm x 200 nm, the clusters have a volume of 2000 nm³, corresponding a 0.05 nm coverage (or 0.16 ML). Thus, even if we assume all the clusters are due to BeO, the growth rate would be 20 times lower than the initial growth

rate of the 1st layer. With this empirical evidence, we suggest that the growth rate is nonlinear, and seems to saturate after one monolayer, with additional BeO creating clusters on the surface of a well annealed sample.

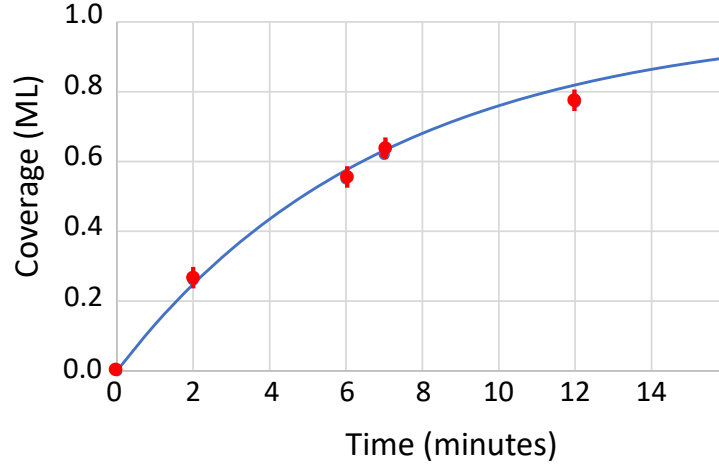


Figure 3.4 BeO coverage as a function of growth time for five different BeO growths showing the growth rate is nonlinear and decreases at higher coverage.

Above (Figure 3.4) we show the results for the h-BeO areal coverage versus growth time (while keeping the source temperature and substrate temperature unchanged) which shows non-linear time dependence. The blue curve is a fit for the coverage as a function of deposition time following the equation $x(t) = 1 - e^{-At}$ where A is $1/7 \text{ minutes}^{-1}$. This is a solution for the differential equation,

$$\frac{dx}{dt} = A(1 - x).$$

Here, $\frac{dx}{dt}$ is the growth rate where $(1-x)$ is the Ag(111) surface area not yet covered by the h-BeO (or equivalently the exposed Ag area). Thus, the experimental data suggests that the growth is governed by the interaction with the exposed Ag, and therefore, the substrate choice of Ag(111) may play a critical role in stabilizing the BeO growth.

3.4 MONOLAYER HONEYCOMB BeO CRYSTAL STRUCTURE

3.4.1 BeO Monolayer

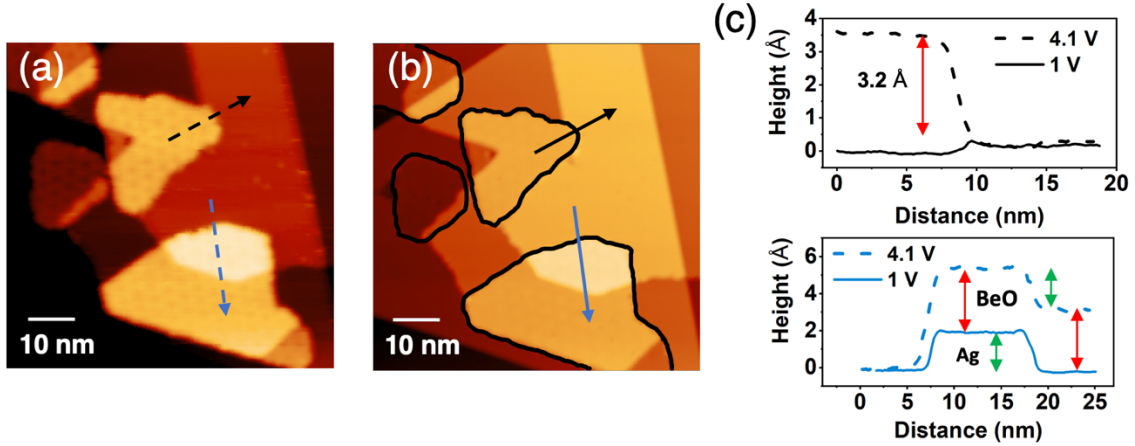


Figure 3.5 STM images of a 0.4 ML growth of h-BeO acquired at $I_t = 5$ pAmp and (a) 4.1 V and (b) 1 V sample bias (area: 70×70 nm²). The black and blue arrows correspond to the line profiles in (c) showing that the appearance of multilayer BeO growth is from BeO monolayers crossing underlying Ag terraces. The h-BeO monolayers islands have a height of ~ 3.2 Å.

The underlying Ag substrate has many triangular terraces (shown later) therefore it was initially unclear whether multilayer BeO growth was present. To further investigate this, we studied a sample with submonolayer coverage of 0.4 monolayer, presented in STM images at different bias conditions, $V_s = 4.1$ V and 1 V, respectively (Figure 3.5 (a,b)). As discussed below, the h-BeO has a relatively large bandgap with the conduction band minimum (CBM) located at $\sim 3.0 \pm 0.2$ eV above E_F . Consequently, Figure 3.5 (a) (with sample bias above the CBM) shows the formation of well-defined h-BeO islands that can be identified by a distinct moiré pattern, while in Figure 3.5 (b) (bias below the CBM) the h-BeO regions, outlined in black for clarity, are almost indistinguishable from the Ag surface. When the sample bias is within the h-BeO bandgap, quantum tunneling occurs only from the Ag states through the BeO layer, resulting in an image that reflects the step

structure of the underlying Ag (Figure 3.5 (b)). Although the surface exhibits a multi-step morphology, a careful comparison of the bias dependent images allows us to conclude these are single layer h-BeO 2D islands on Ag(111). Figure 3.5 (c) shows line profiles corresponding to the black and blue lines in Figures 3.5 (a) and (b), with the arrow denoting the direction of the line cut. The thickness of the h-BeO is determined by comparing the black line cuts across the h-BeO island shown in the top graph of Figure 3.5 (c). At 1 V (solid line), the profile is nearly flat except for a small depression of 0.3 Å at the BeO layer. It has been shown that the apparent height of insulator islands has a strong bias dependence, and depressions have also been seen at low bias for insulators such as MgO and CoO [52, 53]. At 4.1 V, the BeO step height appears ~ 3.2 Å above the Ag substrate (see Figure 3.5 (c)), which is consistent with the predicted interlayer spacing of the hypothetical graphitic BeO structure [44], as well as our theoretical calculation (discussed below). The blue line cuts in Figures 3.5 (a,b) cross a feature that resembles a second layer of h-BeO at first sight, but the corresponding line profiles (bottom graph of Figure 3.5 (c)) validate the existence of a single h-BeO layer. We determine a step height of ~ 2.2 Å (green arrow) which correlates to the underlying Ag terrace height, while the difference in height of the two curves (red arrows) clarifies that h-BeO covers the Ag surface in a uniform monolayer, rolling over the Ag steps.

We further characterized a complete monolayer growth of h-BeO by STM, as shown in Figure 3.6 (a-c). A 120 nm x 120 nm STM image (Figure 3.6 (a)) of the Ag(111) thin film substrate shows triangular atomic terraces bordered by atomic steps (step height of 2.36 ± 0.1 Å). Figure 3.6 (b,c) are STM images of a surface after a complete atomic sheet of honeycomb BeO was deposited, acquired at a sample bias of 2.5 V and 3.55 V, respectively. As discussed above, STM images obtained below the h-BeO CBM reflect the morphology of the underlying Ag surface, which explains the similarity of Figure 3.6 (b)

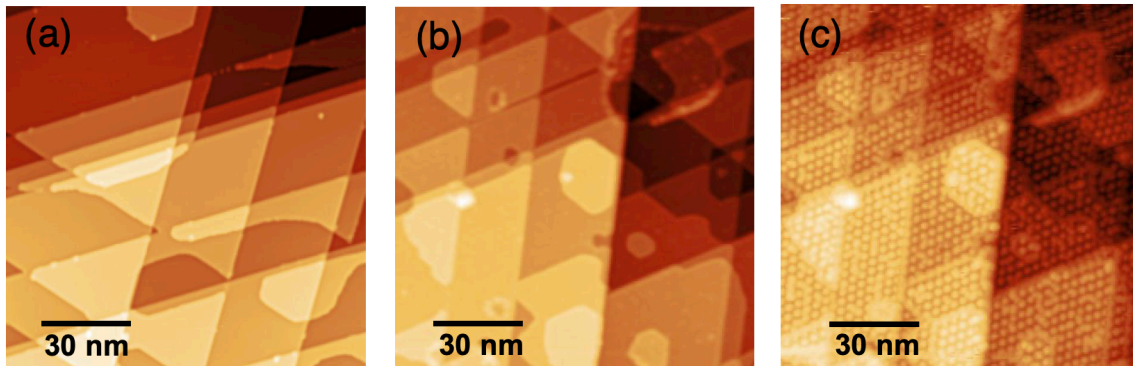


Figure 3.6 (a) STM image of an Ag (111) film, and (b,c) full coverage monolayer h-BeO surface, (area: $120 \times 120 \text{ nm}^2$) $I_t = 5 \text{ pAmp}$, $V_s = 2 \text{ V}$, 2.5 V , and 3.55 V respectively. At low bias (b) the BeO sample looks like the bare Ag substrate (a), while at high bias (c) the BeO moiré pattern becomes visible.

to the pristine Ag(111) in Figure 3.6 (a). The measured step heights in images 2.6 (b) and (c) are $2.36 \pm 0.1 \text{ \AA}$, which matches the Ag terrace height, confirming the sample surface is covered with a complete monolayer of h-BeO that rests on the Ag(111) surface like a carpet, rolling over the terraces. At a sample bias of 3.55 V (above the CBM), one observes a clear moiré pattern due to the beating between the atomic lattices of the h-BeO and Ag(111) surface (Figure 3.6 (c)). We note that the contrast of the moiré pattern is curiously reversed from the pattern shown in Figure 3.5 (a), which will be analyzed in detail later.

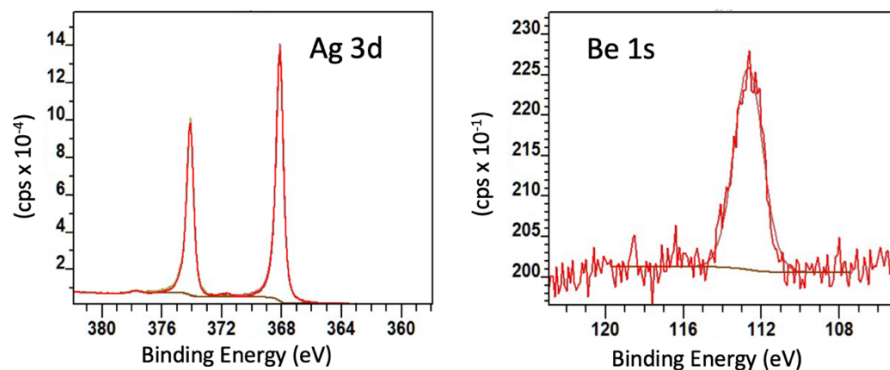


Figure 3.7 XPS measurements of the Ag 3d and Be 1s core levels, respectively. The Be/Ag atomic fraction ratio is determined to be 1:4.23 within the probed depth.

As additional verification that the sample surface is indeed covered in a monolayer of BeO, we carried out *ex-situ* XPS (x-ray photoelectron spectroscopy) measurements of the Ag and Be core levels (Figure 3.7). First, the signals were normalized to the photoionization cross-section of the respective elements, then the XPS signal gives the atomic fraction of each element within the probed volume. We took into account that the difference in lattice constant of the BeO and Ag result in a Be density that is greater than the Ag. In addition, the Ag signal is the sum of many layers, and the attenuation of the Ag signal traveling to the surface also needs to be taken into account. With this knowledge, we calculated the anticipated ratio of the Ag and Be signals for a monolayer of BeO, and compared the results with measured XPS signals. We found that the ratio of the Ag and Be signals to be ~ 4.8 , which is reasonably close to the experimentally measured value of 4.23. We therefore conclude the XPS measurement is consistent with a single monolayer of honeycomb BeO. Details of this analysis can be found in Appendix B.

3.4.2 Honeycomb BeO Atomic Structure

The atomic structure of the BeO layers is determined using three approaches: atomic resolution STM imaging, low energy electron diffraction (LEED), and moiré pattern analysis. High-resolution STM images acquired at $V_s = 0.05$ V (Figure 3.8 (a)) verify that the BeO has a honeycomb atomic structure by direct observation. Below the atomic resolution image, a line profile shows the atomic corrugation of the h-BeO, which yields a lattice constant of 2.61 ± 0.08 Å (see Appendix C for details of the STM calibration). An enlarged view of the honeycomb structure is visible in Figure 3.8 (b), which shows the atomic lattice with the location of the atomic sites of the Be (cross) and O (circle) atoms marked within the unit cell, with a corresponding model shown in Figure 3.8 (c). The line profile along the diagonal direction of the unit cell reveals the location of

the atoms, with the O atom at the primary maximum and the Be atom at the shoulder. It is interesting that atomic resolution of the BeO is observed when the sample bias is set within the BeO band gap, but this phenomenon is common for atomically thin insulators on metal surfaces [42, 54], and the contrast mechanism has been thoroughly discussed in several theoretical papers [54, 55].

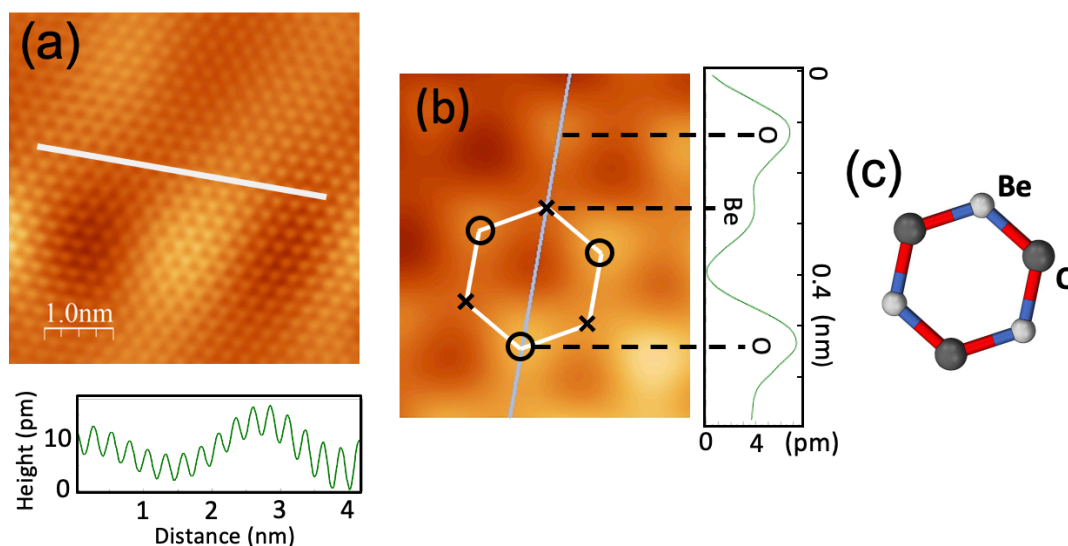


Figure 3.8 (a) Atomic resolution STM image of BeO ($5 \times 5 \text{ nm}^2$), $I_t = 30 \text{ pAmp}$, $V_s = 50 \text{ mV}$. The white line corresponds to the profile below showing the atomic corrugation (b) Zoom in of a honeycomb unit cell showing the Be and O atomic sites. To the right a line cut show the profile of the atomic sites with (c) showing a corresponding schematic of the BeO honeycomb.

In Figure 3.9 (a-f) we utilize LEED to further examine the structure of the h-BeO film. Figure 3.9 (a) shows the sharp hexagonal LEED pattern of the bare Ag(111) substrate, and after the growth of a BeO monolayer, additional spots appear in the pattern. In order to establish that the h-BeO forms across the substrate, LEED patterns were obtained at different locations along the sample surface, indicated by the red dots in Figure 3.9 (b). Figures 3.9 d-f show the LEED patterns of the h-BeO growth, providing additional evidence that the monolayer has a hexagonal structure rotationally aligned with the

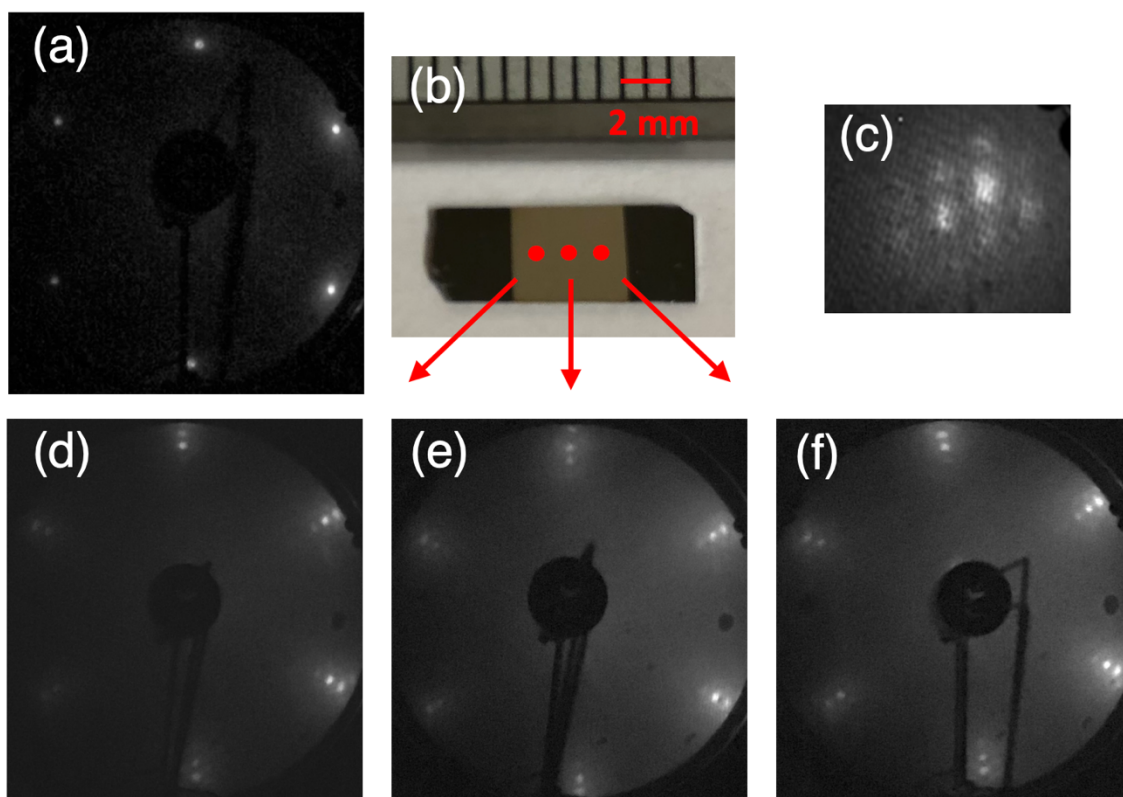


Figure 3.9 (a) LEED pattern from Ag(111) surface acquired at 50 V electron beam voltage. (b) An image of the h-BeO sample on the silicon wafer, where the lighter area in the center is the location of the Si/Ag/BeO heterostructure, $\sim 5 \times 5 \text{ mm}^2$. The red dots indicate the locations of the LEED patterns (d, e, f) acquired with an electron beam energy of 58 V. (c) A zoom-in of the LEED pattern from the rotationally aligned Ag and BeO.

Ag(111) surface. A zoom in of the LEED pattern shows the formation of the moiré pattern (see Figure 3.9 (c)). Each LEED measurement was obtained at a location more than one millimeter apart, suggesting that the h-BeO is a uniform layer across the wafer, similar to the wafer scale growth of graphene and hBN [28, 29]. However, LEED analysis coupled with the local STM imaging cannot rule out the possibility that there might be some local regions that are not covered by the BeO layer.

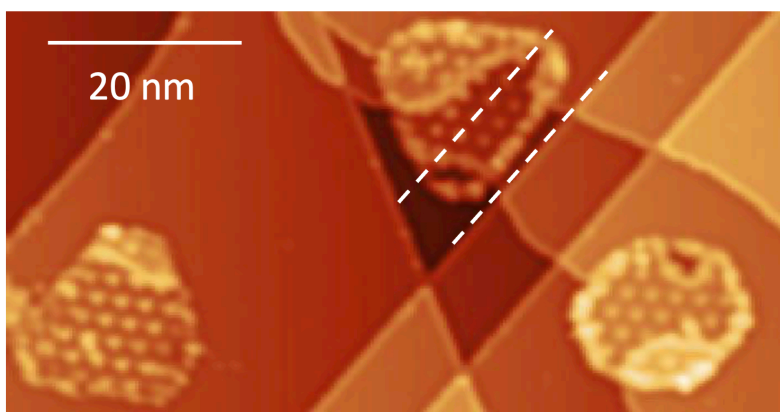


Figure 3.10 STM image acquired at 3.5 V sample bias clearly shows the BeO/Ag(111) moiré pattern rows aligned with the Ag $\langle 110 \rangle$ terrace direction.

We finally use moiré pattern analysis as an indirect method to verify the BeO atomic lattice constant. As previously noted, the hexagonal moiré pattern (see Figure 3.10) has a periodicity of 3.2 ± 0.1 nm and is rotationally aligned with the Ag substrate step along the $\langle 110 \rangle$ direction, which indicates that the Ag(111) and h-BeO lattices are also rotationally aligned [56]. Briefly, moiré pattern periodicity depends on the rotational misalignment and/or difference in lattice periodicity of the overlayer with respect to the substrate [56]. With this knowledge, we can exploit the moiré pattern to determine the h-BeO lattice constant with greater accuracy: with a moiré periodicity of 3.2 nm, and the known lattice constant of 2.89 Å for Ag (111), one can deduce a lattice constant of 2.65 ± 0.01 Å for the h-BeO. This calculated lattice constant is consistent with the atomic resolution measurements, displaying a reduction in BeO bond length compared to bulk wurtzite structure, as theoretically predicted [38, 44, 46, 57-61]. The decrease in lattice constant was previously theorized to stem from the graphitic Be-O bond having an increased covalent character, and as a result the atoms move closer to increase the orbital overlap of nearest neighbors [38, 45, 57].

3.4.3 Long Range Crystallinity

Interestingly, not only do we find that the single atomic sheet can be extended across the whole wafer, but the phase of the atomic registry is also well maintained even across the Ag step. This conclusion is based on analysis of the moiré pattern; small changes in the lattice constants due to defects and strain are greatly magnified by the moiré pattern, making it an excellent tool to gauge the crystallinity of materials [62]. Shown in Figure 3.11 (a) is a topographic image, and (b) the corresponding conductivity image, with the underlying Ag steps marked as N , $N+1$, $N+2$, and $N+3$. The conductivity image (3.11 (b)) eliminates the height difference and planarizes the moiré patterns on different steps, improving the visibility of the pattern. The image is marked with lines to guide the eye to the rows of the moiré patterns at different levels, and across each step one observes an abrupt phase shift (labeled by δ) in the moiré pattern rows. This phase shift δ is roughly $1/3$ of the spacing between the rows (labeled by λ), and the same phase shift is observed across each step, as shown by the model in Figure 3.11 (c). The underlying Ag atomic steps follow an ABC stacking sequence, resulting in a phase shift of $1/3$ between the atomic rows in layer A and layer B (and between B and C) as shown by the stacking model in Figure 3.11 (d). Note that as one follows the blue dashed line across three Ag terraces from N to $N+3$, the moiré pattern rows return to their original alignment. This reveals that the BeO honeycomb lattice preserves the original phase as it continuously rolls across each step, with the shift in the Ag atomic rows creating a phase shift of $\frac{\delta}{\lambda} = \frac{1}{3}$ in the moiré pattern rows, as illustrated by the models (Figure 3.11 (c,d)).

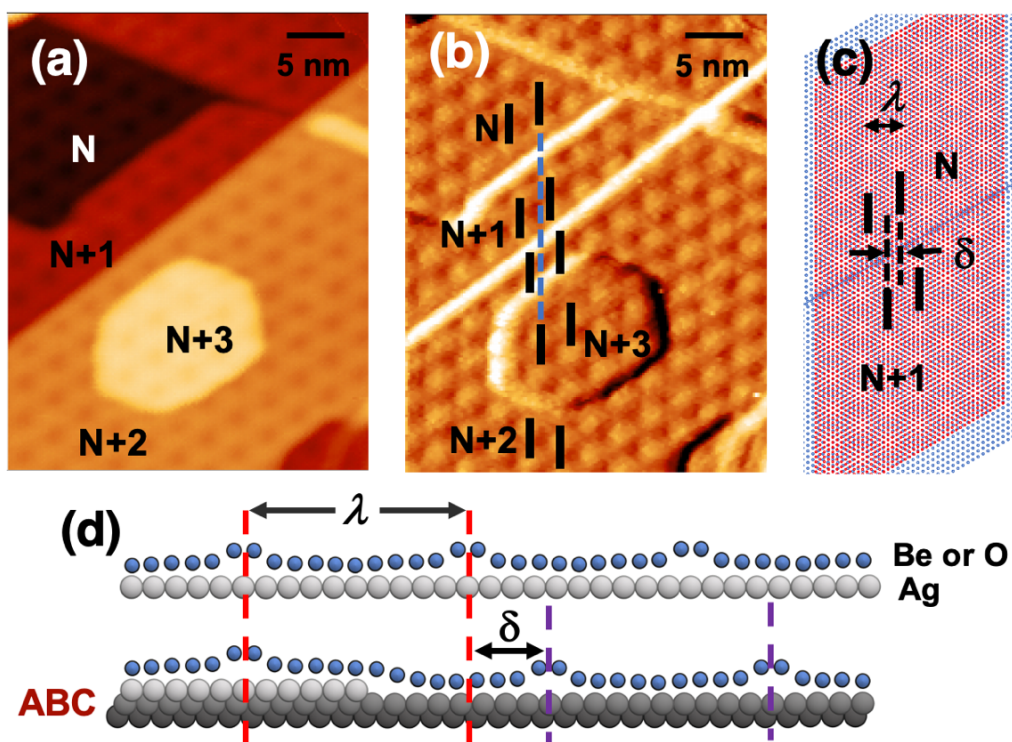


Figure 3.11 (a) A topographic STM image ($32 \times 40 \text{ nm}^2$) of the surface of one monolayer of h-BeO, $I_t = 5 \text{ pAmp}$, $V_s = 4.5 \text{ V}$ and (b) the corresponding conductivity image taken simultaneously by using lock-in. The images show a phase shift of $\delta = \lambda/3$ across the Ag steps, where λ is the spacing of the moiré pattern rows, as indicated by the lines. (c) A model showing that the atomic registry of the BeO is preserved with a phase shift of the moiré pattern due to the ABC stacking of the Ag(111) steps. (d) A model showing a side view of the BeO layer rolling over the Ag steps. The moiré periodicity contains 12 BeO/11Ag(111).

The discovery of the high crystallinity of the h-BeO maintained even across Ag steps is fascinating. The low coverage (0.4 ML) scans in Figures 3.5 (b,c) suggest the nucleation of h-BeO 2D islands occurs in the middle of terraces with an average island-island distance of $\sim 50 \text{ nm}$. Combined with the above analysis, one can conclude that after nucleation in the middle of terraces, the 2D islands grow laterally over the Ag steps, creating a uniform sheet, as indicated by Figures 2.3, 2.6, and 2.9. This combined LEED

and STM analysis amazingly suggests that a complete monolayer is formed as the 2D atomic layer islands merge, the boundary self-heals, maintaining the long-range phase coherence in atomic registry (> 120 nm, as shown in Figure 3.6 (c)). We note that although grain boundaries do occur, they are quite rare for high coverage growth.

3.5 STM/S CHARACTERIZATION OF HONEYCOMB BeO ELECTRONIC PROPERTIES

3.5.1 I-V Spectroscopy: BeO DOS and Interaction with Ag(111) Substrate

Next, we utilize scanning tunneling spectroscopy to study the electronic structure of the h-BeO. The differential conductance (dI/dV) spectroscopy, representing the local density of states (LDOS), is shown in Figure 3.12 (a) with spectra spanning 5 orders of magnitude in dynamic range and displayed in logarithmic scale, acquired at a set bias of 4.1 V. With such a large dynamic range, we can assign the location of the CBM at 3.0 ± 0.2 eV and VBM at -3.0 ± 0.2 eV, corresponding to a bandgap of ~ 6 eV, similar to the value of previous theoretical calculations [38, 47, 57-60]. However, we note that it is difficult to assign the exact locations of the band edges with dI/dV spectroscopy alone. As discussed above, this explains why the layers resemble pristine Ag(111) at low sample bias (Figures 3.5 (b), 3.6 (b)); within the bandgap, the h-BeO does not contribute to the LDOS. At a sample bias above the CBM, (Figs. 3.5(a), 3.6 (c)) tunneling from the BeO layer begins and the islands become visible. To further understand the interaction between the Ag(111) surface and the BeO, tunneling spectra (with a set point bias of 0.8 V, well within the BeO gap) was acquired on the clean Ag (black curve), and on the monolayer BeO surface (red curve), respectively (Figure 3.12 (b)). Interestingly, the Ag surface state is preserved in the BeO region except for an upward shift of 0.12 ± 0.03 eV. This behavior closely resembles that of systems that are weakly interacting via vdW forces, for example hBN and Xe on Cu(111), which shift the Cu(111) surface state upward by ~ 0.1 eV [63, 64]. The

preservation of the Ag (111) surface states is strong evidence that similarly, the h-BeO layer is weakly interacting with the Ag substrate.

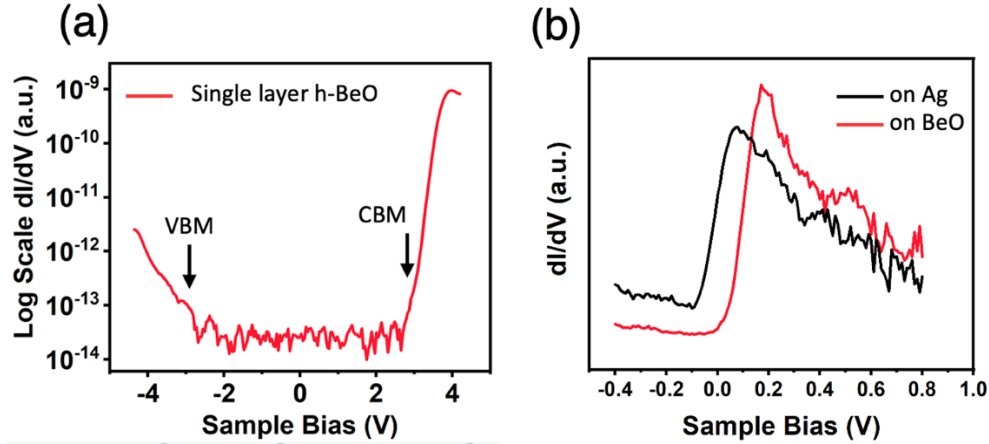


Figure 3.12 (a) Log scale dI/dV tunneling spectra acquired on the h-BeO layer at a set point bias voltage of 4.1 V, showing a bandgap of ~ 6 eV. (b) dI/dV tunneling spectra of the Ag surface states acquired on a single sheet of h-BeO (red curve) and on the Ag surface (black curve) at a set point bias of 0.8 V. Note that the Ag surface state is preserved with the addition of the h-BeO, with a slight upshift in energy.

3.5.2 Z-V Spectroscopy: Moiré Modulation of Work Function

As mentioned before, the observed h-BeO/Ag(111) moiré pattern displays a peculiar bias dependent contrast reversal, as shown in Figures 3.5 and 3.6. This implies that the moiré patterns not only introduce a change in height corrugation, but also a spatial modulation of the electronic character. Here we adopt the terminology used in this field and call different regions in the moiré pattern “hole” and “wire” regions, as labeled in the inset of Figure 3.13 (a). Figure 3.13 (b) is an STM image that illustrates the contrast reversal of the h-BeO that shows the hole region (white dashed line) changing from a protrusion to a depression when the bias was changed from $V_s = 3.7$ V (top) to 4.5 V (bottom). To investigate the contrast mechanism, we use Z-V spectroscopy to examine the

field emission resonance (FER), as the sample bias of the first FER is a good approximation for the local work function, and this phenomenon has been thoroughly discussed in the literature [25, 26]. As discussed in Chapter 2, in this spectroscopic technique, the tunneling current is held constant while the tip-sample distance (Z) *versus* bias sweep is recorded. When the bias reaches the tunneling barrier resonance, a steep increase in Z occurs, therefore peaks in the derivative $(\partial Z/\partial V)_I$ denote the locations of the FER. Figure 3.13 (a) shows the Z - V (top) spectra and their derivatives $(\partial Z/\partial V)_I$ (bottom) acquired at the hole region (red curve) and wire region (blue curve). We find that energy locations of FER in the hole region are consistently lower than those in the wire regions by about 0.08 eV, suggesting that the local work function is modulated across the moiré pattern. In addition, comparison of the h-BeO $(\partial Z/\partial V)_I$ spectra with spectra obtained on an Ag(111) surface (black curve) shows the h-BeO layer reduces the work function. A closer look at the work function modulation explains the variation of the moiré pattern contrast observed by STM (Figure 3.13 (b)). In Figure 3.13 (c), we plot the tip height difference between the hole and wire regions directly deduced from the Z - V curves in Figure 3.13 (a) and find that the positive values indicate the bias range where the hole regions appear as a protrusion, while at negative values it becomes a hole. We note that this work function behavior closely mirrors the trends observed for hBN on transition metals [63, 65-68], providing further evidence that the interaction of the h-BeO and Ag(111) is similar to a vdW interface.

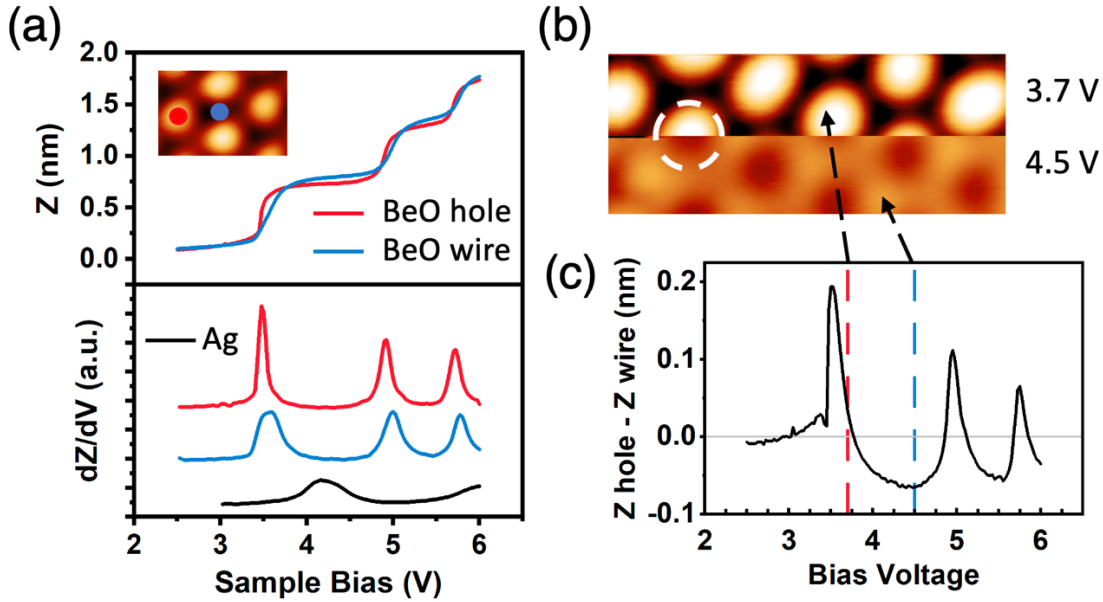


Figure 3.13 (a) The inset shows the “hole” (red dot) and “wire” (blue dot) regions of the h-BeO moiré pattern. The top graph shows vertical tip position (Z) as a function of the sample bias at constant current, and the bottom graph shows the corresponding dZ/dV spectra acquired at the hole and wire regions. (b) STM image (area: $15 \times 6 \text{ nm}^2$) acquired at a sample bias of 3.7 V (top) and 4.5 V (bottom) showing a contrast reversal between the hole and wire regions. (c) The relative difference of the vertical tip height between the hole region and wire region with positive values indicating bias where the hole becomes bright, and negative values where the wire is bright.

3.6 FIRST PRINCIPLES CALCULATION OF BeO/Ag(111) HETEROSTRUCTURE

To further understand the BeO/Ag interaction, we have performed first-principles calculations using a supercell consisting of 12×12 unit cells of monolayer honeycomb BeO on 11×11 unit cells of Ag(111), which gives rise to a 3.17-nm moiré pattern (see Appendix D for calculation methods). The optimized structure is shown in Figure 3.14 (a), with regions marked by black, blue, and orange circles to represent the local stacking patterns of $\text{Be}_{\text{fcc}}\text{O}_{\text{hcp}}$, $\text{Be}_{\text{top}}\text{O}_{\text{fcc}}$, and $\text{Be}_{\text{hcp}}\text{O}_{\text{top}}$, respectively. This notation describes the locations of the Be and O atoms with respect to the surface sites on Ag(111); for example, $\text{Be}_{\text{fcc}}\text{O}_{\text{hcp}}$ corresponds to the configuration with Be at the fcc site and O at the hcp site. Due to the

spatial variation of the stacking pattern, the interaction of the h-BeO layer with the Ag substrate varies within the moiré cell. As a result, the BeO-Ag interlayer distance fluctuates with a height corrugation from 3.02 to 3.47 Å which is a reasonable separation for a vdW interaction and agrees well with our measurements. The average height of each marked region is shown in Figure 3.14 (a), with the height of the black region set as the zero point. The orange region ($\text{Be}_{\text{hcp}}\text{O}_{\text{top}}$) with O on top of Ag has the strongest interaction and corresponds to the “hole” region seen in the STM scans. However, the separation between the BeO layer and the topmost Ag layer varies only slightly across the moiré cell and is larger than 3 Å everywhere. This is very different from other cases such as h-BN/Ru(0001) [66], where a smaller separation is found for the “hole” region, and calculations identified a noticeable charge transfer induced by the interaction. We have also checked the projected density of states onto Be and O atoms for both the freestanding BeO monolayer and BeO on Ag(111). The valence band profiles are similar, and no gap states induced by interaction are found. We further investigate the local work function variation along the diagonal of the supercell from left to right in Figure 3.14 (b). The work function values at black, blue, and orange regions are 4.26, 4.28, and 4.19 eV, respectively, which correlates to a modulation between the hole and wire region of roughly 70 – 90 meV and is consistent with the STM observation of 80 meV using barrier resonances as discussed above.

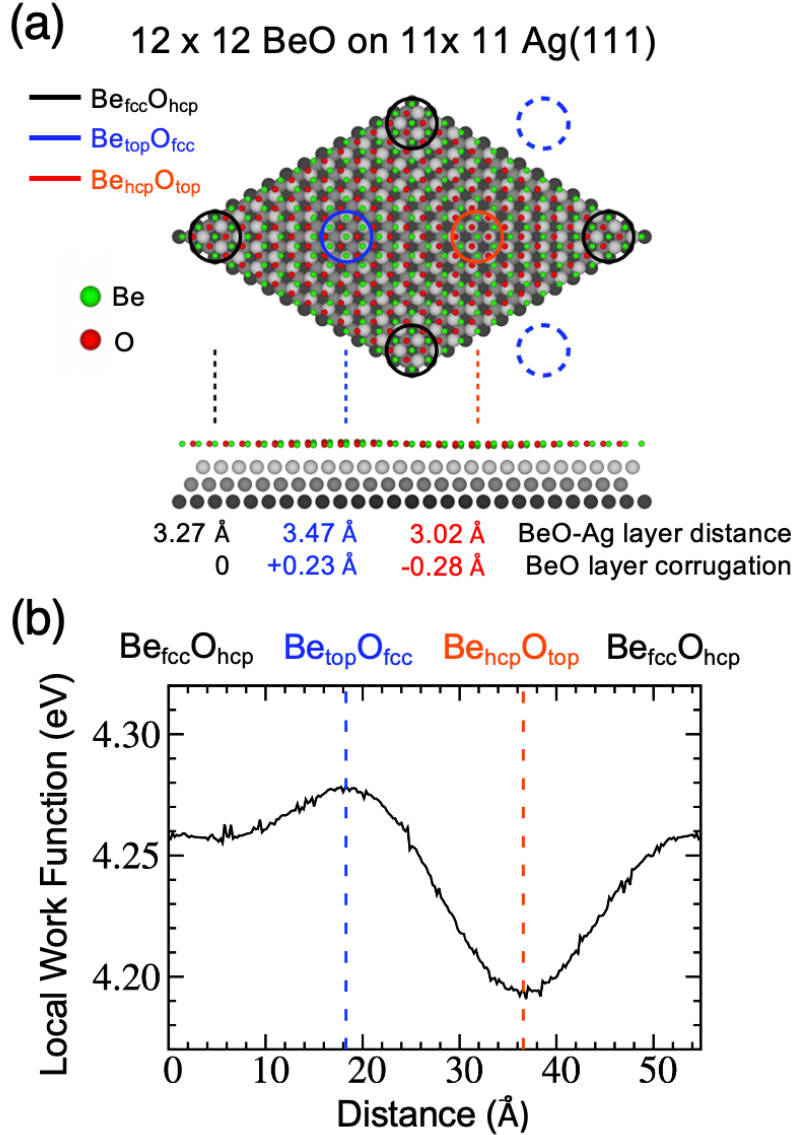


Figure 3.14 (a) Top and side views of a supercell containing 12x12 h-BeO/11x11 Ag(111) used to simulate a 3.17-nm moiré pattern. The green and red spheres represent Be and O atoms, respectively. The 1st, 2nd, and 3rd layers of Ag atoms are illustrated by gray spheres with different darkness. High symmetry stacking regions of $\text{Be}_{\text{fcc}}\text{O}_{\text{hcp}}$, $\text{Be}_{\text{top}}\text{O}_{\text{fcc}}$, and $\text{Be}_{\text{hcp}}\text{O}_{\text{top}}$ are marked by black, blue, and orange circles, respectively. The dashed blue circles indicate the $\text{Be}_{\text{top}}\text{O}_{\text{fcc}}$ regions in the neighboring moiré cells. The BeO-Ag interlayer distance and the h-BeO layer corrugation are also shown at the bottom. (b) Calculated local work function along the diagonal of the supercell shown in (a).

3.7 CONCLUSION AND FUTURE OUTLOOK

In summary, this work represents the compelling demonstration of the epitaxial monolayer growth of the graphitic phase of BeO by MBE, and also the direct characterization of the h-BeO atomic structure and electronic properties by STM/S. We find an h-BeO lattice constant of $2.65 \pm 0.01 \text{ \AA}$, and that the h-BeO surprisingly displays a nearly perfect atomic registry even across Ag steps like true vdW atomic layers. Previous studies of other wurtzite structure materials such as ZnO have shown that monolayers are observed at a local scale of a few tens of nm laterally, and exhibit multilayer, polycrystalline growth at higher coverage [41-43]. In contrast, our LEED and STM measurements suggest the astonishing formation of wafer scale coverage of a single atomic sheet of honeycomb BeO that maintains long-range phase of the atomic lattice. In our case, the growth appears to saturate at a monolayer, with prolonged deposition leading to the formation of clusters with a significantly lower growth rate (more than a factor of 20). This suggests that the Ag(111) substrate may play a critical role in stabilizing the growth. Yet another similarity to vdW materials is the preservation of the pristine Ag (111) surface electronic structure, indicating a weak interaction with the h-BeO atomic sheet, an assertion that is supported by our complimentary DFT calculations. We note that the size of our Si substrates is constrained by our sample holders, which are limited by the STM sample stage. Considering the h-BeO is directly grown on epitaxial Ag films on Si wafers, such a method may be translated to a larger growth format, providing a powerful scalable technology platform. The large insulating band gap of 6 eV and weak substrate interactions of the h-BeO make it an attractive candidate for multilayer heterostructures and as a template to support other 2D materials. We expect that our work demonstrates that insulating h-BeO is a valuable addition to the library of 2D materials and will create future

possibilities for bottom-up fabrication of 2D devices. These results are summarized in a manuscript published in *ACS Nano* [8].

Chapter 4

Sulfur Vacancy Defect-Defect Interactions in Monolayer WS₂

4.1 INTRODUCTION AND BACKGROUND

Within the family of 2D materials, transition metal dichalcogenides (TMDs) have gained much research interest due to their potential for filling the semiconductor role in 2D devices. The critical role defects play in modifying semiconductor electronic properties is best demonstrated by the example of silicon, where defects have been both detrimental by limiting device performance, and beneficial as a tool to engineer the electronic properties. TMDs have many attractive mechanical, electronic, and optical properties arising from their extreme 2D nature [69], and it comes as no surprise that the strong confinement and reduced screening leads to their electronic properties having a strong sensitivity to defects [70-72]. A number of different intrinsic atomic defects have already been experimentally observed in TMDs [61, 73-79], and connecting each of these defects with their related impact on the TMD electronic properties is critical to further the field of TMD defect engineering. However, nanoscale atomic characterization of defects and direct measurement of their electronic properties is difficult to achieve in tandem experimentally, therefore many unanswered questions still remain.

Of the possible defects in TMDs, chalcogen vacancies are shown to be the most energetically favorable with the lowest formation energy [78, 80-84], and therefore were predicted to be the most abundant intrinsic defect. This makes understanding chalcogen vacancies a natural starting point in creating the foundation for defect engineering. Chalcogen vacancies were predicted to introduce deep in-gap states (IGS) that are highly

localized, which can strongly affect the TMD optoelectronic and transport properties [81, 83-93]. Experimental studies have attributed a variety of features in transport characteristics [94, 95], catalytic activity [96-100], and optical response [61, 87, 101-103] as signatures of IGS from chalcogen vacancies, but fail to directly show the defect atomic structure concurrently. Instead, the defect structure is investigated in separate measurements by STM or transmission electron microscopy (TEM). However, a recent STM study of WS₂ found that the most abundant defect was actually oxygen passivated sulfur vacancies, which show no IGS [76]. This raises the question of whether chalcogen vacancies are stable in atmosphere, and could be present during experiments (optical, transport, catalytic) that were conducted in ambient conditions. Further, many studies rely on TEM measurements to characterize intrinsic defects, but TEM does not provide information about the electronic structure, and it is well known that TEM actually creates chalcogen vacancies due to radiation damage of the sample [73, 80, 104-106]. In order to obtain a comprehensive understanding of chalcogen vacancies, an approach of controlled creation of vacancies in ultra-high vacuum and *in situ* characterization of atomic and electronic structure is required.

This technique was employed in a recent study by Schuler et. al., by first creating chalcogen vacancies in vacuum then characterizing them *in situ* using STM [74]. First, sulfur vacancies were introduced by thermal annealing the WS₂ sample in UHV (Figure 4.1 (a)), which has become a popular approach to conveniently create chalcogen vacancies in TMDs in a controlled manner [107-110]. STM images also showed darker defects, which were previously reported to be oxygen passivated chalcogen vacancies [76]. Schuler et. al. interestingly showed that sulfur vacancies give rise to two unoccupied deep IGS near the CBM (Figure 4.1 (b)), and the origin of these states will be discussed in detail later. The verification that chalcogen vacancies lead to IGS opens an intriguing question: how do these defects

interact at higher concentrations? Theoretical studies have shown that high vacancy defect density affects the TMD optical and transport properties [92, 94], and result in an increase of in-gap states, ultimately leading to an in-gap defect band [98, 103, 111, 112]. Further, theoretical studies have shown that in general, if two of the same defect have localized in-gap states and are close together, the states will hybridize and increase the total number of in-gap states [113]. This was predicted to occur with S divacancies in WS_2 , but the impact of chalcogen vacancy interactions has yet to be observed experimentally and invites further exploration [87, 88].

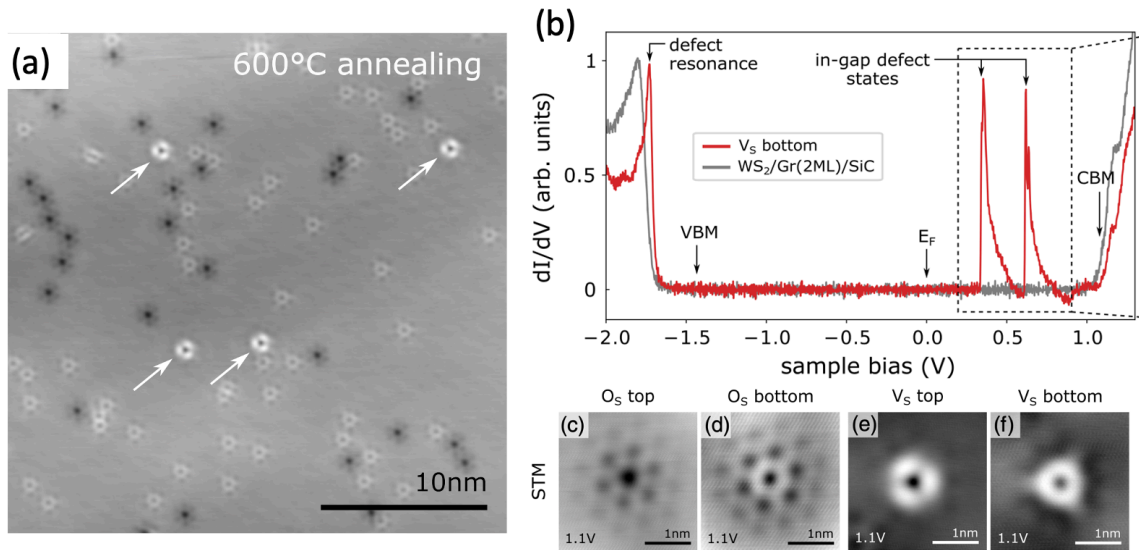


Figure 4.1 (a) STM image of WS_2 after thermal annealing showing different defects (b) dI/dV spectroscopy on the vacancy shows two IGS (c) oxygen passivated top vacancy (d) oxygen passivated bottom vacancy (e) top s vacancy (f) bottom S vacancy. Images taken from Ref. [109].

Here we report the incorporation of a high concentration of S vacancy defects in WS_2 monolayers by vacuum annealing, and characterization of their electronic properties and structure using scanning tunneling microscopy and spectroscopy. We find that the interaction of nearby S vacancies results in a rich variety of deep in-gap states, shedding

light on how vacancy interactions influence TMD electronic properties. This indicates that vacuum annealing provides a method for defect engineering that can be a useful tool to controllably manipulate the electronic properties of 2D materials.

4.2 WS₂ UHV THERMAL ANNEALING

The WS₂ sample was grown by chemical vapor deposition (CVD) on sapphire substrates in a horizontal hot-wall CVD chamber using a one-pot synthesis as outlined in Refs. [114, 115]. In brief, high purity WO₃ (99.995%, Aldrich) and S (99%, Aldrich) powders were used as precursors. The sapphire substrate and WO₃ powder were placed in the central heating zone, with the S heated upstream separately with a heat tape. The growth temperature was ~920 °C and Ar/H₂ gas was flowed at a rate 60/6 sccm at 5 Torr, and after the growth the temperature was slowly lowered to room temperature, and Figure 4.2 (a) shows an optical microscope image of the micrometer scale WS₂ islands. A conductive substrate is necessary for the tunneling in STM measurements; to address this issue, the sample was transferred from the sapphire growth substrate to a highly oriented pyrolytic graphite (HOPG) substrate via a wet transfer method. First the sample was spin coated with poly(methyl methacrylate) (PMMA) and submerged in water to isolate the PMMA, pulling the WS₂ flakes from the sapphire substrate. The PMMA layer then floats at the top of the water, and can be lifted onto a HOPG substrate. The sample was annealed on a hot plate at 90 °C for 15 minutes, followed by heating the sample in acetone at 90 °C for an hour. The PMMA is then rinsed from the sample using IPA and water, and finally annealed at 90 °C another 15 minutes, and Figure 4.2 (b) shows an optical image of the transferred HOPG/WS₂ sample. The WS₂ sample was then put into a UHV chamber with a heat stage for vacuum annealing. This annealing served two important purposes: first to remove the

contamination left by the transfer process, and second to create a high enough concentration of sulfur vacancies to observe defect-defect interactions.

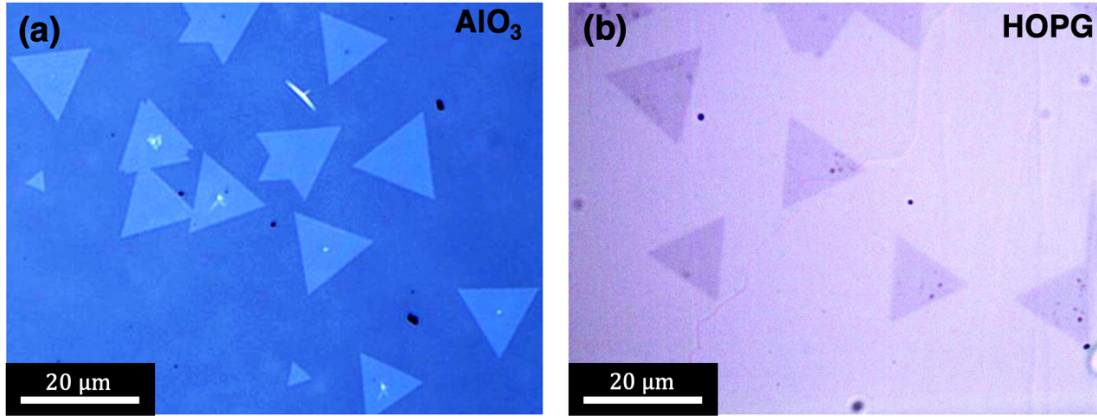


Figure 4.2 (a) Optical image of CVD grown WS_2 on AlO_3 (b) optical image of the WS_2 sample transferred to HOPG.

The WS_2 was gradually annealed during multiple cycles, slowly increasing the temperature incrementally to avoid evaporation or serious damage to the crystal. We note that although the following images show clean areas on the crystal surface, the polymer residue of the transfer process was never completely removed. Figure 4.3 (a) is an STM image of the sample after annealing at 250 °C that shows a layer of adsorbates covering surface, and we attribute this layer to polymer residue left over from the transfer process. After thermal annealing at a higher temperature of 380 °C (Fig. 4.3 (b)), clean areas on the WS_2 surface become visible. Figure 4.3 (c) shows a zoom in image of one of these clean areas, which reveals the appearance of a variety of point defects. After further annealing at 460 °C (Fig. 4.3 (d)), there was a dramatic increase in the defect density, with bright clusters forming on the surface. As noted in Section 2.3.1, constant current STM measurements are a convolution of the topography and the LDOS of the sample. Thus, the composition of these clusters is unclear, as they could be an agglomeration of defects leading to a higher LDOS, or small clusters of residue left on the surface. Taking

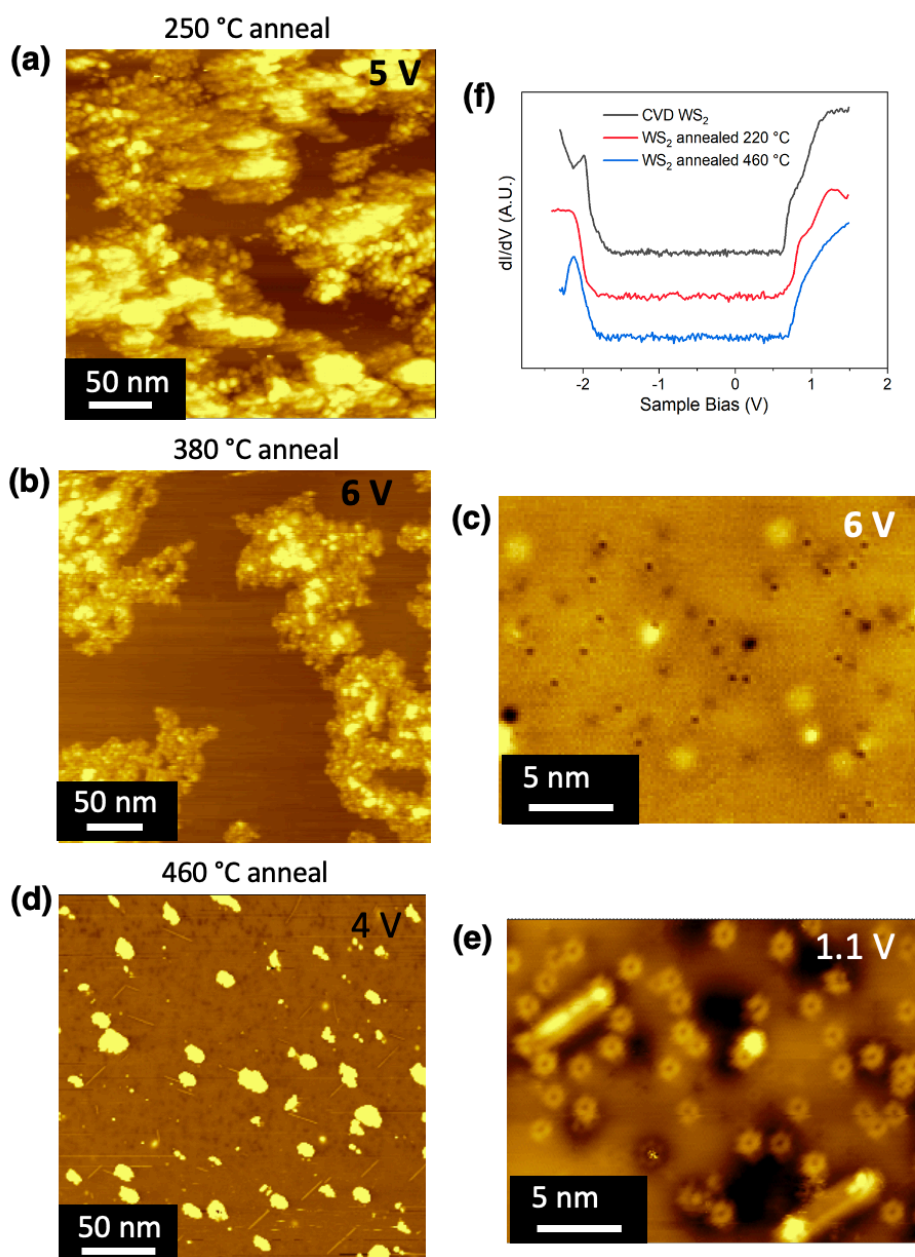


Figure 4.3 (a) An STM image of WS₂ after a 250 °C thermal annealing shows polymer residue on the surface (b) After a 380 °C anneal clean areas appeared (c) a zoom in image at (bias) shows defects have emerged (d) further annealing at 460 °C (e) a zoom in image of showing an increase in the defect density (f) dI/dV spectroscopy of the WS₂ away from defects shows that the bandgap is not changed (red, blue) compared to a different sample grown direction on HOPG without annealing (black). Sample bias (a) 5 V, (b) 5 V, (c) 6 V, (d) 4 V, (e) 1.1 V

a closer look at the WS₂ surface, it is apparent that the high temperature annealing not only increased the density of point defects, but also resulted in the formation of line defects. Note that the STM images in Figures 4.3 (c) and (e) were taken with different sample bias conditions, therefore the point defects we attribute to sulfur vacancies appear as small dark circular defects in (c) and the bright circular defects in (e). After careful analysis of the STM images we find that the defect density after the 380 °C and 460 °C anneal was $2.7 \times 10^{12} \text{ cm}^{-2}$ and $7.7 \times 10^{12} \text{ cm}^{-2}$, respectively. However, only single sulfur vacancies were included in the calculation of the defect density for the 460 °C anneal, which leaves out the contribution of the defect clusters and line defects. As we will see, it is difficult to determine the number of vacancies contributing these larger agglomerate defects, so this reported concentration is certainly an underestimation.

We also investigated how the introduction of sulfur vacancies impacted the electronic structure of the WS₂ crystal. Figure 4.3 (f) shows STS obtained from pristine areas of the WS₂ far away from defects after the initial 220 °C anneal (red) and the final 460 °C (blue) anneal. Upon close examination, the band gap size and Fermi level position appear nearly the same, which indicates that the increase in sulfur vacancy concentration did not dope the sample. In addition, we compare these dI/dV spectroscopy curves with STS taken on a different WS₂ sample that was directly grown on HOPG by CVD (black), and we see that the bandgap of this pristine as-grown sample is very similar to that of our transferred and annealed sample. This result contradicts a prior report that the incorporation of chalcogen vacancies in TMDs causes n-type doping [90, 116]. However, the MoS₂ sample used in this study was supported by an Au substrate, and other investigations have found that that defect-substrate interactions affect the TMD electronic structure [117, 118]. Nevertheless, more investigations into the details of substrate-defect interactions are needed, although it is outside the scope of this study.

4.3 WS₂ DEFECT CHARACTERIZATION

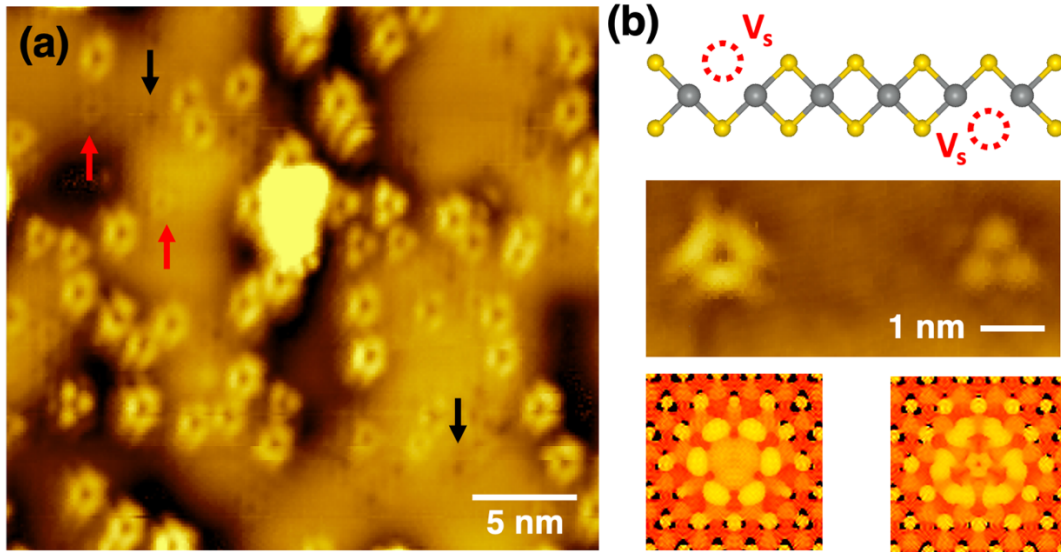


Figure 4.4 (a) STM image of a the WS₂ showing a variety of different defects including oxygen passivated top S vacancies (red arrows), oxygen passivated bottom S vacancies, and S vacancies (b) a schematic showing top and bottom S vacancies, STM image of top (left) and bottom (right) S vacancies, and a DFT simulation of STM images of top (left) and bottom (right) S vacancies. STM images taken at a sample bias of 1.1 V.

We next take a closer look at the variety of defects that formed during the annealing process (see Appendix A for STM methods). Figure 4.4 (a) is STM image obtained at 1.1 V sample bias that shows a high concentration of defects with different geometries and contrast. Two defects with lower contrast, marked by the red and black arrows for clarity, show a circular pattern of dark spots. These defects are top (black arrow) and bottom (red arrow) oxygen passivated sulfur vacancies that were previously reported by Barja et. al. [76]. These passivated vacancies do not contribute IGS, hence the dim contrast next to the pristine WS₂ surface. In comparison, the sulfur vacancies are more apparent, with three bright trifold symmetric lobes. These bright lobes are actually the localized IGS; inspecting the vacancy dI/dV spectroscopy (Figure 4.4 (b)), it becomes clear that at 1.1 V sample bias

the IGS strongly contribute to the tunneling, resulting in a brighter contrast. The three lobes of the top vacancy (left) and bottom vacancy (right) are rotated with respect to each other (Figure 4.4 (b)), and this difference in appearance stems from the lack of mirror symmetry of the defect orbitals with respect to the tungsten plane. A simulated STM image that was calculated by DFT (bottom of Figure 4.4 (b)) matches the differing geometry of the top and bottom sulfur vacancies.

4.3.1 Defect Geometry

This initial look at the sulfur vacancies elucidates the difficulty in determining the defect morphology using STM analysis, because STM contrast is dominated by the LDOS. Some defects lead to a dramatic increase in spatially localized electronic states, therefore teasing apart the physical geometry of the underlying atomic structure with STM alone is a challenge. Before we discuss the defect orientation, we note that we will use the terminology of the field, by calling the $\langle\bar{2}11\rangle$ and $\langle 0\bar{1}1\rangle$ directions the “zigzag” and “armchair” directions, respectively, as shown in the bottom of Figure 4.5 (c). Further, we note that atomic resolution STM images show the top chalcogen atoms of the TMD, and that the lattice constant of WS_2 is ~ 0.32 nm. Figure 4.5 (a) shows an atomic resolution STM image of a sulfur top vacancy, which illustrates that the defect orbitals follow the zigzag direction of the TMD atomic lattice. A DFT orbital density calculation (left of Figure 4.5 (b)) clarifies that the “lobes” of the sulfur vacancy reflect states that are localized about the tungsten atoms adjacent to the missing sulfur atom. Figure 4.5 (a) and (b) (right) shows top vacancies from the same WS_2 island with and without atomic resolution, (respectively), with lobes oriented in the same direction. This illustrates that the defect lobe orientation can be exploited to roughly determine underlying atomic lattice without atomic resolution images. Figure 4.5 (c) shows a zoom in image of the defects from Figure 4.4 (a)

with increased contrast, and although the atomic corrugation is not visible, one can infer the zigzag direction of the atomic lattice from the vacancy orbital orientation (Figure 4.5 (c) black line). Further, the dark spot pattern of the oxygen passivated sulfur vacancies is centered on the missing sulfur atom, and the surrounding spots also follow the zigzag direction of the atomic lattice (Figure 4.5 (c) red line). Comparison with a schematic of the corresponding WS_2 crystal lattice (Figure 4.5 (c) bottom), shows that the geometry of the known defects can aid in the identification of the atomic structure of other unknown defect geometries as discussed later.

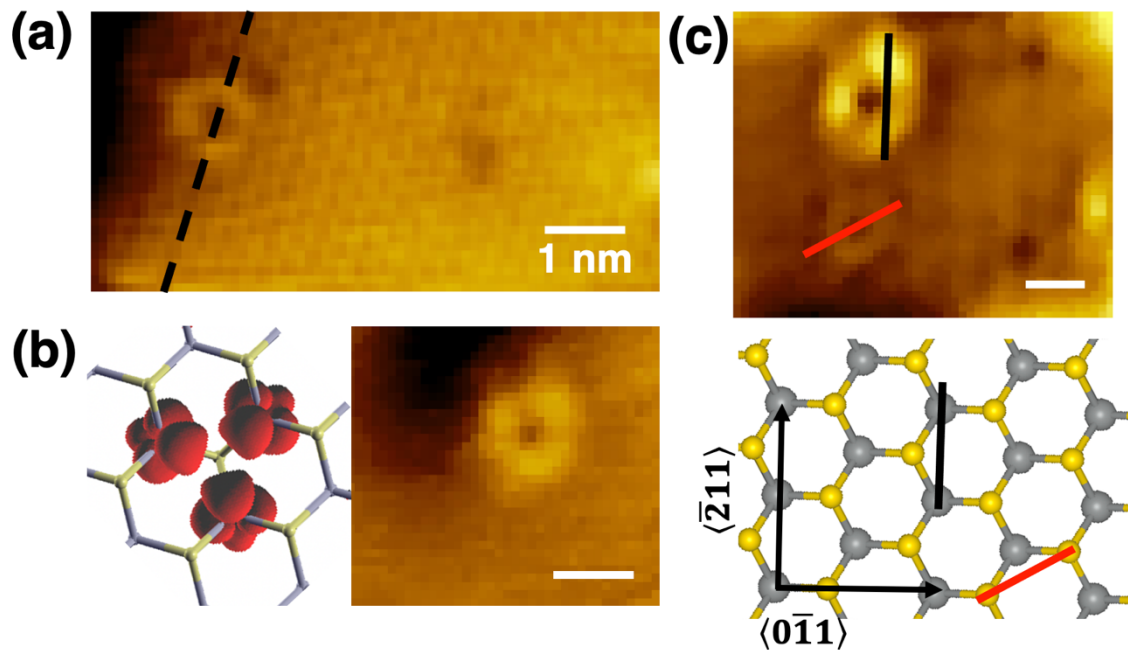


Figure 4.5 (a) Atomic resolution STM image (b) right STM image from the same area as (a) without atomic resolution, left shows a corresponding orbital density calculation which shows the defect orbitals are centered on the surrounding W atoms (c) STM image showing the S vacancy orbital lobes (black line), and black spots of the oxygen passivated vacancies (red line) can be used to roughly determine the zigzag direction of the atomic lattice. The white scale bars are all 1 nm. STM images taken at a sample bias of 1.1 V.

4.3.2 Defect Electronic Properties

We further probed the electronic structure of the single S vacancies to verify that the behavior matched the prior report of two IGS near the valence band edge (Fig. 4.1), as discussed above [109]. Using STS dI/dV spectroscopy, we established that the S vacancies do indeed result in two resonances at the conduction band edge (Fig. 4.6 (a)). Interestingly, we noticed that the IGS peak position differed on some defects, with the valence band edge states shifted to higher values (Figure 4.6 (a) blue curve). Schuler et. al. reported a similar shift in both the IGS and valence band edge energies when WS_2 was on one monolayer Gr/SiC substrates versus a bilayer Gr/SiC substrate (Figure 4.6 (b)). Surprisingly, a comparison between the energies of our observed shifted S vacancy IGS and the IGS reported by Schuler et. al. shows they are nearly identical, as indicated by the black dashed lines. This behavior was attributed to bandgap renormalization due to the change in substrate screening from the monolayer and bilayer graphene, as well as a change in the substrate work function [119, 120]. It is interesting that we observe a similar result for defects at different locations on the same sample, with the same substrate. However, it is likely that the transfer process results in debris trapped at the WS_2 /HOPG interface, leading to a nonuniform dielectric environment [121].

In addition, the spectra obtained on the WS_2 on the bilayer Gr/SiC substrate show an additional peak at negative bias due to defect charging. In brief, tip induced band bending occurs when the STM tip is brought near a semiconductor, and the degree of bending increases with the increase in sample bias, and when the tip-sample distance is decreased [122]. This effect can push the unoccupied defect state below the substrate Fermi level, and then the state can be filled with an electron, negatively charging the defect [123]. Thus, a “charging peak” occurs when a bias is reached at which the empty state has been pulled low enough to become charged. Surprisingly, our data shows no such peak, though

the characteristic shift in the IGS was reproduced. One possible explanation is that the defect remains charged after the initial charging event, as the nature of our transferred WS_2/HOPG interface is different than the as grown $\text{WS}_2/\text{Gr}/\text{SiC}$. Another possibility is that the tip induced band bending in our WS_2/HOPG system is not pronounced enough for defect charging to occur. Regardless, we believe the root cause of this behavior lies in the difference in substrate-sample interface for transferred samples versus as-grown.

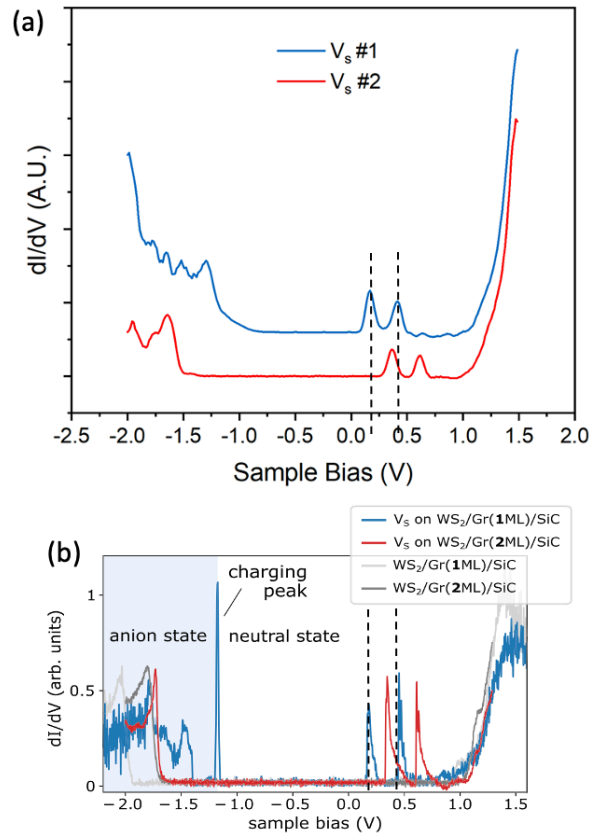


Figure 4.6 (a) STS dI/dV measurements taken on different S vacancy defects (red, blue). The IGS peak location is shifted, as well as the VMB location. (b) dI/dV measurements taken from Ref. [109] showing an almost identical shift for a WS_2 sample on a 1 ML Gr/SiC (blue) and a 2 ML Gr/SiC (red) substrate. We attribute this shift to a change in the dielectric environment at different locations of the sample.

4.4 UNDERSTANDING TMD CHALCOGEN VACANCY ELECTRONIC STRUCTURE

4.4.1 Crystal Field Theory

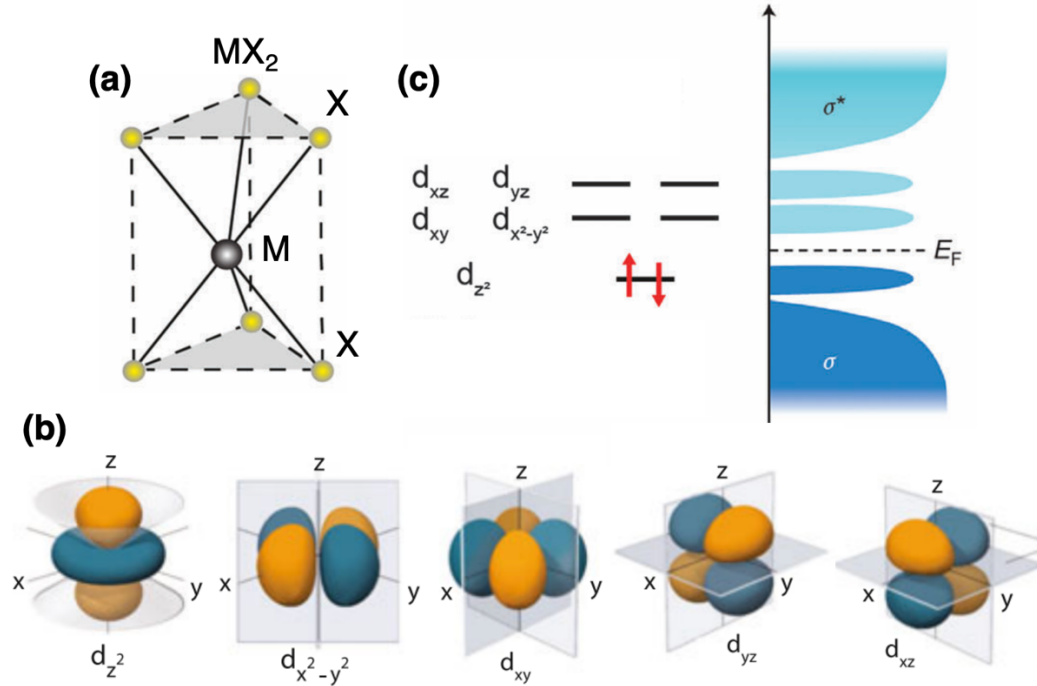


Figure 4.7 (a) Schematic of the trigonal prismatic geometry of the TMD H phase, where M represents the transition metal and X represents the chalcogen. (b) Schematic of the five degenerate transition metal d orbitals (c) Schematic showing the change in energy of the d orbitals due to crystal field splitting. Images taken from Ref. [124] (a), Ref. [125] (b), and Ref. [126] (c).

To investigate the origin of the IGS of chalcogen vacancies in TMDs, we start by considering the character of the pristine TMD band structure. For group VI TMDs, described by the general formula MX_2 ($M = \text{Mo}$ or W , $X = \text{S}$ or Se), the most stable structure consists of a transition metal atom (M) surrounded by six chalcogen atoms (X) in the trigonal prismatic coordination, which forms the so called H phase (Figure 4.7 (a)) [127]. One can gain a better understanding of how this geometry affects the electronic structure of the TMDs by applying crystal field theory. The five transition metal d orbitals

initially have degenerate energies, and each orbital has a distinct spatial orientation (Fig. 4.7 (b)). When the transition metal atom is put in a “ligand field” consisting of six chalcogen atoms (Fig. 4.7 (a)), the electrostatic repulsion from the chalcogen electron clouds will increase the energy of the transition metal d orbitals depending on the degree of orbital overlap. Thus, the resulting d orbital energies depend on the orbital geometry, as this determines the amount of chalcogen overlap. Accordingly, the three resulting energy bands in order of increasing energy are: singlet d_{z^2} , and doublets $d_{x^2-y^2}/d_{xy}$, and d_{xz}/d_{yz} as shown by the schematic in Figure 4.7 (c) [124, 126]

4.4.2 TMD Band Structure

Although crystal field theory provides an extremely simple picture to explain the orbital character of the band edges of the TMDs, rigorous first principles theoretical calculations verify the findings of this intuitive approach. DFT calculations show that the orbitals providing the main contribution to the valence and conduction band edges are the transition metal d orbitals. Figure 4.8 (a) shows the generic TMD band structure calculated by DFT, and although the bands are hybridized with the chalcogen p orbitals, the band edge character is dominated by the transition metal d_{z^2} , $d_{x^2-y^2}$, and d_{xy} orbitals [128]. We note that these orbitals are hybridized, and all contribute to these bands, while the decoupled d_{xz}/d_{yz} bands lie at higher energies. Further, a basic three band tight binding model that only considered transition metal hopping closely reproduced the energy band edges of TMDs (Figure 4.8 (b)), further driving home the point that the transition metal atoms rule the electronic character of the TMD band edges [129].

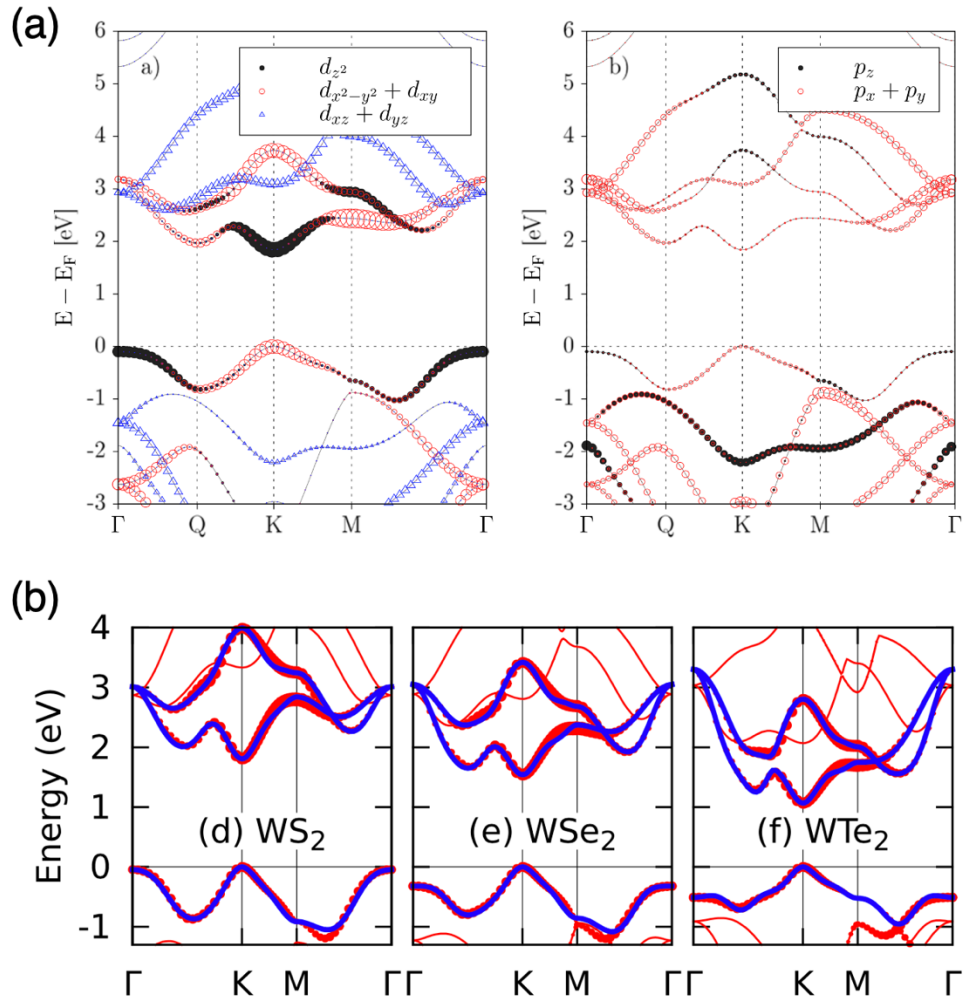


Figure 4.8 (a) First principles calculation of a generic band structure for TMDs showing the orbital contribution of the transition metal d (left) and chalcogen p orbitals (right) (b) TMD band structure calculated by a tight binding only including transition metal hopping (blue) overlaid on first principles DFT calculation of the band structure. Images were taken from Ref. [128] (a) and Ref. [129] (b).

4.4.3 Spin-Orbit Coupling

Another defining characteristic of the TMD electronic structure is the strong influence of spin-orbit coupling (SOC). When TMDs are reduced to a single monolayer, the space inversion symmetry is broken, and this results in a split in energy of the different

spin states due to SOC [130, 131]. This effect is caused by the electromagnetic interaction between the magnetic dipole of the electrons and the electrostatic field of the nucleus, therefore the splitting increases with atomic number. In addition, this implies that the orbitals with a magnetic quantum number equal to zero and no magnetic moment do not experience splitting. Therefore, the degenerate doublets $d_{x^2-y^2}/d_{xy}$, and d_{xz}/d_{yz} will split, while the singlet d_{z^2} does not, and this effect is most dramatic in W based TMDs.

4.4.4 Chalcogen Vacancy In-Gap States

Now that we have established a foundation of the main elements determining the TMD electronic structure, the d orbital character and SOC, we can consider the scenario of removing a chalcogen atom to create a vacancy. One important question is what specific characteristics determine whether a TMD chalcogen vacancy will have deep IGS. Pandey et. al. investigated this question theoretically by systematically comparing chalcogen vacancies in group IV and VI TMDs [93]. They found that TMDs with valence and conduction bands edges with similar orbital composition (group VI) have IGS, while TMDs different orbital character at the valence and conduction bands (group IV) do not. Similar orbital composition at the band edges suggests that the band gap opens due to a bonding and anti-bonding nature, where combinations of sulfur p and metal d states at energies lying within the band gap have bonded. Thus, when a chalcogen is removed, the dangling bonds (localized states) will fall within the gap. This idea further illustrates that the defect “lobes” imaged by STM in Figures 4.4 and 4.5 can be thought of as a visualization of the dangling bonds left after a chalcogen atom is removed. Thus, Pandey et. al. clarify a critical point: the IGS are the band edge states literally “relaxing” into the gap, therefore the orbital character of the valence and conduction band edges is crucial in understanding the IGS.

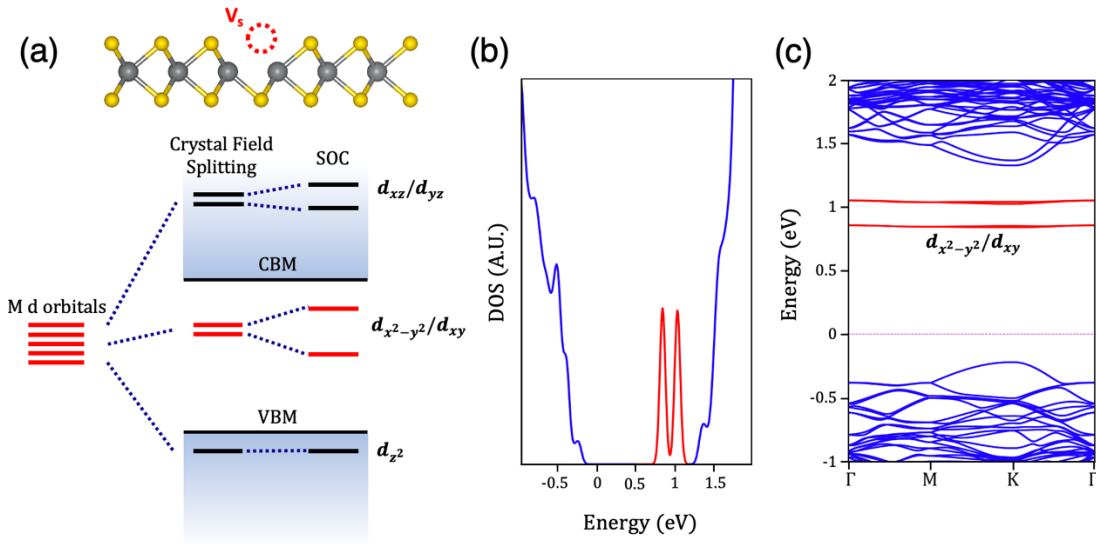


Figure 4.9 (a) A schematic showing a chalcogen top vacancy (top) and a schematic showing the origin of the resulting IGS (bottom). The lowest energy transition metal d orbitals relax into the gap, and then are split from spin-orbit coupling, resulting in two states. (b) A first principles DFT calculation of the DOS of a S vacancy in WS₂. (c) The corresponding DFT band structure calculation for a S vacancy in WS₂.

With knowledge of the conditions that lead to TMD IGS, we set out to understand the orbital contributions of the chalcogen vacancy IGS by applying the same procedure we used for the pristine TMD band structure. Using the schematic in Figure 4.9 (a) as a guide, crystal field splitting first lifts the degeneracy of the transition metal d orbitals as previously discussed. However, the missing sulfur atom causes the $d_{x^2-y^2}/d_{xy}$ at the conduction band edge to relax into the gap, while the filled d_{z^2} state remains in the valence band region. Next, if we include SOC, the $d_{x^2-y^2}/d_{xy}$ orbitals are split in energy, inducing two distinct defect resonances within the band gap. As previously noted, this is a simplified intuitive view of the situation, which leaves out the orbital hybridization. However, DFT calculations have shown that the main orbital contribution to these two IGS is indeed from

the $d_{x^2-y^2}/d_{xy}$ orbitals (with smaller contributions from other orbitals) [84, 91, 109], and our DFT calculations also reproduced these results (Figure 4.9 (b) and (c)).

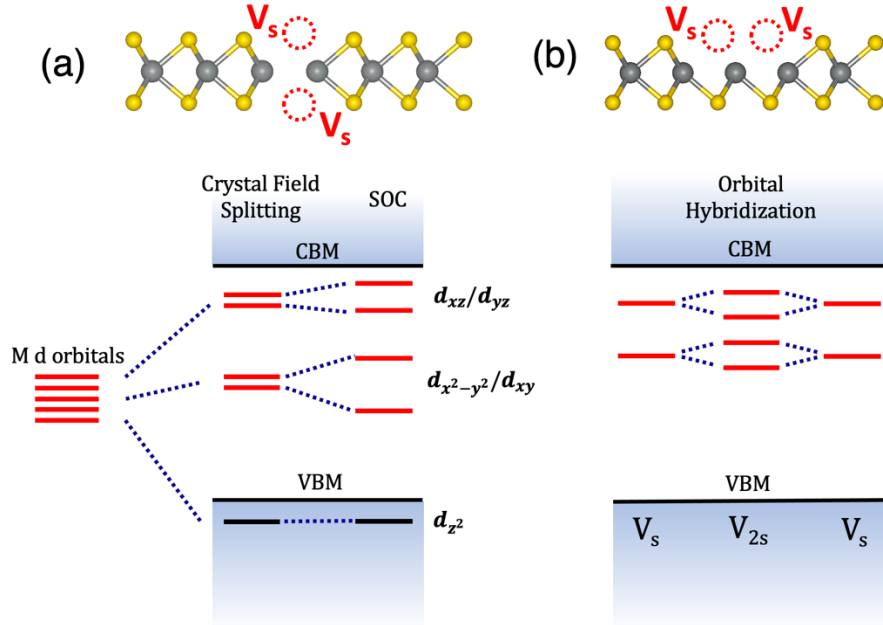


Figure 4.10 (a) A schematic showing a chalcogen column vacancy (top) and a schematic showing the origin of the resulting IGS (bottom). The divacancy reduces the electrostatic repulsion of the nearby chalcogen atoms, and the transition metal d orbitals relax into the gap, then split due to spin orbit coupling. (b) a schematic of a lateral S divacancy (top) and a schematic showing the hybridization of nearby overlapping defect orbitals will result in an increase in IGS state due to orbital bonding/antibonding.

The picture becomes more complicated when chalcogen vacancies are introduced at small separations, creating divacancies. In this case, the vacancies can no longer be considered isolated because the defect orbitals are close enough to interact. As discussed above, theoretical studies agree that the interaction of two nearby sulfur vacancies will cause an increase in the number of IGS, but the origin of these states differs depending on the divacancy orientation [87]. Applying the prior crystal field splitting approach, removal of a nearby sulfur atom will change the surrounding ligand field, which can result in higher

energy states relaxing into the band gap. In this case, the d_{xz}/d_{yz} states also fall into the gap at the conduction band edge, along with the $d_{x^2-y^2}/d_{xy}$ orbitals, which was theoretically predicted to occur for vertically aligned divacancies, or so called “column vacancies” (Fig. 4.10 (a)) [87, 91]. On the other hand, in cases where defect orbitals significantly overlap, the additional effect of orbital hybridization also comes into play. In this case, the dangling bonds of nearby vacancies with the same energy and orbital character will form bonding and antibonding levels, increasing the number of IGS (Fig. 4.10 (b)). This scenario has been theoretically predicted for neighboring lateral divacancies in TMDs [75, 87, 88]. In reality, the complex nature of orbital contributions of the IGS of different divacancy geometries will have some combination of these two effects, and therefore should be investigated on a case by case basis. Further, although this interpretation is helpful in understanding the origin of the states, it does not take into account the d and p orbital hybridization. As we show later, first principles calculations are a powerful tool to gain deeper insight into these complex defect-defect interactions.

4.5 WS₂ SULFUR VACANCY DEFECT-DEFECT INTERACTIONS

As discussed above, thermal annealing of the WS₂ generated a high concentration of sulfur vacancies, and an assortment of interesting atomic defects emerged. Figure 4.11 shows a zoom in are of the STM image in Figure 4.4, which gives a closer look at the rich complexity of the resulting collection of defects. Within this defect “zoo,” single sulfur vacancies (Figure 4.11 (1)) and oxygen passivated sulfur vacancies (Figure 4.11 (2)) were thoroughly characterized in two previous STM studies as discussed in section 4.3 [76, 109]. In our case, by pushing the limits of thermal treatment, we see the arrival of defect clusters. The simplest example of these aggregate defects has the appearance of nearby single sulfur vacancies (Figure 4.11 (3)), while the structure of more irregular clusters (Figure 4.11 (4))

is more of a challenge to unravel. Here, we use STM to explore this assortment of diverse multi-vacancy arrangements.

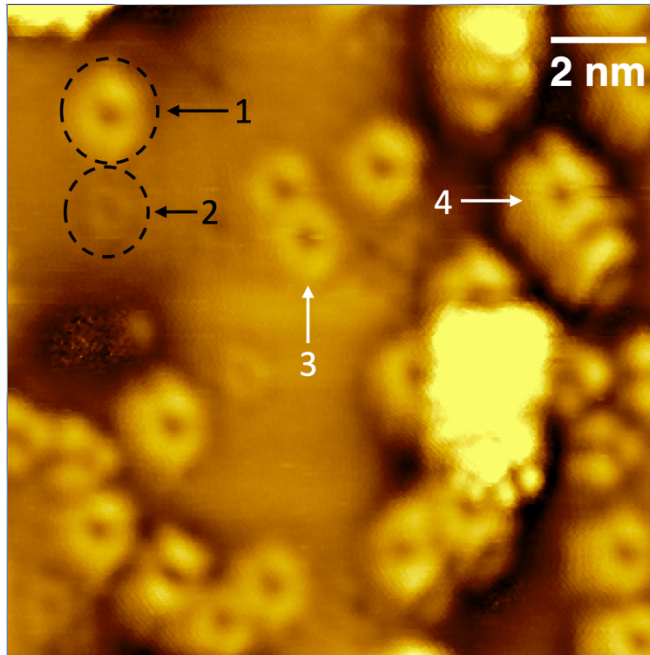


Figure 4.11 An STM image showing a variety of defects, including: (1) a S top vacancy, (2) an oxygen passivated top vacancy, (3) a lateral S divacancy, (4) an aggregate S vacancy complex, among others. Image acquired at a sample bias of 1.1 V.

4.5.1 Column Divacancy

A natural step in investigating the interactions of the sulfur vacancies was to verify that our experimental results for the single sulfur vacancy properties matched previous reports. As discussed above, the single sulfur vacancy characteristics were reproduced, but with an additional conundrum. In some cases, when a defect appeared to be a sulfur top vacancy, the electronic structure showed an increase in IGS. Figure 4.12 (a) shows one such defect, indicated by the blue circle, which has the same distinct trifold

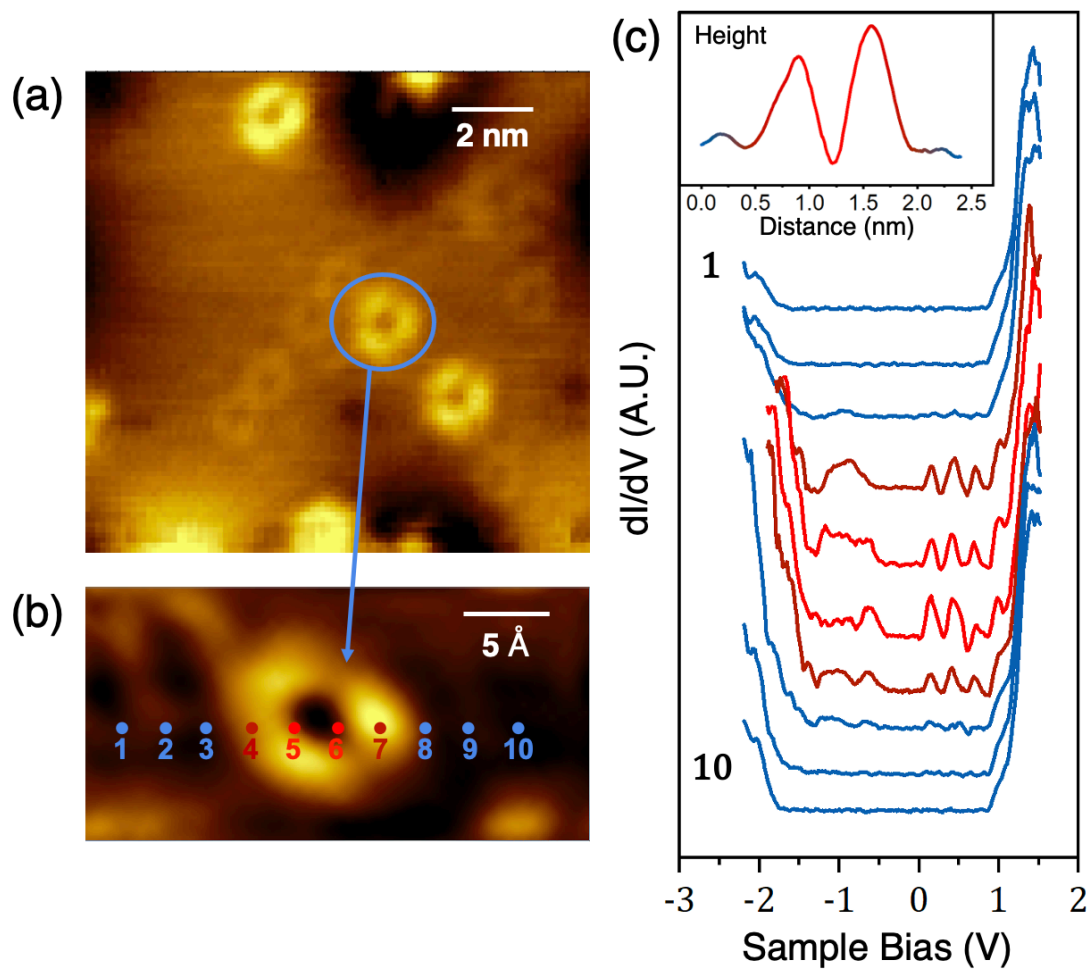


Figure 4.12 (a) Zoom of the STM image in Figure 4.3 (e), (b) Zoom in image of a point defect assumed to be a column vacancy (c) Inset is a height profile across the defect in (b), dI/dV spectroscopy corresponding the points in (b). On the defect (red) there are additional IGS. STM images obtained at a sample bias of 1.1 V.

lobe structure as the previously discussed sulfur top vacancy (Figure 4.4). However, STS dI/dV measurements taken on a line across the defect (Figure 4.12 (b)) show an intriguing increase in the number of IGS for spectra obtained above the defect (Figure 4.12 (c)). Specifically, rather than two defect resonances at the conduction band edge, there are four, in addition to wide band of states at the valence band edge (see 4.11 (c) red). As previously

discussed, the defect lobes shown by STM are a visualization of the localized IGS of the defect. A height profile in the inset in 4.11 (c) shows that the defect lobes span approximately 1.5 nm, which indicates that defect-defect interactions should occur when lateral defect separations are on this order. However, Figure 4.12 (a) clearly shows there are no sulfur vacancies close enough for hybridization, and the nearby oxygen passivated defects cannot cause hybridization because they have no IGS. Therefore, this increase of IGS is quite perplexing, but theoretical calculations can be a guide in unraveling this surprising development.

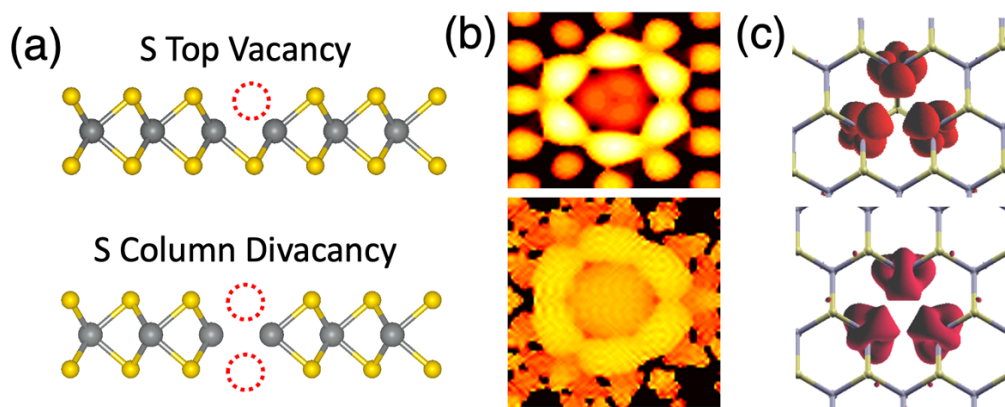


Figure 4.13 (a) Schematic showing S top vacancy (top) and column divacancy (bottom) in WS₂. (b) Simulated STM image of the S top (top) and column (bottom) vacancies. (c) Corresponding orbital density calculated by DFT showing the morphology of the top vacancy and column vacancy is nearly the same.

We performed DFT calculations (see Appendix E for details) to determine the atomic and electronic structure of an assortment of different defect geometries (discussed later), one of which was a sulfur divacancy comprised of vertically aligned sulfur vacancies shown schematically at the bottom of Figure 4.13 (a). We will adopt the terminology “column vacancy” here, which is commonly used to describe vertical chalcogen vacancies in TMDs. Figure 4.13 (b) shows a comparison of simulated STM images for a single top

vacancy (top) and column vacancy (bottom) calculated by DFT. The topography of these two defects is nearly identical, showing three lobes with trifold symmetry oriented along the same atomic lattice directions. Further, orbital density calculations show that the electronic states for both the top vacancy and the column vacancy are localized around the transition metal atoms nearest the missing sulfur atoms (Figure 4.13 (c)). This suggests that the geometric structure of the dangling bonds imaged by STM measurements will be indistinguishable for the sulfur top vacancies and column vacancies. However, a previous TEM study found that the formation of column vacancies in WS_2 was common, and further showed that column vacancies are more energetically favorable in WS_2 than isolated single vacancies or lateral divacancies [106]. These results suggest that at high sulfur vacancy concentrations in WS_2 , column vacancies will emerge, which supports our identification of this feature as a possible column vacancy.

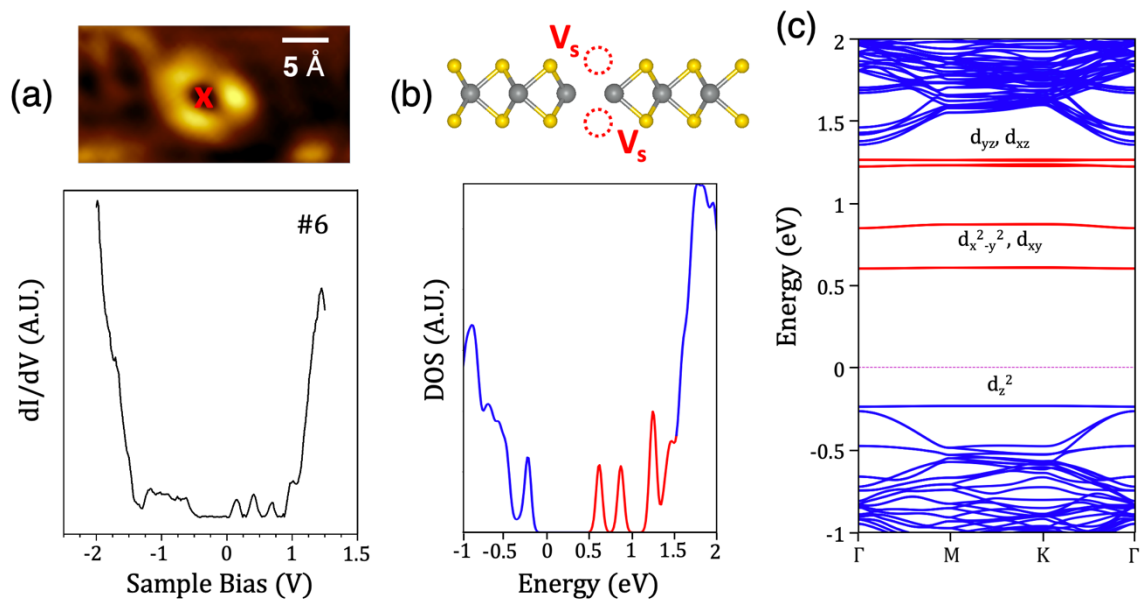


Figure 4.14 (a) STS dI/dV curve #5 from Figure 4.12, taken at the center of the column vacancy (red x). (b) DFT calculation of the DOS of the WS_2 column vacancy as indicated by the schematic above. (c) Corresponding DFT band calculation of the column vacancy.

Now that we have an understanding of the physical structure of the column vacancy, we further apply DFT to investigate the nature of the IGS. Figure 4.14 (a) shows one of the dI/dV spectra (taken at point 5 in 4.12 (b)) with four distinct IGS near the conduction band edge. Comparing with the DOS calculated by DFT, we see that the four in gap states match the corresponding experimental results nicely (Fig. 4.14 (b)). Figure 4.14 (c) shows the calculated band structure of the WS_2 with a column vacancy showing four IGS, along with a state at the very edge of the valence band. The orbital character of the IGS was obtained by projection onto the different atomic orbitals; in this case, like the single vacancy, the two lowest energy states are dominated by the $d_{x^2-y^2}/d_{xy}$ orbitals. However, we found that the main orbitals contributing to the two higher energy states were the d_{xz}/d_{yz} orbitals, indicating the relaxation of the orbitals deeper into the gap. A previous first principles study by Khan et. al. showed a similar result for column vacancies, although the d_{xz}/d_{yz} orbitals did not fall completely into the gap [91].

We next address the puzzling broad state present at the edge of the valence band. Theoretical predictions agree that the singlet state at the valence band edge is more delocalized because it is hybridized with the bulk valence continuum [83, 89, 91, 111]. High defect concentrations were predicted to lead to defect-defect interactions that will broaden the IGS from vacancies [98, 111]. Thus, one explanation for this broad band of states arises from the delocalized nature of the valence band edge state, due to hybridization. Theoretical predictions have further shown that this scenario would result in the valence band edge state being pulled deep into the band gap [98, 111]. We note that a similar broad feature was seen previously in an electron tunneling study of WS_2 , though the cause of the feature was not explained [88].

4.5.2 Lateral Divacancy

We next turn our attention to the case of two sulfur vacancies with a small lateral separation, close enough for the defect orbitals to overlap, leading to defect-defect interactions. Figure 4.15 (a) is an STM image showing a zoom in of the lateral divacancy defect (3) from Figure 4.11. As we clarified earlier, the sulfur vacancy is located at the dark center of the defect, while the bright lobes are centered about the neighboring tungsten atoms (Figure 4.5). With this in mind, we perform a height profile across the defect (Figure 4.15 (b)) to determine the separation of the vacancies, and find a distance of ~ 1.1 nm. Although the defects are separated by more than three lattice constants, the profile shows that the defect lobes are overlapping to such a degree that distinguishing where one vacancy ends and the other begins is impossible, as indicated by the red portion of the profile. To ascertain the defect orientation, recall that the defect lobes follow the zigzag atomic lattice direction, as do the dark spots of the oxygen passivated defects, indicated by the black dashed lines in Figure 4.15 (a). Using this knowledge as a rough guide, we can determine that the two vacancies are not in the same atomic lattice row, but rather separated with an orientation closer to the armchair direction (Figure 4.15 (c)). We note that although STM images are prone to drift, comparison with nearby defects with a known orientations in the same image is a reliable method as the drift will skew all of the defects equally. With a separation of ~ 1.1 nm, it is possible that the two vacancies are separated across two lattice sites in the armchair direction (Figure 4.15 (c) red), which would give a separation of 1.1 nm. However, we cannot rule out the possibility of a mixed armchair and zigzag separation, as the angle is close, and the distance is similar at 1.14 nm (Figure 4.15 (c) blue).

Following the same procedure applied to the column vacancy, we investigate the electronic structure of the lateral sulfur divacancy. STS dI/dV spectroscopy was

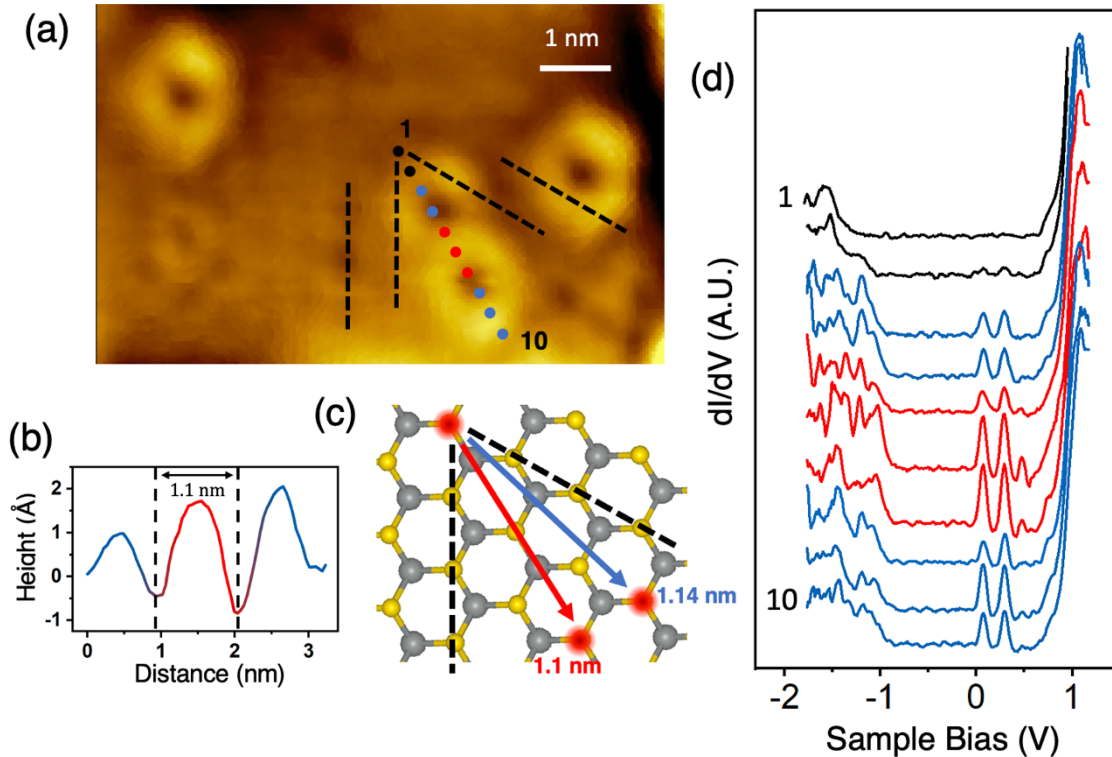


Figure 4.15 (a) STM image showing a zoom in from Figure 4.11. The black dotted lines correspond roughly to the zigzag direction of the WS₂ atomic lattice (b) a line profile taken diagonally across the lateral S divacancy (c) A schematic showing the WS₂ lattice. The blue and red arrows indicate two possible lattice site orientations of the two vacancies. (d) dI/dV spectroscopy taken on a line across the defect, indicated by the colored dots. Sample bias of (a) was 1.1 V.

performed in a line across the defect, as shown in Figure 4.15 (d). The first two spectra off of the defect (black) shows the WS₂ bandgap as the IGS start to emerge. On top of vacancies where the lobes are not overlapping, the DOS is similar to the spectra from isolated sulfur vacancies with two IGS at the conduction band edge (blue). However, the spectra taken on top of the shared defect lobe (red) show an additional IGS at a higher energy. This surprisingly affirms that even when defects have a separation greater than three atomic lattice constants, they are still close enough to weakly interact, increasing the number of IGS. Strong hybridization was previously reported for two chromium atoms

substituting tungsten in WS₂ with a separation of two lattice sites apart in the zigzag direction (~ 0.6 nm) [74], therefore it is reasonable that weak interactions might occur at larger separations. Later, we will discuss our DFT analysis to further explain this interaction.

4.5.3 Vacancy Aggregate

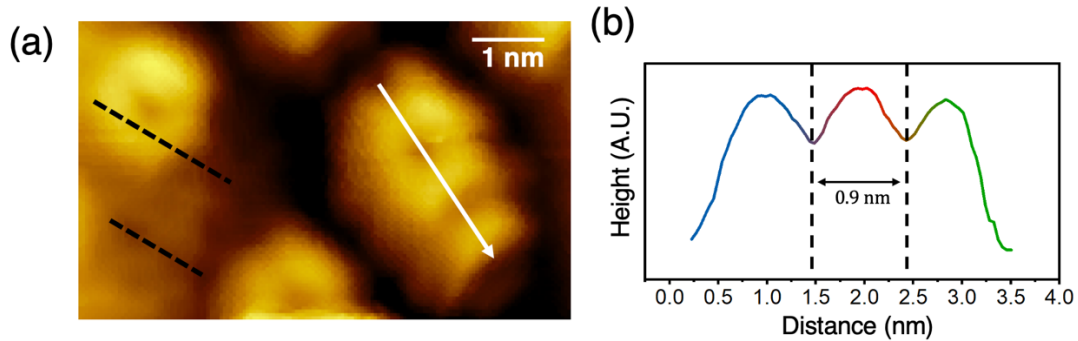


Figure 4.16 (a) Zoom in of the aggregate vacancy defect (4) from Figure 4.11. The black lines roughly indicate the zigzag direction (b) A height profile of the aggregate defect. Sample bias of STM image (a) was 1.1 V.

We next address the complex amorphous defect (4) shown in Figure 4.11. Unlike the previous defects we have discussed, the atomic structure of this defect was not simple to pin down due to the strong increase in localized states. The increase in STM contrast and unclear globular structure suggests that this defect is some aggregate cluster of sulfur vacancies. Figure 4.16 (a) gives a closer look at the structure and orientation of this aggregate defect. Comparing the orientation with the S top vacancy to the left, it seems that the aggregate defect is not oriented along the zigzag direction. A line cut across the defect (Fig. 4.16 (b)) shows that the dips between defect lobes are spaced approximately 0.9 nm apart. As we previously discussed, the dark center of the vacancies denotes the location of the missing S atoms, but in this case, it is difficult to make this assumption. The

dramatic increase in the in the LDOS is an indication that this defect includes vacancies with significant orbital overlap, however, a spacing of 0.9 nm is more than two atomic lattice constants. Further, a TEM study on WSe₂ have showed that vacancy clusters can result in chalcogen-transition metal bond rotation, leading to a rearrangement of the atomic structure near the defect. Thus, we are hesitant to assign a specific structure to this defect, as we cannot rule out such a lattice transformation, and STM topography alone is not a reliable indicator.

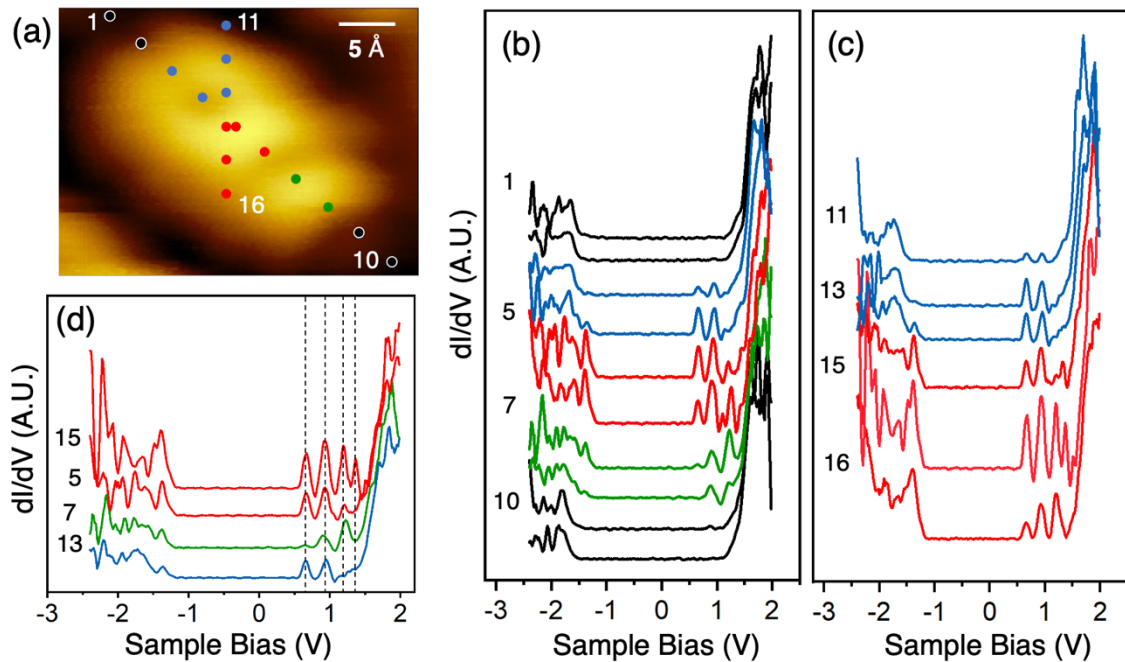


Figure 4.17 (a) STM image of the aggregate defect, with the points showing the location of dI/dV spectroscopy taken along diagonal (1-10) and vertical (11-16) lines. (b) Plot of the spectra 1-10 showing that the IGS change at the different orbital locations on the defect (c) Plot of dI/dV spectra 11-16 (d) Comparison of select spectra from different areas of the defect. Sample bias of STM image (a) was 1.1 V.

We next turn our attention to the electronic structure of the aggregate defect. We performed dI/dV spectroscopy across the defect along two lines, one following the defect

axis (spectra 1-10), and one vertically across the defect (spectra 11-16). Similar to the case of the lateral divacancy, we see that the defect electronic structure evolves across the defect (Figure 4.17 (b), (c)). In particular, at the middle of the defect we see the greatest increase in IGS, where there is the most apparent overlap of the orbital lobes (red). However, Figure 4.17 (b) shows an important divergence from the behavior of the lateral divacancy; the electronic structure differs at the left and right hand sides of the defect (Fig. 4.17 blue, green). This implies that the atomic structure is not symmetric across the defect, which is supported by the increase in “brightness” or contrast at the left hand side of the defect. Figure 4.17 (d) gives a comparison of the IGS at the different locations on the defect, and the black dotted lines guide the eye to the different peak positions of the defect resonances. Upon this comparison, it is evident that both the left and right hand sides show two peaks at the conduction band edge, but at higher (right, green) and lower (left, blue) energies, with one of the peaks overlapping. At the middle of the defect with the greatest orbital overlap, we see four distinct states emerge at the conduction band edge. We note that there is also a resonance at the valence band edge across the entire defect. This behavior makes sense, as the valence band edge states tend to be more delocalized, while the conduction band edge states depend heavily on the orbital geometry and amount of overlap of the defect lobes, as discussed above.

Although it is difficult to disentangle the complex geometry and electronic structure of this aggregate defect, we can gain some qualitative insight by analyzing its properties. First, we note that other intrinsic defects such as the aforementioned chromium substituting tungsten have been observed in WS_2 [74], which introduces the possibility that this defect is not solely comprised of S vacancies. However, the chromium defect geometry does not match, and it introduces IGS that are not well defined like the resonances shown here, therefore we are confident that this aggregate defect is a sulfur vacancy complex. Next,

compared to the more defined structure of the lateral divacancy, the amorphous structure of the aggregate defect hints that the sulfur vacancies are closer together. Thus, a comparison of the lateral divacancy and the aggregate defect illustrates the overall trend that vacancies with smaller separations have increased defect-defect interactions, leading to an increase of IGS due to hybridization and changes in the crystal field splitting. Later, we will utilize first principles calculations to gain more detailed insight into this overarching trend.

4.5.4 Line Defect

One of the most surprising features we found as a result of the heavy thermal annealing were bright lines crisscrossing the WS_2 surface, as was previously depicted in Figure 4.3 (e). Taking a closer look at one of the lines from Figure 4.3 (e) (Figure 4.18 (a)), we see that the line defect has a brighter contrast than the surrounding point sulfur vacancies. This STM image was taken with a bias setpoint of 1.1 V at the CBM edge, and recall that this bias probes primarily the unfilled IGS. Therefore, this increase in contrast at 1.1 V already indicates that the line defect introduces an increase in IGS. Figure 4.18 (b) shows an STM image of another line defect at 3 V, which surprisingly shows a more clearly resolved image of the structure. We attribute this behavior to the tip picking up debris that helped probe the surface, as the STM contrast of the WS_2 is usually quite different at 3 V. From this image we can conclude that the line defect follows the zigzag direction (blue line), by using a nearby S vacancy as a guide. We also see a peculiar lobed structure at the left end of the defect, which hints that the line defect is comprised of an aggregate line of S vacancies. The line defect interestingly shows an asymmetric

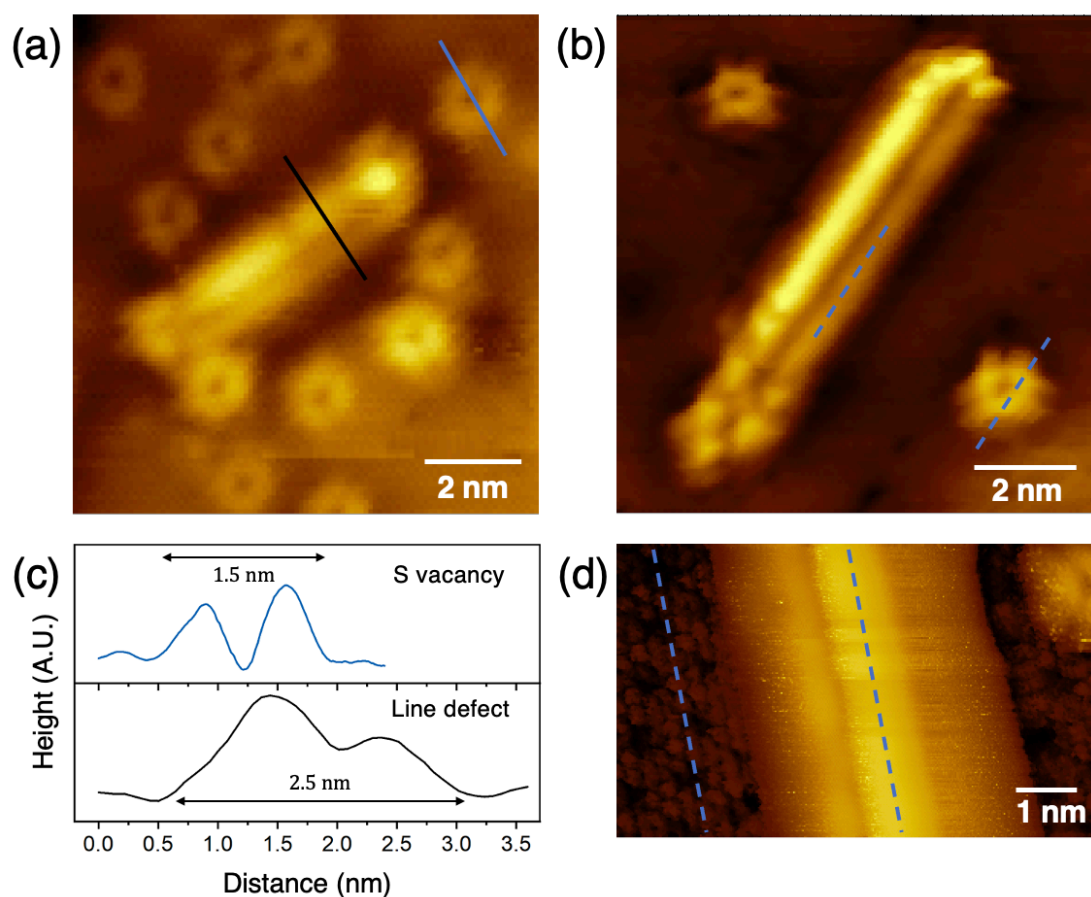


Figure 4.18 (a) Zoom in of the STM image in 4.3 (e) showing a line defect obtained at 1.1 V sample bias. (b) Higher resolution image of a line defect obtained at 3 V sample bias. The blue lines indicate that the line follows the zigzag direction of the atomic lattice. (c) Line profiles taken across the line defect (black) and S vacancy (blue) in (a). (d) Atomic resolution STM image showing the line defect follows the zigzag direction (blue line) obtained at -1.5 V sample bias.

contrast, which is revealed by the line profile in 4.17 (c) (bottom). A comparison with of a profile of a nearby point vacancy shows that the lateral dimension of the line is much larger, at ~ 2.5 nm. However, it is difficult to conclude whether the localized states extend farther, or if the line results in a reconstruction of the nearby atomic structure, leading to a larger geometry. Figure 4.18 (d) shows a line defect imaged at -1.5 V sample bias, which shows the atomically resolved lattice next to the defect. From this image we can conclude

with more certainty that the line defect indeed follows the zigzag direction, but the increased LDOS at the defect make it impossible to resolve the atomic structure.

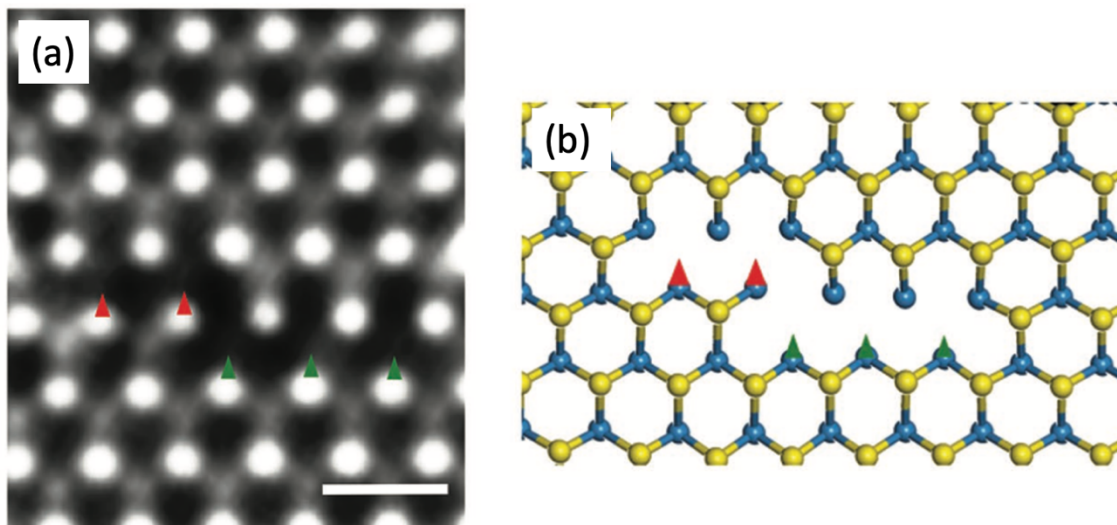


Figure 4.19 (a) a TEM image showing a WS_2 line defect composed of S column vacancies (b) a corresponding schematic showing the WS_2 atomic structure, with S (yellow) and W (blue) taken from Ref. [106]

Although we cannot make any concrete conclusions about the precise structure of this line defect based on STM characterization alone, we can fortunately look to a prior TEM study for guidance. Zhao et. al. found that after electron irradiation, WS_2 formed so called “chain vacancies” comprised of lines of S column vacancies, as shown by the TEM image in Figure 4.19 (a) [106]. The chain vacancies form a line along the zigzag direction, and the structure is inherently asymmetric on either side as shown by the schematic in Figure 4.19 (b). On one side of the line defect the W atoms have two adjacent column vacancies, while on the other side each W atom is adjacent to only one. This asymmetry is possibly the root cause of the peculiar change in contrast across the line (Fig. 4.18), as there would be more dangling bonds on one side of the line than the other. Zhao et. al. further

performed a theoretical calculation, and found that column vacancies are more energetically favorable than two isolated vacancies, and that chain vacancies in the zigzag direction were also energetically favorable, explaining their common occurrence in TEM measurements [106]. However, the reported chain vacancies were only three lattice sites long, while the line defects reported here are longer than 5 nm (> 10 lattice sites). Therefore, we cannot rule out the possibility that at high defect densities there might be reconstructions of the atomic lattice geometry, rather than a simple chain of column vacancies.

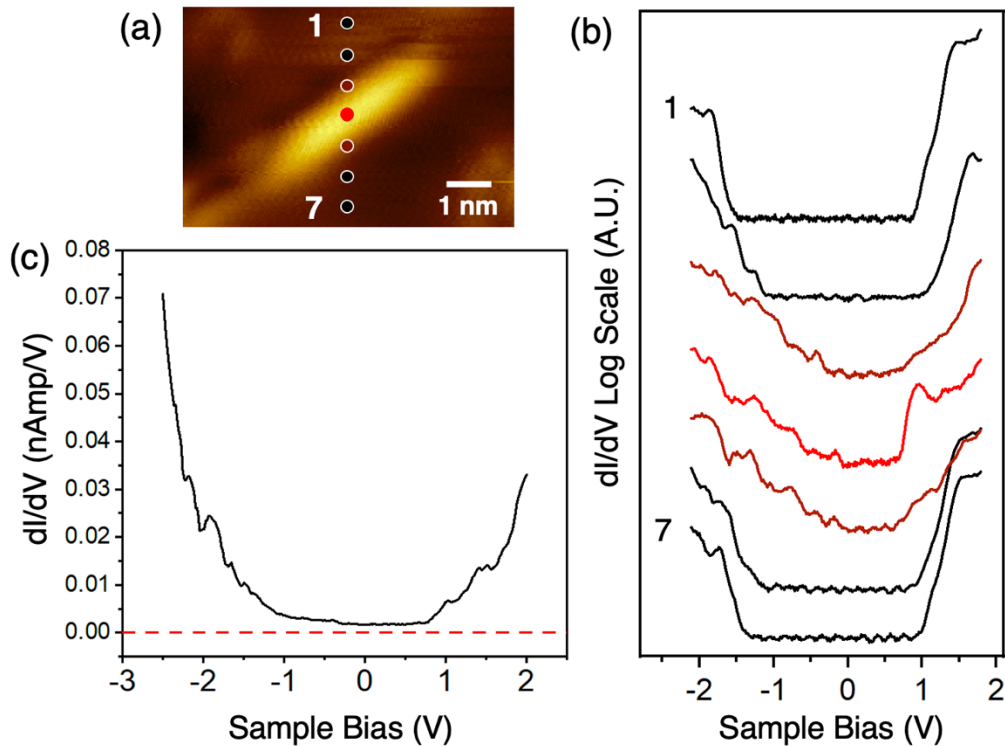


Figure 4.20 (a) STM image of a line defect taken at -2.5 V (b) dI/dV spectra taken at the locations indicated by the dots in (a), plotted in logarithmic scale. There is a strong increase in IGS one the line. (c) Plot of averaged dI/dV from line defects in linear scale, showing that the defect is metallic with finite conductivity near the Fermi level (red line).

We next examine the electronic structure of the line defect, again performing dI/dV spectroscopy along a line across the defect (Figure 4.20 (a)). From Figure 4.20 (b), plotted in logarithmic scale for clarity, we observe that at the line, states fill a continuous band at both the valence band and conduction band edges. Near the Fermi level, a small gap seems to remain, but a closer look at the electronic structure of the line defect in linear scale shows otherwise. Figure 4.20 (c) clarifies that the DOS never quite goes to zero (indicated by the red line) elucidating that the line defect has a metallic character. This behavior is not that surprising, as it is well known that defects such as grain boundaries have a metallic character [132], and chalcogen vacancy line defects were theoretically predicted to induce a dramatic increase in IGS [108].

4.6 FIRST PRINCIPLES CALCULATIONS OF DEFECT-DEFECT INTERACTION

In order to obtain an understanding of the characteristics of the S vacancy defect-defect interactions, we performed first principles calculations. Using density functional theory (DFT), we calculated the DOS and band structure, and simulated STM images to compare with the experimentally observed defect geometries we discussed above (see Appendix E for methods). We sought not only to interpret our experimental results, but also to gain insight into the general behavior of the defect-defect interactions by systematically changing the orientation and distance.

We first investigate the electronic structure of S vacancies along the zigzag direction $\langle \bar{2}11 \rangle$ with different separations as indicated by Figure 2.21 (a). Specifically, Figures 2.21 (b), (c), (d) show the calculated electronic structure of vacancies at adjacent (1), next nearest (2), and third nearest (3) lattice sites in the zigzag direction, respectively. Comparing the resulting DOS and band structures of these three zigzag configurations side by side, the evolution of the IGS as a function of distance becomes clear. For the smallest

separation (Fig. 2.21 (b), case 1), the IGS have the greatest spread, and as the defects get farther apart (Fig. 2.21(c), case 2) the states get closer together, finally appearing nearly the same as an isolated S vacancy (Fig. 2.21 (d), case 3)

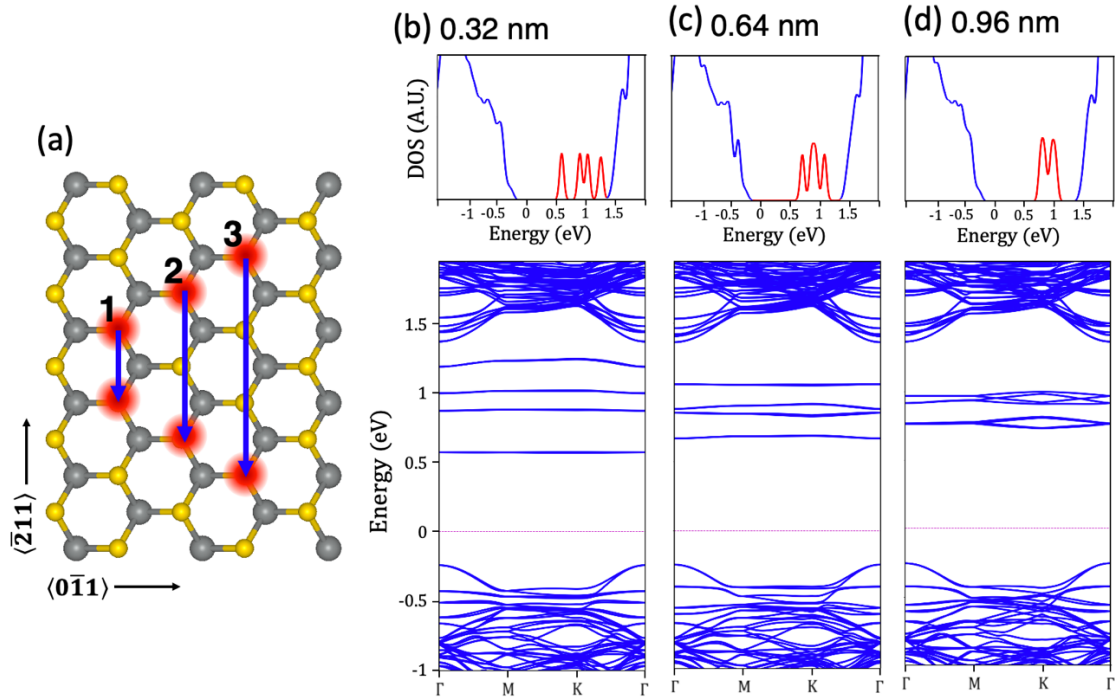


Figure 4.21 (a) A schematic showing the atomic location of three cases of calculated S vacancies along the zigzag direction with increasing separation. (b), (c), (d) Calculated DOS and band structure for two S vacancies separated by one, two, and three lattice constants, respectively.

Next, we consider the interactions along the armchair direction $\langle 0\bar{1}1 \rangle$, and mixed armchair and zigzag direction (shown schematically in Fig. 2.22 (a)). Figure 2.22 (b) shows the electronic structure corresponding to S vacancies located at nearest lattice sites following the armchair direction (case 4); note that although the defects are closer together than the case of two vacancies separated by two lattice sites in the zigzag direction (Fig. 2.21 (c), case 2), the IGS seem to be less spread out. This indicates that vacancies along the same lattice row in the zigzag direction interact more strongly, which

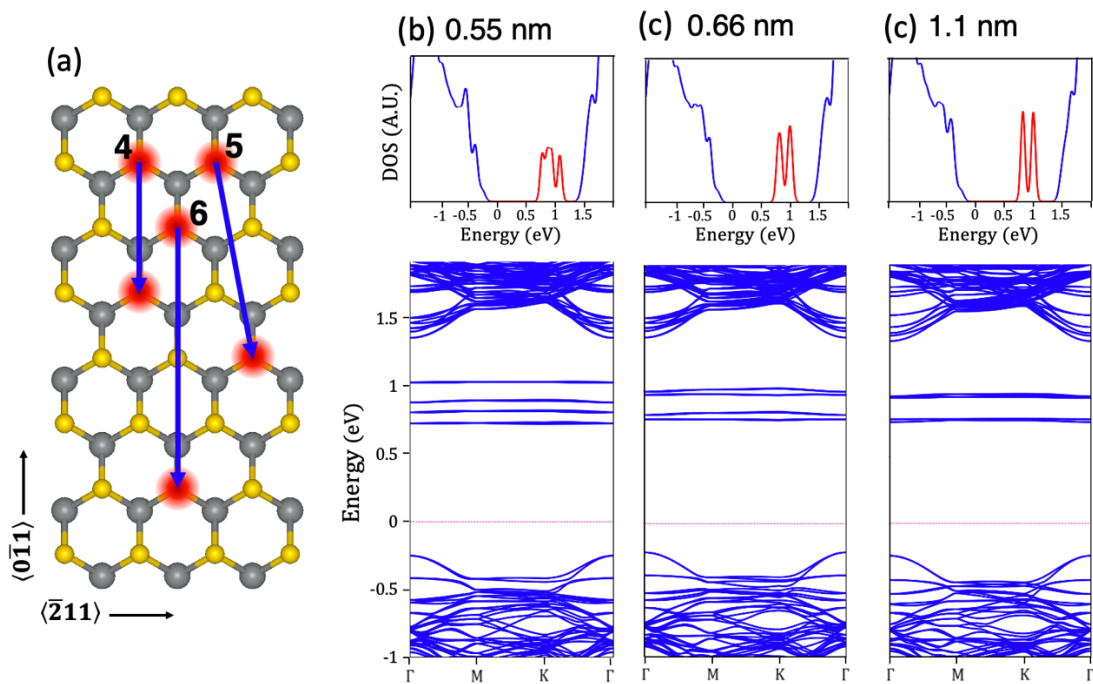


Figure 4.22 (a) A schematic showing the three cases of calculated two S vacancies separated along the armchair direction (case 4, 6) and mixed armchair and zigzag direction (case 5) with increasing separation. (b), (c) Calculated DOS and band structure for two S vacancies separated by one and two armchair lattice sites, and (c) a mixed armchair and zigzag separation

makes intuitive sense as the defect orbitals are oriented along this direction and should have more overlap. Similarly, comparing the case of mixed zigzag and armchair orientation (Fig. 2.22 (c), case 5) with the zigzag direction vacancies separated by three lattice constants (Fig. 2.21 (d), case 3), we notice that the strength of the interaction seems comparable, even though the vacancies of the latter case are much further apart. Finally, we observe that the DOS and band structure calculation for S vacancies at a farther distance along the armchair direction (Fig. 2.2 (c), case 6) appears almost identical to an isolated S vacancy, suggesting that this distance is too large for defect-defect interactions to occur.

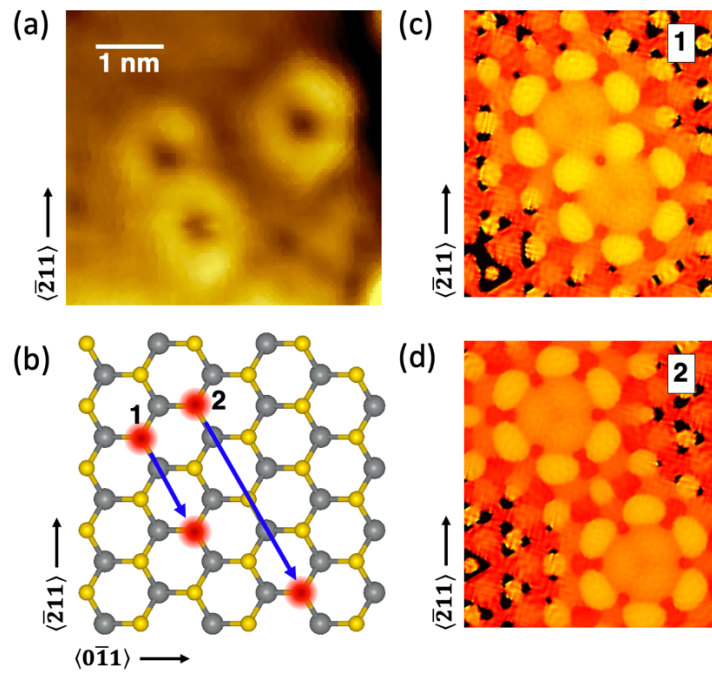


Figure 4.23 (a) STM image of the lateral S divacancy from Fig. 4.15 (a). (b) A schematic showing two top vacancies nearest (case 1) and next nearest (case 2) in the armchair direction. (c), (d) Simulated STM images for cases 1 and 2, respectively

The above results are consistent with our previous discussion, showing that there are two key elements determining the strength of defect-defect interaction, namely, the vacancy orientation and distance. However, upon making a detailed comparison of the calculated electronic structure with the experimental results, we find some interesting discrepancies. As previously discussed, the separation of the lateral divacancy is approximately 1.1 nm (Fig. 4.15), however, the DFT results predict that this separation is too large for the defects to interact (Fig. 4.22 (c)). Recall that the lateral divacancy appears to follow the armchair direction, therefore we compare it with STM simulations of S vacancies oriented along the armchair direction (Fig. 4.23). The STM image (Fig. 4.23 (a)) shows that the defect lobes overlap to such a degree that it is difficult to determine where

one vacancy ends and the other begins. The STM simulations show a similar geometry for nearby vacancies in the armchair direction (Fig. 4.23 (c), case 1), but this distance would be ~ 0.55 nm, which doesn't match our observations. A divacancy separated by two lattice sites in the armchair direction gives a similar separation of ~ 1.1 nm, but the STM simulation shows that the defects appear distinct without much overlap (Fig. 4.23 (d), case 2). Finally, a comparison of the DOS calculations (Fig. 4.22) with the STM dI/dV (4.15 (d)), we see that the case of nearby vacancies in the armchair direction (Fig. 2.22 (b), case 4) most closely matches, but this separation is too small, as noted above. Thus, the DFT calculations predict weaker interactions than the experimental STM observations indicate.

We next turn our attention to the case of the aggregate defect (Fig. 4.17), whose structure is unclear. The brighter left hand side shares a similar geometry with a top vacancy or a column vacancy, while the right hand side is unclear. We found that STM simulations of neighboring top and bottom vacancies in the zigzag direction showed the most similarities with our observed STM geometry. Figure 4.24 (a) is a schematic showing the two cases we simulated, nearest neighbor (case 1), and next nearest neighbor (case 2) top and bottom vacancies in the zigzag direction. Similar to the lateral divacancy, the closer vacancy configuration (Fig. 4.24 (b)) seems to be a better match for the electronic structure than the next nearest neighbor (Fig. 4.24 (c)). Further, recall that the distance between the dips in the topography of this defect were ~ 0.9 nm (4.16 (b)), which again indicates a larger separation. However, it is difficult to determine the location of the missing atoms, and we cannot rule out the possibility of a column vacancy next to a single vacancy. If one examines the amorphous structure at the end of the line defect (Fig. 4.18 (b)), presumably some form of S column vacancy, it becomes clear that this amorphous defect could be the beginning of a line defect. Therefore, it is difficult to assign the structure of this defect, even with the aid of DFT STM simulations.

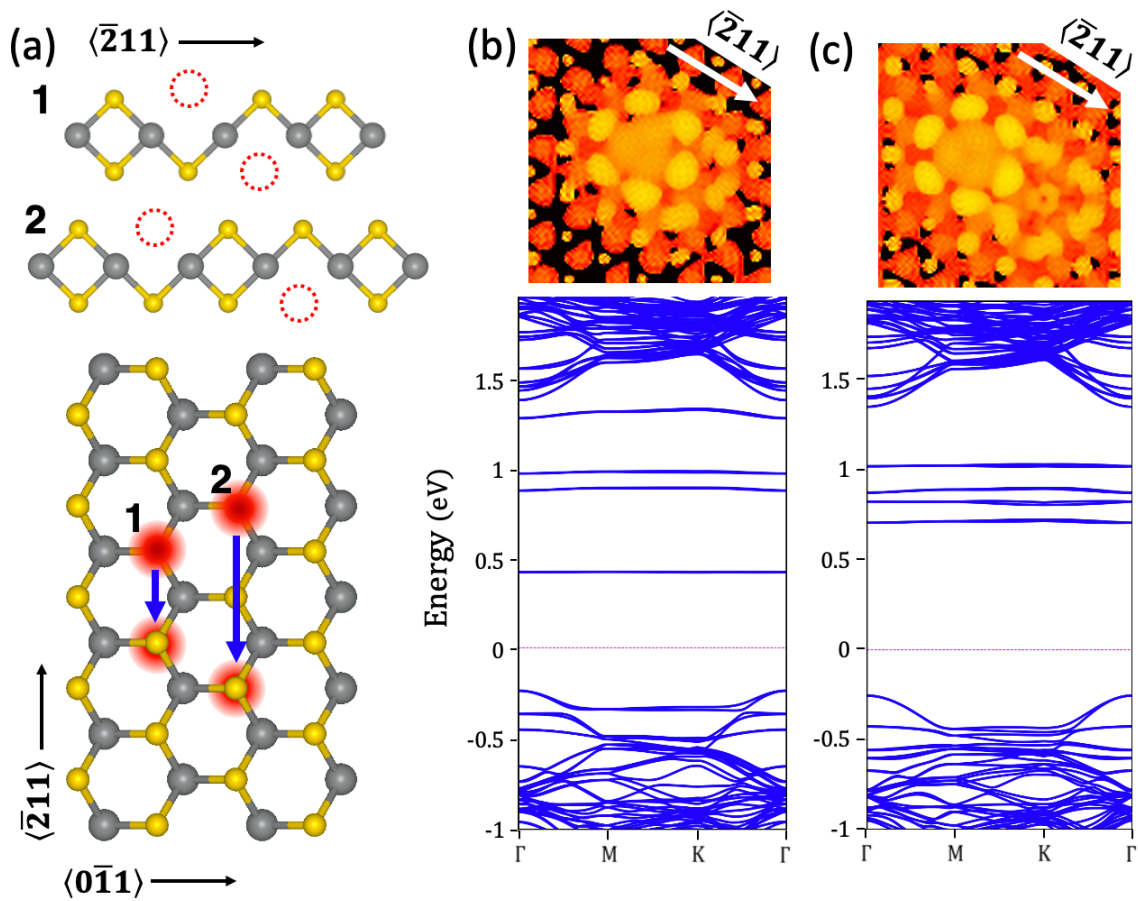


Figure 4.24 (a) A schematic showing lateral top and bottom S vacancies separated by one (case 1) and two (case 2) lattice constants. (b), (c) Corresponding simulated STM images and band structure calculations for cases 1 and 2, respectively.

Although it is difficult to assign the detailed structure of the aggregate defect, we can study the DOS of the similar staggered top and bottom vacancy defect (4.24 (a) case 1) to gain a better understanding of the aggregate defect electronic properties. Figure 4.25 (a) shows the DFT calculation of the DOS, showing four IGS at the conduction band edge, as well as an additional state at the valence band edge, similar to the aggregate defect (4.17). We also theoretically determine the orbital contribution of each state, finding the position where they are localized across the defect. As we observed previously with the

dI/dV measurements taken at different points across the defect, the different states are localized to specific sites across the defect, as indicated by the colored circles in the schematic in Figure 4.25 (b). Further, we see that the valence band edge state is more delocalized, appearing across the entire defect. Thus, although we cannot definitively determine the structure of the aggregate defect, we find that the overall electronic behavior is predicted by DFT.

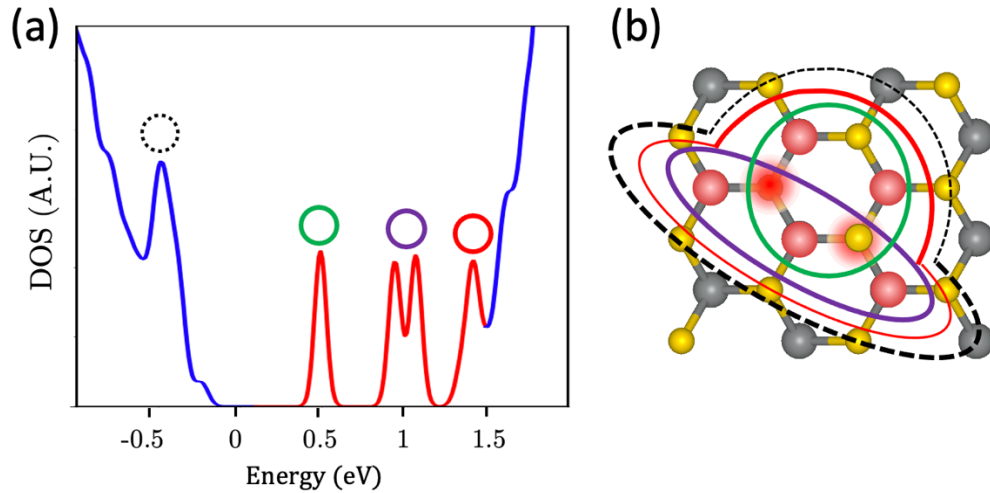


Figure 4.25 DOS calculation for a lateral top and bottom divacancy separated by one lattice constant (case 1 in Fig. 4.25) showing four IGS at the conduction band edge and one state at the valence band edge. (b) A schematic showing the localization of the states in (a) indicated by the colored circles.

4.7 CONCLUSION

In this study, we have brought to light several important aspects of TMD defect engineering using STM characterization and DFT calculations. First, we have demonstrated that thermal annealing is a viable and controllable method to deliberately introduce vacancies into TMD monolayers. We found that at high vacancy concentrations aggregate defects will form, directly showing that it is energetically favorable for vacancies to cluster. Further, we demonstrate that S vacancy defect-defect interactions result in a rich

variety of IGS beyond the two IGS previously reported for isolated S vacancies. Through a detailed investigation of a variety of aggregate S vacancies including divacancies and vacancy clusters, we learn vacancies interact even at separations greater than two lattice constants. We further show that the strength of the interaction, and therefore number of states introduced into the gap, depends on both vacancy separation and lattice direction, which we verified with DFT. Finally, we note that these overall trends not only apply to WS₂, but are likely generalizable to other TMD materials systems. Specifically, we predict that chalcogen vacancy defect-defect interactions will depend on separation and orientation, and that aggregate vacancy clusters will also form at high vacancy concentrations. Therefore, this study furthers the knowledge that can be applied to future defect engineering, showing that thermal annealing is a robust method for manipulating the electronic properties of 2D TMD materials.

Chapter 5

Tailoring the Lateral Potential Landscape of 2D Electronic Materials at the Nanoscale via Environmental Proximity Engineering

5.1 INTRODUCTION

As technology has advanced, the rush to miniaturization has led to the ultimate limit of atomically thin, two dimensional (2D) materials. Within the family of 2D layered van der Waals (vdW) materials, atomically thin semiconducting transition metal dichalcogenides (TMDs) have captured intense research interest, partly due to their potential for filling the semiconductor role in nanoscale electronics [5-7]. Semiconductor p-n junctions are the foundational element of most electronic devices, thus an important step in the design of 2D devices is the ability to create 2D analogues of the bulk p-n junction with controllable electronic properties. Following the example of heterojunction (HJ) design in three dimensional semiconductor counterparts, one approach is to combine two TMDs with different electronic properties to create a HJ. As 2D TMD monolayers interact weakly via vdW forces and can be easily isolated, fabricating vertical HJs by stacking different TMD monolayers has received intense investigation [2, 133-136]. However, these 2D stacked heterojunctions have a fundamentally different character than bulk p-n junctions, with no vertical depletion region due to low dimensionality, and an electronic structure that depends on interlayer coupling and stacking orientation rather than intrinsic band alignment alone [133, 137].

Another much less explored path is the synthesis of a planar, atomically thin, HJ comprised of two different TMD monolayers that are stitched together laterally [62, 138-140]. Recently, a lateral TMD heterojunction was realized using this method and intriguingly demonstrated a narrow, nanometer-scale, smooth hetero interface with type-II

band alignment [138]. This exciting result poses the intriguing promise of a nanoscale 1D analogue to bulk heterojunctions; however, the band offsets of HJs formed by this method is limited to hundreds of meV, constrained by the electronic properties available in the existing 2D TMD materials library [141]. The ability to engineer the electronic bandgap is crucial to HJ design, but TMDs are not limited to the toolbox of techniques conventionally used for bulk materials, as their extreme 2D nature provides other avenues to manipulate the electronic properties.

The atomically thin nature of 2D materials results in intimate contact of the entire layer with the surrounding environment. In consequence, the electronic band structure 2D materials is not a static property intrinsic to the material, and is strongly influenced by the surrounding environment. The interaction between a TMD and the nearby environment is complex, with a variety of effects modifying the electronic structure including (but not limited to) interlayer coupling [9, 10], substrate hybridization [142-144], substrate work function [66, 145, 146], and dielectric screening [120, 121, 147, 148]. Thus, if a TMD is embedded in an environment with lateral spatial inhomogeneity, changes in band alignment can occur within a single homogeneous monolayer, effectively creating a lateral HJ. Indeed, this environmental sensitivity was shown to result in a lateral modulation of the TMD electronic structure across the moiré pattern due to the local variation in interlayer coupling [137], changes in the electrostatic potential [66], as well as dielectric screening [149]. These results hint that through deliberate control of the surrounding environment, one can exploit this environmental susceptibility to non-invasively engineer a lateral HJ comprised of a single homogeneous TMD monolayer.

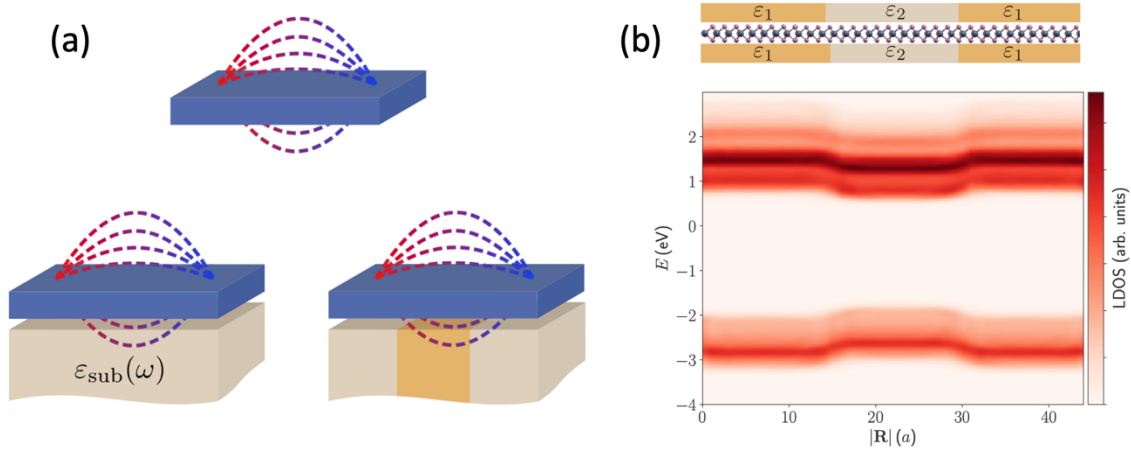


Figure 5.1 (a) Schematic showing the electric field of charges in a 2D TMD layer extends far outside the layer into the environment. The dielectric environment of the substrate results in screening of the overlying 2D layer. (b) A theoretical prediction showing a substrate with segments with different dielectric constants can modulate the bandgap of the overlying TMD layer, creating a heterojunction. Images taken from Ref. [150].

Dramatic band gap renormalization occurs in TMDs due to external dielectric screening from the substrate or capping layers because the electric fields from charges extend far outside the atomically thin layer [120, 151, 152] (Fig. 5.1 (a)). Theorists predicted that this effect could be harnessed to externally induce lateral bandgap modulations in monolayer TMDs at the nanometer scale by embedding them in spatially inhomogeneous dielectric environments (see Fig. 5.1 (b)). Thus, by placing a TMD on a substrate with segments that have different dielectric constants, a lateral HJ can be created by “coulomb engineering” [150, 153, 154]. Experimental studies later verified this phenomenon by placing monolayer TMDs on substrates with an abrupt change in dielectric constant, showing that a band gap modulation of a hundred of meV was achieved, although they did not demonstrate that this change occurs over a nanometer length scale [155-157]. Similarly, as TMD crystals are completely exposed at the surface, they are extremely

sensitive to surface adsorbates, which strongly tune the fermi level position and work function [158-160]. One study exploited this susceptibility to engineer a nanoscale lateral heterojunction by depositing a molecular acceptor layer on top of a monolayer TMD to effectively modulate the band structure [160]. Although these examples illustrate that environmental engineering is a promising path to design lateral heterojunctions within a single homogenous TMD monolayer, further exploration is necessary to unravel the underlying mechanisms of the surrounding environment influencing TMD overlayers.

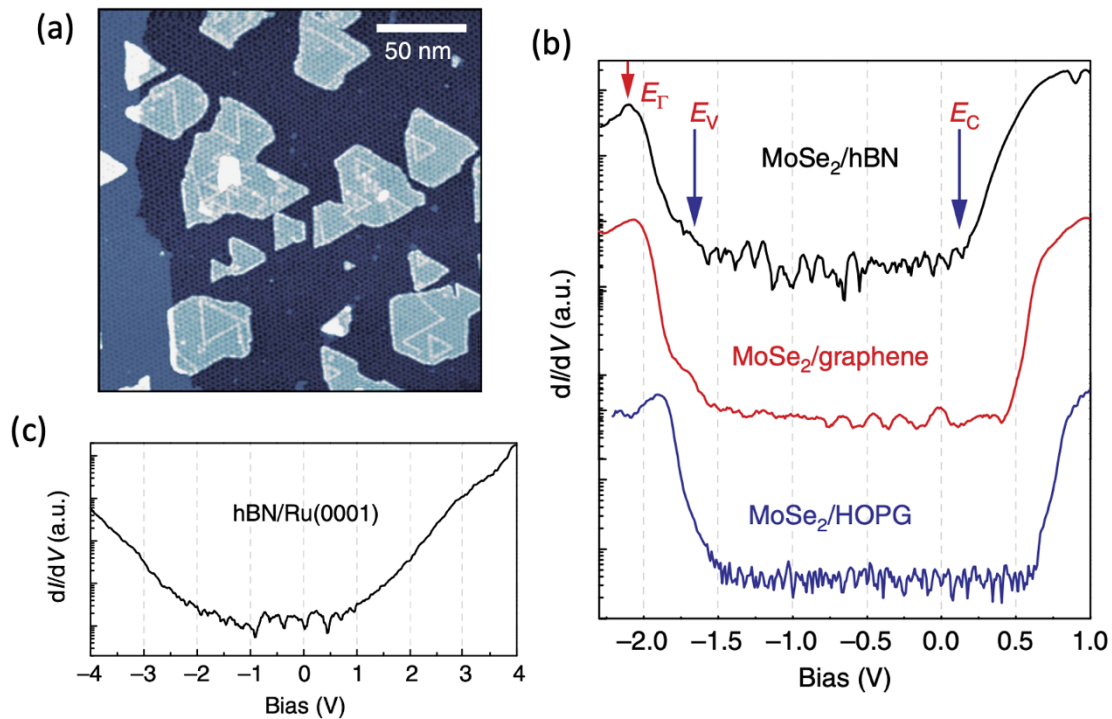


Figure 5.2 (a) STM topographic image showing MoSe₂ on a hBN/Ru substrate (b) dI/dV spectroscopy on the hBN/Ru surface showing metallic characteristics of the hBN layer (c) Comparison of dI/dV spectroscopy of MoSe₂ on hBN/Ru (black), graphene (red), HOPG (blue) showing that the MoSe₂ bandgap differs due to the change in electrostatic screening of the substrate. Images taken from Ref. [66].

In a similar vein, with a clever choice of substrate, one might expect that the dielectric screening of monolayer TMDs could be reduced, resulting in a larger band gap that is closer to the “intrinsic” value. With this in mind, a study by Zhang et. al. set out to directly synthesize MoSe₂ on a substrate of monolayer hBN grown on a Ru(0001) single crystal, as shown by the STM image in Figure 5.2 (a) [66]. Although hBN is normally a wide bandgap insulator that should provide isolation from screening, they surprisingly found that the MoSe₂ band gap was actually *smaller* than that of MoSe₂ synthesized on semi metallic HOPG substrates (see Fig. 5.2 (b)). This phenomenon was explained by further STS measurements on the hBN/Ru(0001) substrate, which interestingly showed that there was finite conductance within the expected gap region of hBN (Fig. 5.2 (c)). The strong interaction between the hBN and Ru causes metallic characteristics to emerge in the hBN, resulting in a strong screening effect that decreases the band gap of the overlying MoSe₂. Furthermore, studies have shown that the interaction of hBN on transition metal substrates changes with the local atomic registry across the moiré pattern, creating a so called “nanomesh” with strongly interacting “hole” regions and weakly interacting “wire” regions, as shown in Figure 5.3 (a) [65, 67, 68, 161, 162]. This interaction not only induces a structural corrugation in the hBN layer, but also introduces a non-uniform electrostatic field from charge transfer at the hole regions, causing a lateral periodic modulation of the work function (WF) (Figure 5.3 (b), (c)) [65, 67, 68, 163]. In the case of the MoSe₂/hBN/Ru heterostructure, the WF modulation results in a rigid shift of the MoSe₂ bandgap with the same magnitude as the WF shift (Fig. 5.3 (d)), signifying that the MoSe₂ band profile modulation is a purely electrostatic effect [66]. Thus, this work illustrates a powerful result: the interactions between the hBN and the Ru substrate can indirectly modulate the electronic structure of an overlying TMD monolayer through dielectric screening and WF modulation.

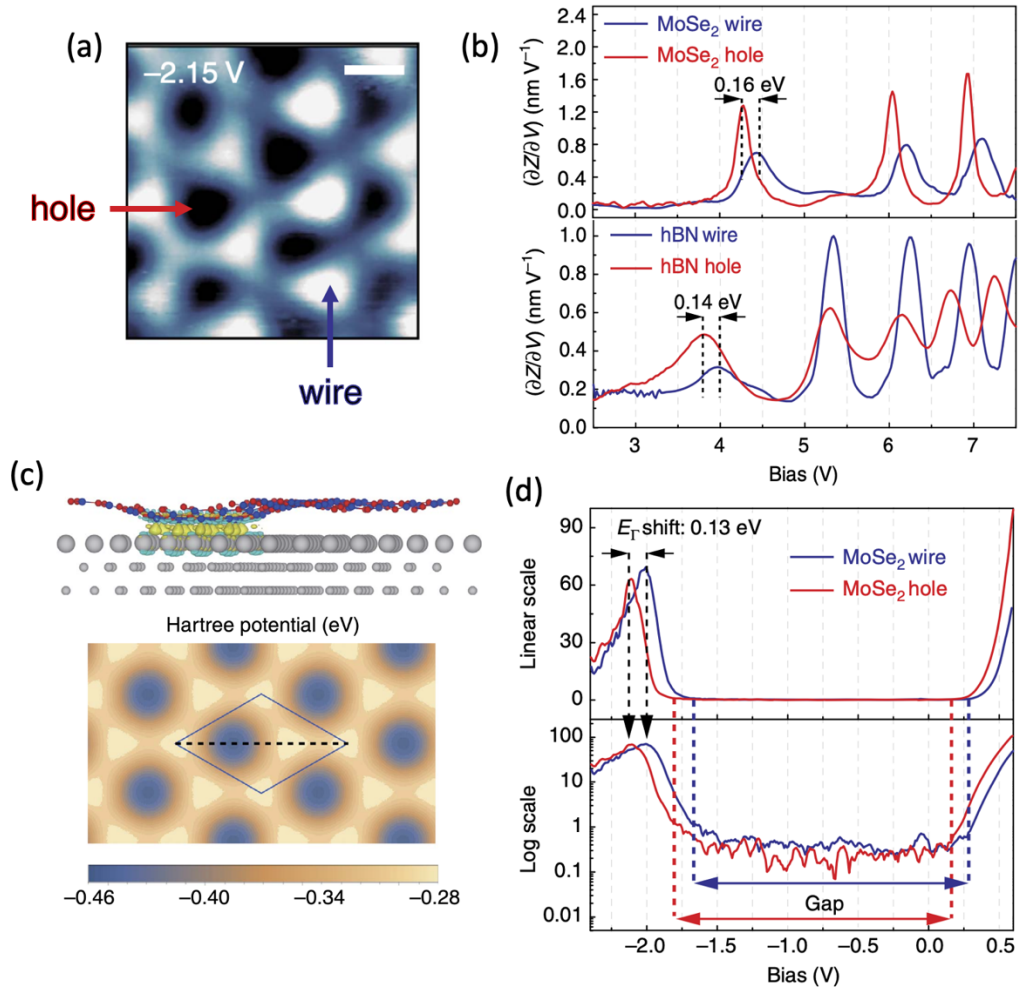


Figure 5.3 (a) STM topographic image of corrugated MoSe₂ on hBN/Ru showing the hole and wire regions. (b) dZ/dV spectroscopy probing the FER of the MoSe₂ hole (red) and wire (blue) regions (top) and hBN (bottom) that shows a similar shift in the work function. (c) Theoretical model of the interaction between the hBN/Ru heterostructure, showing charge transfer at the highly interacting hole regions (top) results in a modulation of the electrostatic potential (bottom) (d) dI/dV spectroscopy of the MoSe₂ at the hole (red) and wire (blue) regions showing a rigid shift in the MoSe₂ band gap due to the change in electrostatic potential. Images taken from Ref. [66]

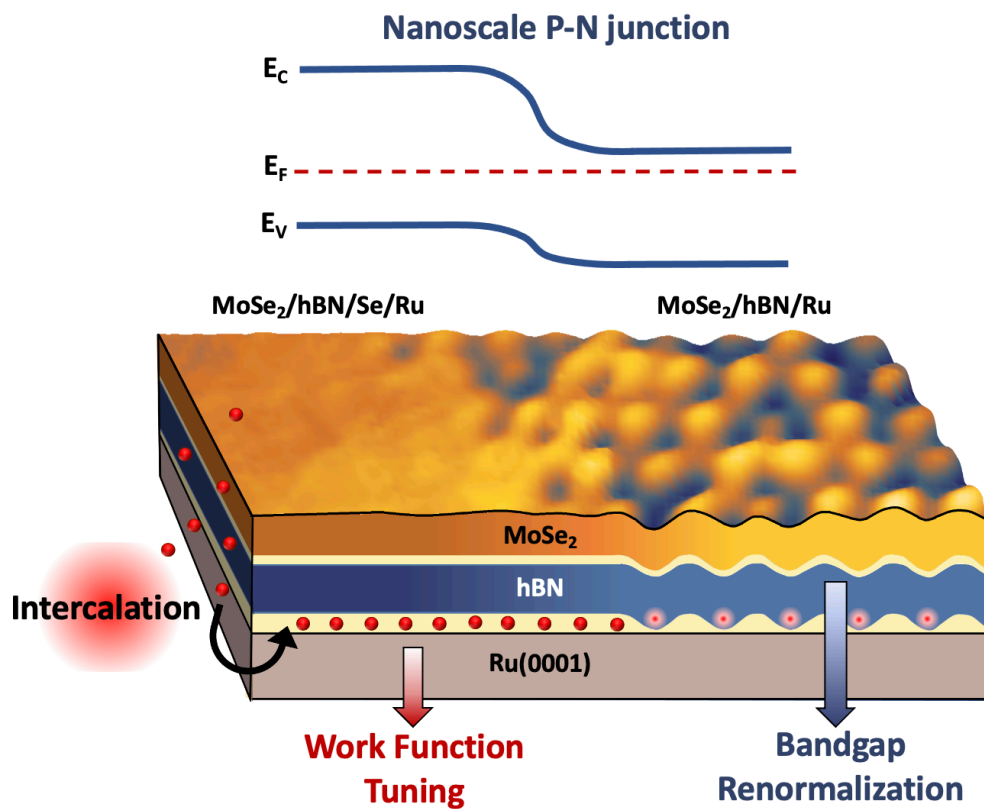


Figure 5.4 A schematic showing the environmental proximity engineering of MoSe_2 on hBN/Ru that has been partially intercalated by Se. The Se intercalation decouples the hBN from the Ru , changing the electronic structure of the hBN/Ru substrate. This results in changing electrostatic screening that renormalizes MoSe_2 the bandgap, as well as tunes the work function of the overlying MoSe_2 layer, creating a lateral P-N heterojunction.

The above study by Zhang et. al. sets the stage for this work, posing an exciting question: can we utilize environmental proximity engineering to create a nanoscale lateral p-n junction in an atomically thin TMD monolayer by tuning the interaction at the hBN/Ru interface? Fortunately, there is no need to discover a new technique to alter the interaction between hBN and transition metal substrates, as intercalation has been thoroughly established as a facile method to achieve this goal. Prior studies have shown that the hBN

layer becomes electronically decoupled from transition metal surfaces when adsorbates are intercalated at the interface, effectively isolating the hBN layer [164-168]. Thus, the MoSe₂/hBN/Ru heterostructure provides an ideal platform for exploration of environmental proximity engineering, as intercalation provides a robust method for tailoring the electronic landscape. Not only does this material system provide the perfect opportunity to simultaneously examine the influence of work function modulation and substrate screening on the overlying TMD monolayer, further, we seek to push the limits of attainable band offsets achieved by environmental proximity engineering.

Here we report the exciting demonstration of a lateral p-n heterojunction within a single homogeneous monolayer of MoSe₂. By intercalating Se at the hBN/Ru(0001) interface, we deliberately tune the hBN electronic structure, dramatically modifying the work function and metallicity of the hBN at the nanoscale, shown pictorially in Figure 5.4. This real space change in the dielectric properties and electrostatic potential landscape in turn influences the band profile of the overlying MoSe₂, which we resolve spatially at the nanoscale using STM/S. We find that through a combination of changes in electrostatic screening and work function, dramatic shifts in the MoSe₂ band structure of more than 500 meV are demonstrated at a nanometer length scale. Further, the direct epitaxial growth and intercalation of the MoSe₂/hBN/Ru is achieved completely in UHV, demonstrating an attractive and scalable approach to heterojunction synthesis. This work illustrates that environmental proximity engineering provides a robust method to indirectly manipulate the band profile of 2D materials outside the limits of their intrinsic properties, opening up new opportunities for device design.

5.2 SYNTHESIS AND INTERCALATION OF hBN/RU(0001) PLATFORM

The MoSe₂/hBN/Ru heterostructure synthesis and intercalation was carried out in UHV, with the transfer between growth chambers the STM characterization chamber completed entirely *in situ*. First, a clean Ru(0001) surface was cleaned by Ar⁺ sputtering (1.5 kV, 5 x 10⁻⁵ Torr Ar) followed by annealing at ~1000 °C by electron beam bombardment in repeated cycles. A monolayer of hBN was then grown on the Ru by leaking a borazine (H₆B₃N₃) precursor vapor into a UHV chamber at a pressure of 1 x 10⁻⁷ Torr for 5 minutes while the Ru was held at 1000 °C, then slowly lowered to room temperature. This UHV CVD technique has been a well-documented method for epitaxial synthesis of high quality hBN monolayers on transition metal surfaces [65, 68, 161, 162, 167, 168]. Figure 5.5 (a) shows an STM image of a typical hBN growth, exhibiting a complete single domain monolayer covering the Ru surface with a distinct nanomesh structure as previously reported [162]. The hBN/Ru was next transferred *in situ* to an MBE chamber for Se intercalation. The intercalation procedure started by heating the sample to 480 °C, then Se was deposited by an effusion cell a rate of 6 Å/min on the hBN surface, at a pressure of 1 x 10⁻⁹ Torr (the chamber base pressure is 3 x 10⁻¹⁰ Torr) for 60 minutes. After the deposition, the hBN/Ru sample was further annealed for 30 minutes, maintained at 480 °C. Upon performing STM measurements on the intercalated hBN/Ru sample (we will call hBN/Se/Ru), it was immediately evident that an interesting change in the surface morphology had occurred. Figure 5.5 (b) shows the appearance of large “flat” regions, along with the typical nanomesh structure of the hBN/Ru. This flattening of the hBN corrugation is typical in intercalation experiments of hBN on transition metals, and is the hallmark sign that the intercalation has decoupled the hBN from the substrate surface [164-167].

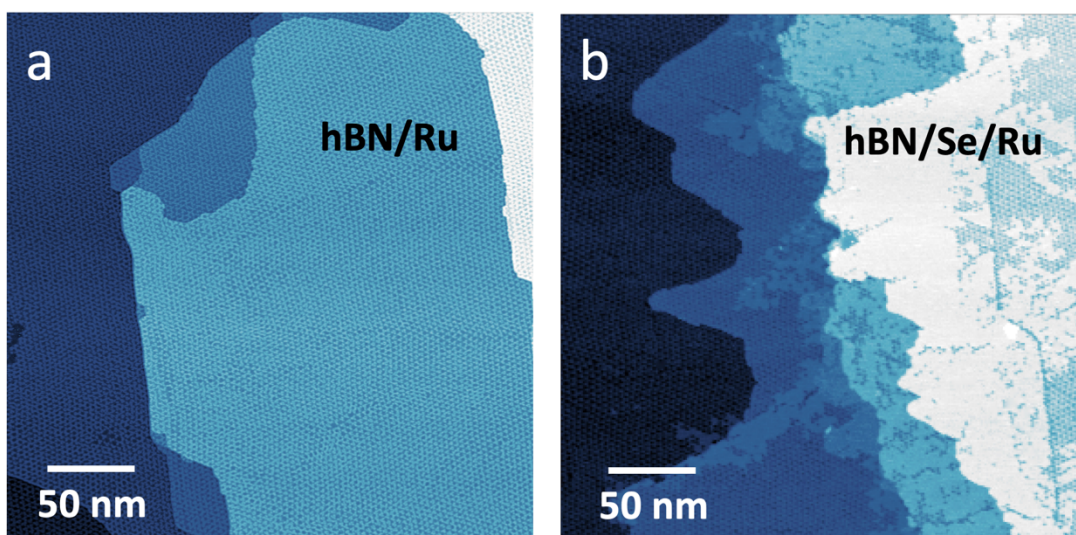


Figure 5.5 (a) Topographic STM image showing a large, well-ordered domain of hBN on Ru with a corrugated surface structure (b) STM image of the same hBN layer after Se intercalation, showing domains of a flat structure have emerged where the hBN has been intercalated. Images obtained at a sample bias of -2 V.

Taking a closer look at the change in the hBN morphology, Figure 5.6 shows topographic STM images of the hBN surface before (a) and after (b) intercalation (see Appendix A for STM methods). Before the intercalation, a height profile from the bare Ru to hBN nanomesh (Fig. 5.6 (c)) shows the hole regions where the hBN is strongly interacting with the Ru (dark contrast) and wire regions where the hBN is weakly interacting (light contrast), leading to the corrugated hBN structure. In contrast, after the intercalation the corrugated nanomesh structure coexists with flat regions without a periodic corrugation (Fig. 5.6 (b)). A height profile from the flat region to the corrugated region shows that the apparent height of the flat hBN is increased when compared to the loosely bound wire regions of the corrugated hBN. This indicates that the presence of the Se at the hBN/Ru interface removes the bonding between the hBN and Ru, effectively isolating the hBN from the Ru substrate, as shown schematically in Figures 5.6 (e), (f). We

note that this topographic behavior is nearly identical to the findings of prior STM studies of intercalated hBN on other transition metal substrates, suggesting this approach can be generalized to other supporting substrates and intercalants [164-167].

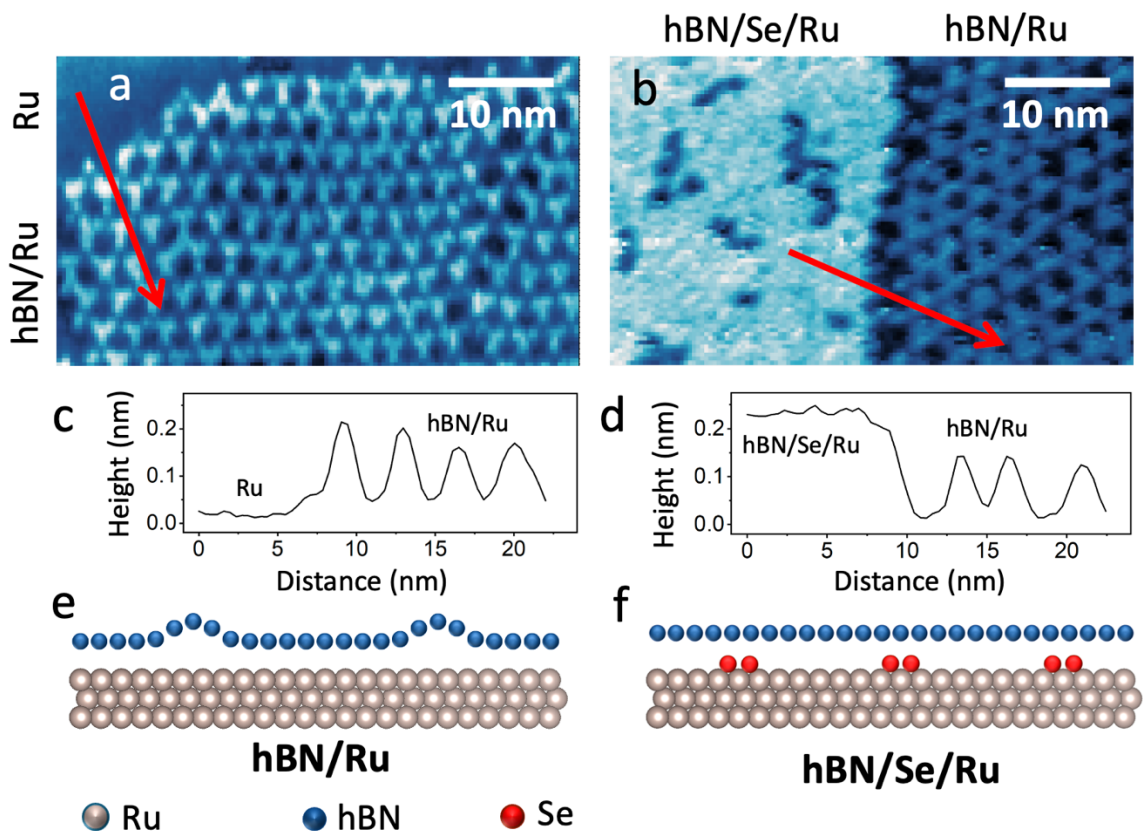


Figure 5.6 (a) STM image of hBN on Ru showing the corrugated hBN structure. (b) STM image of a region of hBN that has been partially intercalated by Se (left). (c) Height profile corresponding to the red line in (a) from the Ru to the hBN. (d) Height profile corresponding to the red line in (b) across the Se intercalated-corrugated interface. (e) A schematic showing the corrugation results from the interaction between the Ru and hBN. (f) Schematic showing the Se intercalation of hBN/Ru substrate, resulting in a flattened structure.

5.3 FIRST PRINCIPLES CALCULATION OF THE INTERCALATED hBN/Se/Ru

We next set out to understand how the Se intercalation at the hBN/Ru interface modifies the electronic structure of the hBN by carrying out a first principles theoretical

calculation (see Appendix F for methods). First, we must determine the Se overlayer configuration on Ru(0001) by calculating the adsorption energy of one Se atom on the Ru(0001) surface in different unit cells representing different concentration values. The Ru(0001) substrate is simulated by the periodic slab method with seven Ru atomic layers arranged in hexagonal close-packed stacking and Se atoms adsorbed on both surfaces, keeping the mirror symmetry with respect to the central layer of Ru. The structure is fully relaxed until the force on each atom is less than 0.01 eV/Å. The adsorption energy, defined with respect to an isolated Se molecule, was determined for different configurations and different adsorption sites. In general, the adsorption strengthens as the surface unit cell increases from 1×1 to 3×3 , namely, the coverage decreases from 1 to 1/9. The hcp site in the 3×3 unit cell is found to be the most stable configuration corresponding to an adsorption concentration of 11.1%. The adsorption energy for a smaller coverage (1/16) does not change much. Therefore, we will use a Se coverage of about 10% in the simulation of Se intercalation into the interface between hBN and Ru(0001).

Rotationally aligned hBN on Ru(0001) corresponds to approximately 13×13 hBN on 12×12 Ru(0001), but this system is too large for plane-wave based calculations. Instead, we have used a supercell of $\sqrt{67}\times\sqrt{67}$ h-BN on $\sqrt{57}\times\sqrt{57}$ Ru(0001) with a small rotational angle of 5.63° , as shown in Figure 5.7 (a). Se atoms are then uniformly distributed in the interface between monolayer h-BN and Ru(0001) with a concentration of about 10.5% (= $6/57$) (Fig. 5.7 (b)). The lateral size of the supercell is about 20.6 Å, and the vacuum region has a thickness of about 27.3 Å. Without Se intercalation, the hBN monolayer on Ru(0001) exhibits large corrugation as shown in Figs. 5.7 (a) as discussed previously [66]. After introducing the Se atoms between h-BN and Ru(0001), the h-BN layer is transformed to an almost flat layer as shown in Figure 5.7 (b). In addition, the average interlayer distance between hBN and Ru(0001) is increased by 1.9 Å. Thus, it can be concluded that the

original moiré pattern of hBN/Ru(0001) will disappear as observed by the STM measurement.

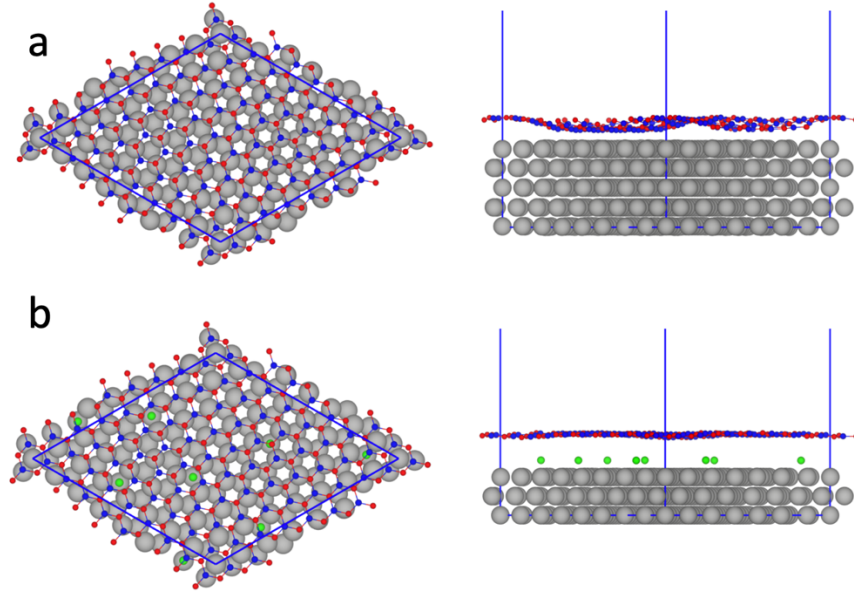


Figure 5.7 (a) Top view (left) and side view (right) of the atomic structure of the hBN/Ru(0001) system. (b) Top view and (d) side view of the atomic structure of the hBN/Se/Ru(0001) system. Blue, red, light-green, and gray spheres represent B, N, Se, and Ru, respectively.

The intercalation of Se atoms induces a dipole layer in the system, which is expected to change the work function. We have calculated the plane-averaged Hartree potential along the z-axis before and after Se intercalation. For *h*-BN/Se/Ru(0001), because of the asymmetric structure of the surfaces on each side and possible charge transfer, a usual dipole correction is adopted in the supercell calculations in order to eliminate the long-range dipole potential to obtain the correct work function. We find that the vacuum level for *h*-BN/Se/Ru(0001) is about 4.87 eV with respect to the Fermi level. For hBN/Ru(0001), it is not enough to add a constant dipole correction since the dipole layer is laterally non-uniform. Therefore, in order to obtain a reliable work function, we use a 5-

layer Ru slab with both sides covered by hBN, which automatically cancels the interfacial dipole on each side. As a result, the plane-averaged Hartree potential in the vacuum region is approximately flat. The average potential is about 3.75 eV above the Fermi level, with the value being 3.68 eV at the valley and 3.80 eV at the hill, respectively. Therefore, the work function difference between hBN/Se/Ru(0001) and hBN/Ru(0001) is calculated to be $4.87 - 3.75 = 1.12$ eV arising from the elimination of the hBN corrugation. As we will uncover later, this work function shift will have a significant impact on the electronic structure of the overlying MoSe₂.

5.4 SYNTHESIS AND INTERCALATION OF MOSE₂/hBN/RU HETEROSTRUCTURE

After confirming the high quality of the hBN/Ru platform, we set out to grow an overlayer of epitaxial monolayer MoSe₂. For this growth, we started with a fresh hBN/Ru heterostructure substrate, which was then transferred *in situ* to a separate chamber for the MoSe₂ growth. We note that this all-UHV approach ensures that the MoSe₂/hBN/Ru heterostructure has a clean interface. The MoSe₂ growth was performed with an e-beam evaporation of high-purity Mo (99.95%) and effusion of Se (99.999%) sources at a ratio of 1:30. The hBN/Ru sample was maintained at 410 °C for a growth of 55 minutes, then the temperature of the Mo source was decreased while the evaporation of the Se continued. The sample was then annealed in the Se vapor while the sample was maintained at the growth temperature for an additional 15 minutes. Thus, the Se intercalation of the hBN was achieved due to Se exposure during MoSe₂ growth and anneal, rather than intercalating the hBN/Ru substrate beforehand.

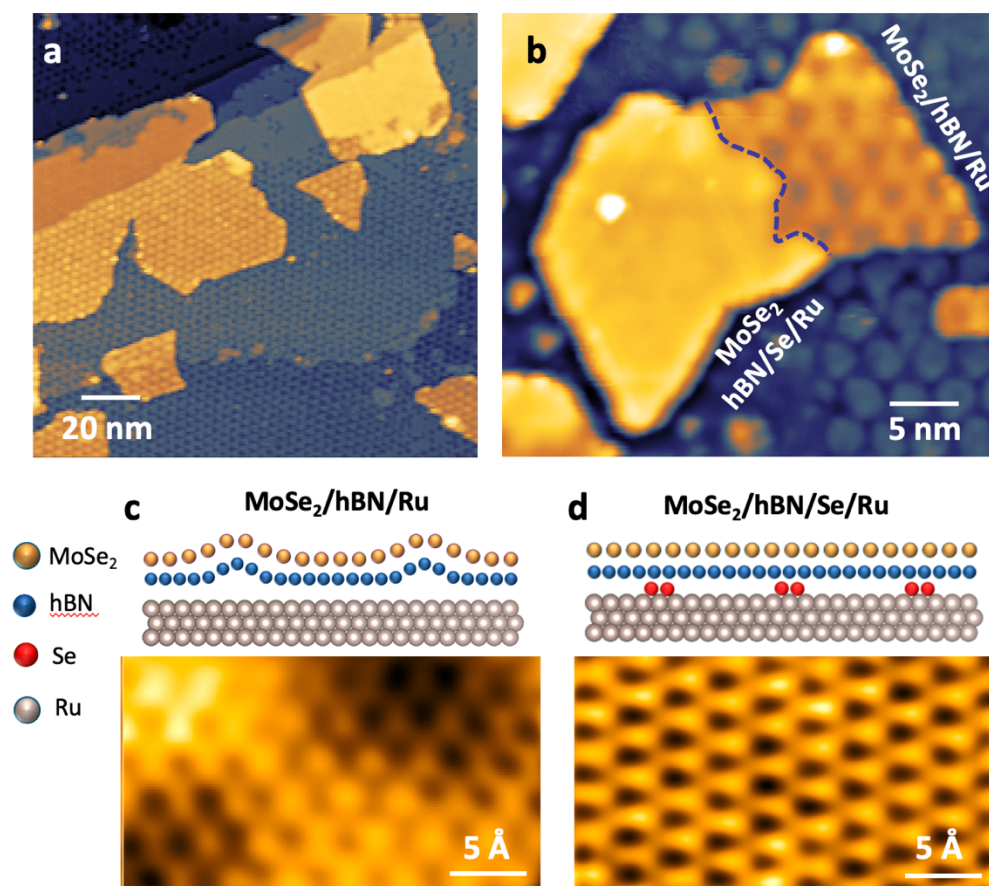


Figure 5.8 (a) STM image of MoSe₂ on Se intercalated hBN (flat) and unintercalated hBN (corrugated) on Ru. (b) STM of a partially Se intercalated flake of MoSe₂ with an interface indicated by the dashed line (c) Atomic resolution STM image of the corrugated MoSe₂. (d) Atomic resolution STM image of flat MoSe₂ on Se intercalated hBN. STM images obtained at a sample bias and current setpoint of (a) V = -2.6 V, I = 5 pAmp (b) V = 3.5 V, I = 5 pAmp (c) V = -1.3 V, I = 0.25 nAmp (d) V = -1.3, V I = 20 pAmp.

The resulting MoSe₂/hBN/Ru heterostructure is shown by an STM topographic image in Figure 5.8 (a). The MoSe₂ structure shows two phases, flat and corrugated, analogous to the intercalated hBN in Figure 5.5 (b), and in stark contrast to the fully corrugated heterostructure reported in the prior study by Zhang et. al. (Fig. 5.2 (a)) [66]. Upon closer inspection, we find the periodicity and phase of MoSe₂ corrugation matches

the corrugation of the underlying hBN, while the expected moiré pattern from the beating of the MoSe₂ and hBN atomic lattices is not present. Figure 5.8 (b) shows a closer view of a MoSe₂ island where both the corrugated and flat phases are present, illustrating that the nanomesh superstructure is barely discernible at the flat region. This change in topography is made more apparent by investigating STM images of the atomic structure of the surface of the corrugated (Fig. 5.8 (c)) and flat (Fig. 5.8 (d)) MoSe₂ phases. As was previously discussed by Zhang et. al., the MoSe₂ corrugation arises from the structural corrugation of the underlying hBN [66]. Therefore, the interaction of the Se decouples the hBN from the Ru substrate and flattens the structure, the overlying MoSe₂ layer will mirror this change as a consequence. Interestingly, the spatial change from the flat to corrugated morphology is quite abrupt, as indicated by the dotted line in Figure 5.8 (b), foreshadowing the prospect of the MoSe₂ electronic structure evolving over the same length scale, as discussed later.

5.5 INFLUENCE OF INTERCALATION ON THE ELECTRONIC STRUCTURE OF THE MOSE₂/HBN/RU HETEROSTRUCTURE

Next, we investigate how the Se intercalation of the hBN transforms the electronic structure of the overlying MoSe₂. Figure 5.9 (a) shows a comparison of dI/dV spectroscopy taken on a flat intercalated region (red) and a corrugated region (blue) of the same MoSe₂ crystal (indicated by the inset). The most conspicuous difference between the two spectra is a pronounced shift in the band edges, as indicated by the black arrows (VBM at the gamma point) and purple arrows (CBM). We note that as discussed above, there is a rigid shift of the band gap between the hole and wire regions, and the corrugated dI/dV spectrum reported here reflects the hole region [66]. We find from the corrugated to the flat intercalated region, there is an increase in energy that shifts the band edges by ~ 0.6 eV at the VBM, and ~ 0.9 eV at the CBM (Fig. 5.9 (a)). We attribute this overall increase in

energy to the change in the work function of the underlying hBN, as we will discuss in detail later. To determine the change in MoSe₂ band gap, we note that the VBM at the K point is located 0.4 eV above the gamma point. Taking this into account, we find a quasiparticle bandgap of ~ 1.9 eV at the corrugated region, which agrees well with the previous report of Ref. [66], and ~ 2.15 eV at the intercalated flat region. This apparent increase of the MoSe₂ band gap at the intercalated domain hints that the screening changes between the two regions, leading to a variation in the strength of the band gap renormalization. Indeed, Figure 5.9 (b) shows dI/dV spectroscopy obtained at the intercalated flat (red) and corrugated (blue) hBN regions, clarifying that the intercalation decreases the conductivity in the band gap of the hBN, which leads to lower screening. However, we note that the band gap of the MoSe₂ on the intercalated hBN (~ 2.15 eV) is comparable to the bandgap of MoSe₂ on HOPG, which implies that the hBN maintains some metallic characteristics even after Se intercalation.

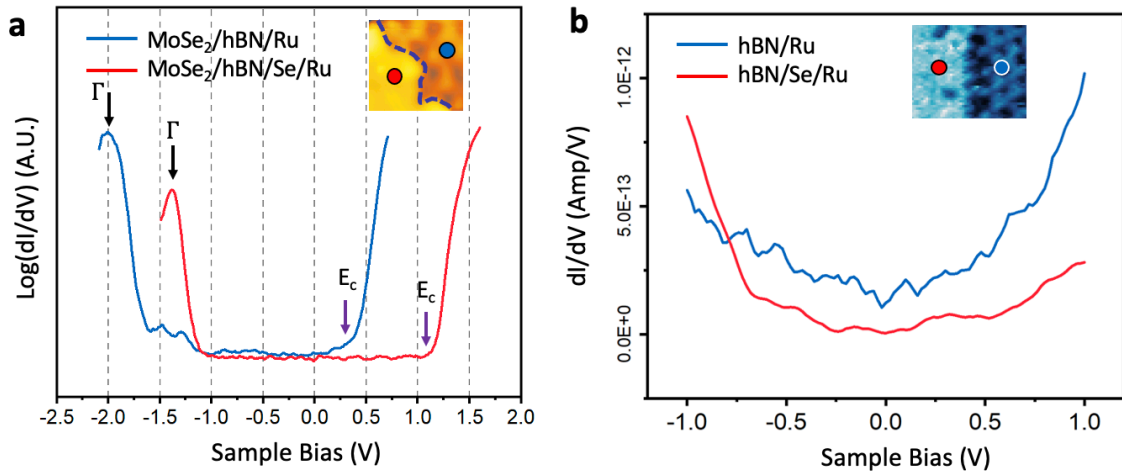


Figure 5.9 (a) dI/dV spectroscopy on MoSe₂/hBN/Ru (corrugated, blue) and Se intercalated MoSe₂/hBN/Se/Ru (flat, red) (b) dI/dV spectroscopy on hBN/Ru (corrugated, blue) and Se intercalated hBN/Se/Ru (flat, red).

5.6 NANOSCALE P-N JUNCTION

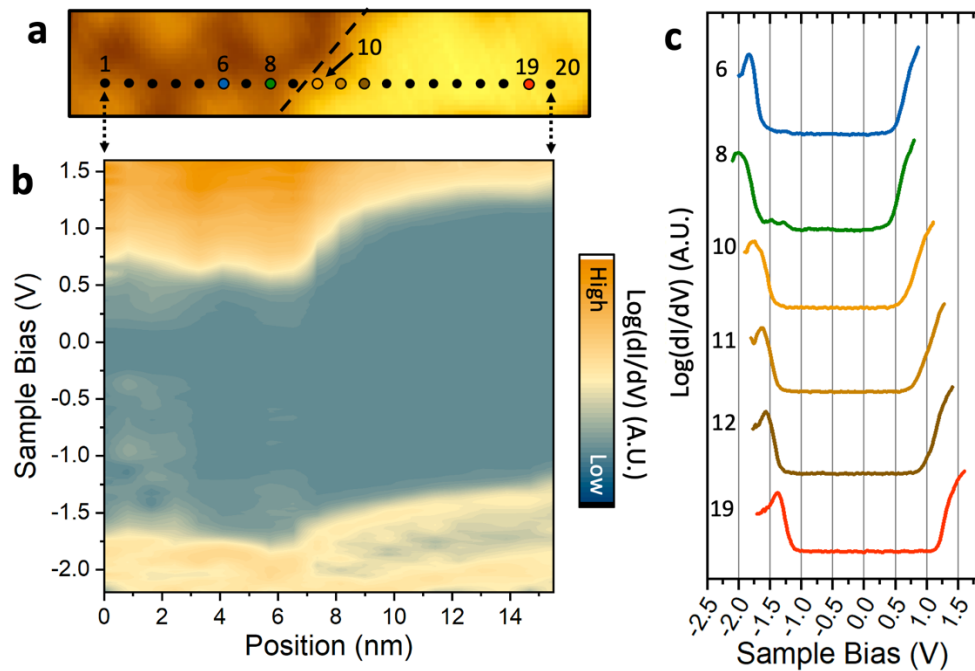


Figure 5.10 (a) STM image of a boundary between the corrugated MoSe₂ and intercalated flat MoSe₂. STS dI/dV spectroscopy was obtained at the points along the interface. (b) Real space 2D color rendering of dI/dV spectroscopy from (a) obtained on the points along a 15.5 nm line (c) Selected spectra from the line indicated in (a), showing the changes in the MoSe₂ bandgap across the intercalation boundary.

Now that we have discovered that the Se intercalation of the hBN induces a pronounced shift in the band gap of the overlying MoSe₂, we investigate the details of the MoSe₂ band profile across the 1D heterointerface between the corrugated and flat regions. Figure 5.10 (a) depicts such an interface where we performed STS dI/dV along a line to spatially resolve the band profile across the boundary. Figure 5.10 (b) depicts a 2D color rendering of the real space modulation of band profile across the interface, exposing the unmistakable characteristic of a lateral p-n junction. We note that the color scale of 2D rendering does not necessarily reflect the band edge locations, although it gives a

qualitative view of the band bending behavior. Thus, Figure 5.10 (c) shows a plot of selected spectra from the line spectroscopy representative of the shifts of the band edges. We point out that the line cut slightly overlaps the hole regions, resulting in a conspicuous modulation rigidly shifting the bandgap across the corrugated side (Fig. 5.10 (c) blue, green) as was previously reported by Zhang et. al. [66]. Intriguingly, close inspection of the spectra in Figure 5.10 unveils that the band gap renormalization begins abruptly at the interface (10 yellow) and is complete within a few nanometers (12 brown), while the shift in the band profile continues (19 red). Accordingly, we will examine the length scales of the band gap renormalization and the electrostatic shift of the band profile separately.

5.6.1 Bandgap Renormalization

We next turn our attention to the detailed spatial modulation of the MoSe₂ quasiparticle band gap across the interface of the Se intercalated hBN. Figure 5.11 (a) shows an STM image of a MoSe₂ island that is partially intercalated, revealing the indicative flattened structure. We performed STS dI/dV measurements across a shorter 6 nm line from the corrugated to flat MoSe₂, as portrayed by the 2D color plot in 5.10 (b). Again, we notice a rigid shift of the MoSe₂ band gap across the hole and wire regions as indicated by the black lines to the left of the interface. At the intercalation boundary, the quasiparticle bandgap begins to widen as marked by the maroon lines, finally reaching a constant value (red lines). We determined the band gap of each of the spectra, and found that the transition begins at a location approximately 1.7 nm into the line spectroscopy. We plotted the measured band gap next the height profile along the same line (Fig. 5.11 (c)) to analyze the details of the transition. Upon closer scrutiny of the of the spatial variation of the MoSe₂ band gap against the line profile, we find the transition is localized to the boundary, and is completed within ~3 nm.

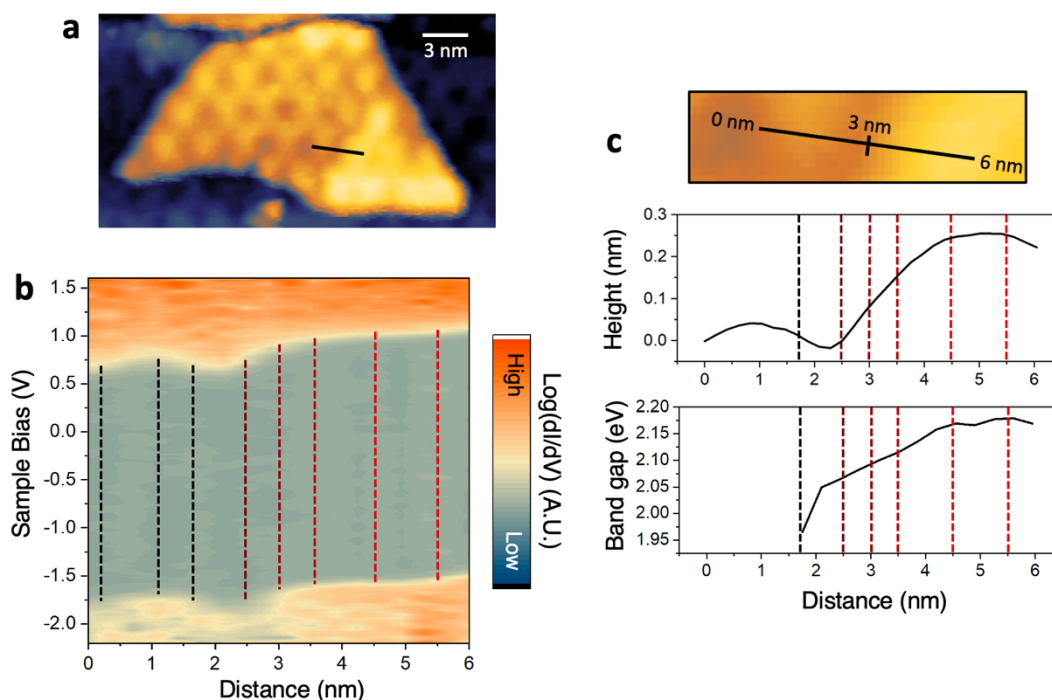


Figure 5.11 (a) STM image showing a partially intercalated MoSe₂ island. STS dI/dV spectroscopy was performed along the black line across the Se intercalation interface. (b) 2D color rendering of the dI/dV spectra along the line across the intercalation boundary. The dotted lines indicate the increase of the MoSe₂ band gap across the interface. (c) The top image is a zoom in of the black line in (a) showing the intercalation boundary, middle shows a height profile across the black line in (a), and bottom is a plot of the MoSe₂ band gap across the interface. The STM image in (a) was obtained at a sample bias and current setpoint of $V = -2$ V and $I = 10$ pAmps.

Theoretical investigations of coulomb engineered heterostructures demonstrated that the band gap reduction occurs within two unit cells, which corresponds to less than a nanometer [150, 154]. However, we note that these calculations considered a spatially abrupt interface where the substrate dielectric constant showed an immediate change. This scenario is unlikely in a real material system, and is certainly not a reasonable assumption for the case of intercalated hBN. In fact, based on our theoretical prediction of the Se intercalation of the hBN as discussed above, the optimum Se coverage at the interface of

the 13×13 hBN on 12×12 Ru(0001) superstructure is reached at $\sim 1/9$. Thus, on the linear scale, the Se will be close to a nanometer apart, which indicates that rather than an “abrupt” interface, a nanometer scale transition region from coupled to decoupled makes intuitive sense. Thus, the length scale of the MoSe₂ band gap renormalization is likely governed by the distance over which the transition of the electronic structure of the intercalated hBN is occurs.

5.6.2 Work Function Tuning

Next, we consider smooth bending of the MoSe₂ band profile from n-doped to intrinsic as the layer crosses over the corrugated-intercalated interface, as observed from the spatially resolved STS spectra (see Figs. 5.10 and 5.11 (b)). As discussed earlier, prior studies have shown that intercalating hBN on transition metal substrates leads to a decoupling of the hBN. Further, the intercalation was shown to change the electrostatic potential, increasing the work function of the essentially “isolated” hBN [166]. Thus, the hBN/Ru platform is the perfect candidate for investigating the role the local work function plays in the electronic properties of a 2D TMD overlayer. First, we use Z-V spectroscopy to examine the field emission resonance FER, as the local work function can be approximated as the bias of the first FER, as previously discussed in Chapters 2 and 3, and thoroughly studied [25, 26]. Figure 5.12 (a) shows the FER of the corrugated hBN (green) and the intercalated flat hBN (orange) showing a fairly dramatic work function increase of ~ 0.85 eV which is similar to the theoretically predicted value discussed above. Note that comparison of the flat intercalated hBN (orange) and the bare Ru (black) is nearly the same, indicating that the addition of the intercalated hBN only slightly lowers the Ru work function (Fig. 5.12 (a)). Further, we probed the work function of the MoSe₂ on top of the corrugated hBN (blue) as well as on the Se intercalated flat (red) hBN, and found that the

work function showed a similar increase of ~ 0.96 eV. Thus, one can anticipate that this dramatic change in the electrostatic potential landscape across the intercalation interface has a pronounced impact on the band profile of the overlying MoSe_2 .

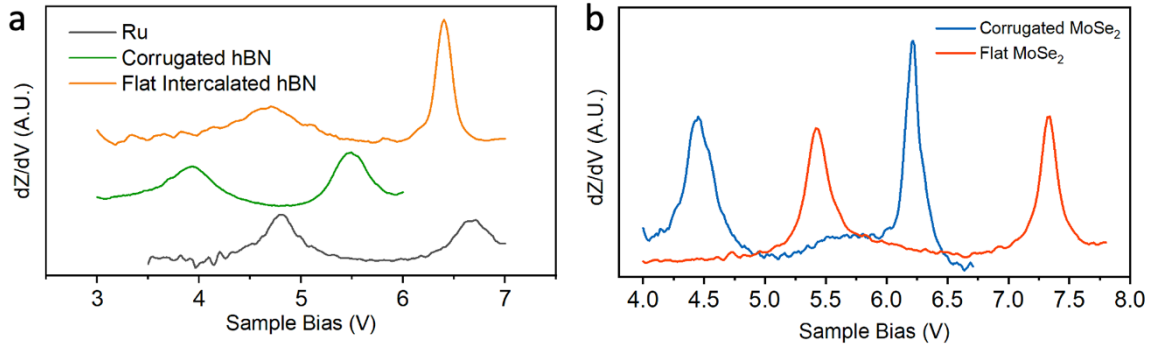


Figure 5.12 (a) dZ/dV spectroscopy on the corrugated (green) and intercalated (flat) hBN, as well as the bare Ru(0001) surface. (b) dZ/dV spectroscopy on the corrugated (blue) and flat (red) MoSe_2 .

We perform dI/dV across the intercalated heterojunction once again, but this time we also carry out dZ/dV across the same line, to further examine the spatial work function modulation. Figure 5.13 (a) is an STM image showing the MoSe_2 junction where the STS was obtained, and Figure 5.13 (b) shows a 2D real space color map of the dZ/dV spectroscopy (top) and dI/dV spectroscopy (bottom). We note that although these measurements were taken after the STM had stabilized for hours, but there is ~ 0.5 nm uncertainty in the alignment of the dZ/dV and dI/dV measurements due to drift. The band profile of the MoSe_2 shows the same characteristic p-n electronic structure across the junction as previously discussed (Figs. 5.10, 5.11 (b)), but comparison with the corresponding work function profile elucidates the strong influence of the underlying hBN. The FER peaks and the CBM of the MoSe_2 show a very similar modulation, giving strong evidence for real space electrostatic tuning across the interface. We further identified the

CBM of each of the dI/dV spectra, and the location of the first FER of the dZ/dV spectra, and plotted them together for closer inspection (Fig. 5.13 (c)). After shifting the energy to overlap the curves, we see that they follow a similar energy profile across the interface. This tracking of the CBM and work function across the interface affirms the idea that the intercalation decouples the hBN from the Ru substrate, increasing the hBN work function, and thereby tunes the MoSe_2 band profile.

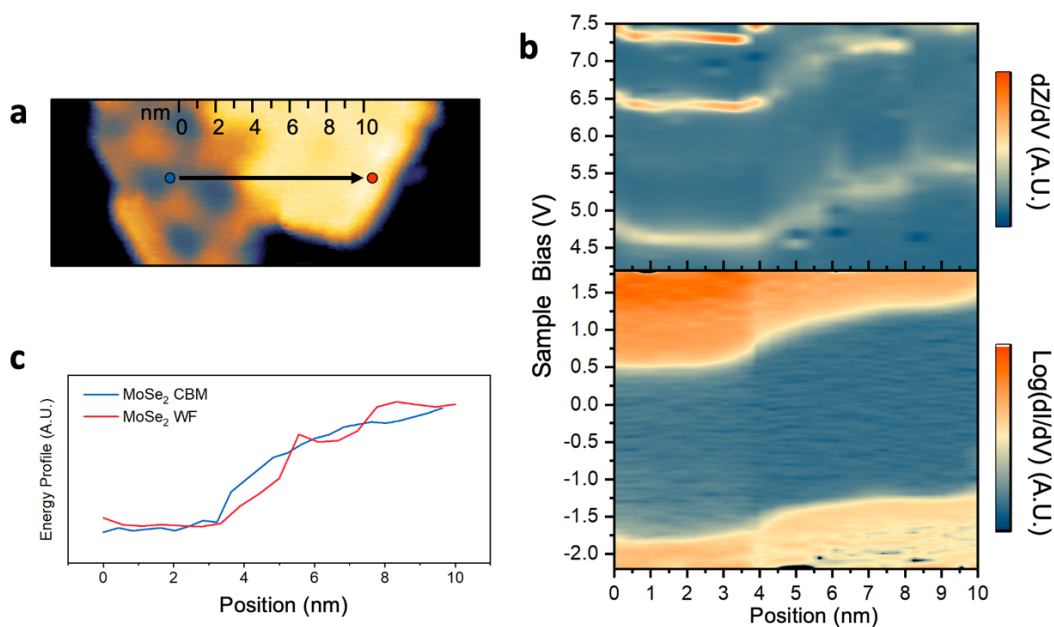


Figure 5.13 (a) STM of a partially Se intercalated MoSe_2 island. (b) 2D color rendering of the dZ/dV (top) and dI/dV spectroscopy obtained along the black line in (a). (c) Plot of the first FER measured for the dZ/dV spectra (red) overlaid with the CBM position obtained from the dI/dV spectra (blue).

5.6.3 Theoretical Model for the Nanoscale P-N Junction

We next seek to apply a theoretical model to derive the band bending of the MoSe_2 p-n junction across the boundary of the Se intercalated hBN. In contrast to conventional bulk p-n junction, the nature of a nanoscale p-n junction within a single 2D layer is inherently more complex due to the low dimensionality. In the 2D case, the charge carriers

are located in-plane, while the junction electric field is primarily concentrated in the environment (Fig. 5.14 (a)). To further complicate matters, the MoSe₂ p-n junction shows a striking asymmetry, with the majority of the band bending occurring at the intercalated side of the metallurgical junction. This behavior arises from the strong screening of the electric field in the highly n-doped corrugated MoSe₂, with the transition of the band profile occurring in the depletion region of the nearly intrinsic intercalated MoSe₂, shown schematically in Figure 5.14 (b). The influence of dimensionality on p-n junctions has surprisingly received low interest until recently, but fortunately there are several thorough studies that have set out to take on the complex problem of modelling 1D p-n junctions in a 2D layer.

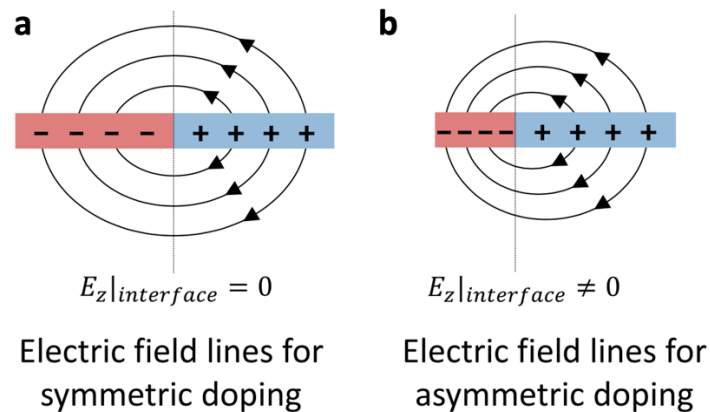


Figure 5.14 Schematic of the 2D depletion region of a symmetric doped (a) and asymmetric doped (b) p-n junction. Images taken from Ref. [169]

We will adopt the approach of Ilatikhameneh et. al. to model the MoSe₂ 2D p-n junction [170]. For wide 2D semiconducting sheets with a thickness much smaller than the depletion width, and a depletion width much smaller than the extent of the sheet, we can model the depletion region as a group of infinite line charges [169, 170]. First, recall that the electric field due to an infinite line of charge follows the equation:

$$\vec{E}(\vec{r}) = \frac{qN}{2\pi\epsilon|\vec{r}|}, \quad (5.1)$$

where \vec{r} is the radial distance from the line, N is the linear charge density, and ϵ is the dielectric constant of the surrounding media. To obtain the electric field as a function of position across the depletion region, Ilatikhameneh et. al. then apply a clever trick of using image charges to satisfy the boundary conditions at the charge neutral regions. Once they obtained an expression for the electric field, the electrostatic potential profile is calculated by integrating the electric field across the 2D lateral p-n junction. The important point to note is that the electric field has an inverse dependence on the distance from the line of charge, therefore, it is evident that the potential will have a logarithmic dependence on position. For the case of a 2D semiconduction flake with a thickness much smaller than the depletion width, they find the following expression for the electrostatic potential:

$$V(x) = \frac{qN}{\pi\epsilon}(d-x)\ln(x-d) - d\ln(d) + x\ln(x), \quad (5.2)$$

where d is the width of the depletion region.

Figure 5.15 shows the same plot of the MoSe₂ conduction band minimum across the p-n junction from Figure 5.13 (c) (black), with the theoretical model of the electrostatic potential from Eq. 5.2 overlaid (red). It is apparent that the logarithmic model fits the data well, providing evidence that the electrostatic potential across a 1D p-n junction within a 2D layer is governed by logarithmic position dependence. However, we note that this model only considers a uniform dielectric environment, and symmetric doping across the junction. Therefore, our analysis cannot be considered quantitative, but rather qualitatively shows the logarithmic position dependence of the p-n junction. We note that the band bending of the MoSe₂ cannot be considered solely due to the difference in doping at the different sides of the heterojunction, like typical p-n heterojunctions. Instead, the band bending of the overlying MoSe₂ follows the change of the electrostatic potential and

electrostatic screening of the hBN substrate, however, the line charge model is also reasonable interpretation for the hBN potential landscape. Further theoretical investigations are necessary to understand the complex scenario of asymmetric doping a nonuniform dielectric environment across the junction.

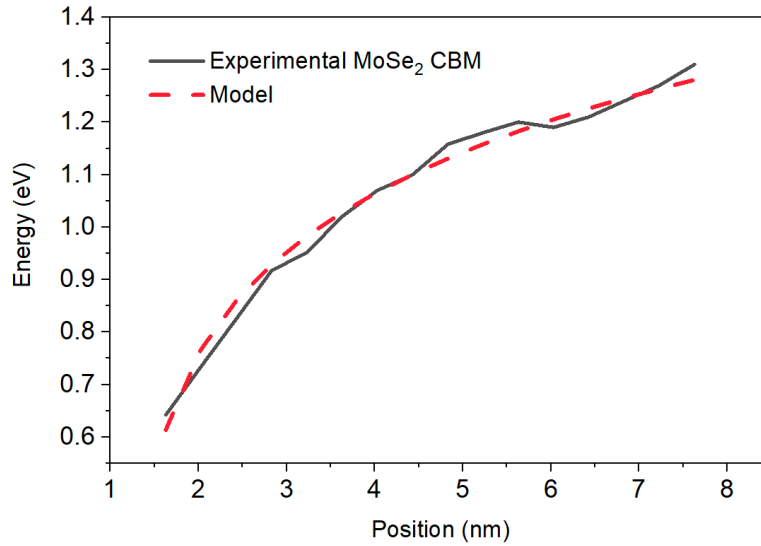


Figure 5.15 Plot of the MoSe₂ CBM position at the Se intercalation boundary from 5.13 (c) (black) with fitted model of the electrostatic potential from Eq. 5.2 (red). Parameters $d = 1.1$ nm and $\frac{qN}{\pi\epsilon} = 0.25$ were used for the fitting.

5.6.4 Summary of the Band Offsets and Work Function of MoSe₂ P-N Junction

Finally, we summarize our findings of the band offset and work function tuning of the nanoscale MoSe₂ p-n junction, outlined in Table 5.1 below. Interestingly, we see that the shift of MoSe₂ closely tracks the shift of the hBN work function, indicating that the electrostatic potential of the underlying substrate molds the band profile of the overlying MoSe₂ layer. A puzzling characteristic of the modulation of the MoSe₂ quasiparticle bandgap is the asymmetry in the band shifts of the MoSe₂ VBM and CBM. Theoretical

investigations have predicted that band gap renormalization should be symmetric at the VBM and CBM; in other words, the VBM and CBM should shift up and down the same amount in energy, respectively [150, 155, 157]. However, if this is the case, then the electron affinity of the corrugated MoSe₂ should be larger than that of the flat MoSe₂ on the intercalated hBN. However, when we calculate the electron affinity by subtracting the CBM position from the measured work function, we find that the flat MoSe₂ electron affinity is actually larger, which is a striking contradiction to this prediction. Thus, it is clear that for environmental proximity engineering to be a useful, predictable, and controllable tool for deliberately shaping the band profile, more experimental and theoretical investigations are necessary to tease apart the complex underlying physical phenomena at play.

| Units eV | WF hBN | WF MoSe ₂ | MoSe ₂ CBM | MoSe ₂ VBM | MoSe ₂ band gap | MoSe ₂ E.A. |
|------------|--------|----------------------|-----------------------|-----------------------|----------------------------|------------------------|
| Corrugated | 3.9 | 4.63 | 0.32 | -1.57 | 1.89 | 4.31 |
| Flat | 4.75 | 5.6 | 1.2 | -0.94 | 2.14 | 4.4 |
| Shift | 0.85 | 0.97 | 0.88 | 0.63 | 0.25 | 0.09 |

Table 5.1 Summary of the work function tuning of the corrugated and intercalated MoSe₂ and hBN, and the band edges of the flat and Se intercalated MoSe₂.

5.7 CONCLUSION

In conclusion, this study affirms that environmental proximity engineering as an invaluable tool to indirectly create a nanoscale lateral p-n junction within a single atomic layer of MoSe₂. This p-n junction was synthesized utilizing a scalable, facile, method of all UHV in situ epitaxial growth and intercalation with Se vapor. We further mapped out the nanoscale band profile of the MoSe₂ p-n junction by direct observation using STM/S

characterization, and analyzed the influence of substrate screening and work function tuning of the MoSe₂ from the electrostatic landscape of the intercalated hBN substrate. We demonstrate band offsets exceeding 500 meV, showing that the combination of work function tuning and band gap renormalization can achieve larger band offsets than previously reported monolayer lateral p-n junctions created by other approaches [138, 157, 160]. Thus, intercalation of hBN on transition metal substrates provides a unique platform for exploring the playground environmental proximity engineering, and can be generalized as a platform for future investigations of TMD band engineering.

Appendices

Appendix A: STM Methods

All STM measurements were performed at 77 K with a chemically etched tungsten tip. The tips are then cleaned in UHV by electron bombardment with an applied bias of 1.5 kV for 5 minutes. The bias voltages were defined as the sample bias, and the topographic images were taken using constant current mode. The chamber base pressure is 5×10^{-11} Torr during measurements. The STM topography images were processed using Gwyddion software, and the STS was processed using the Origin software.

Appendix B: Determination of the BeO Atomic Fraction with XPS

After normalization to the photoionization cross-section, the XPS signal gives the atomic fraction of each element within the probed volume. With knowledge of the electron inelastic mean free path, one can calculate the anticipated ratio of the Ag and Be signals since the BeO lies on top of the Ag substrate. Due to the difference in lattice constant, the Be density is 1.18 times greater than Ag per atomic layer. However, the Ag signal is the sum of many layers, and the attenuation of the Ag signal traveling to the surface needs to be taken into account. If the inelastic mean free path of Ag at a specific kinetic energy is λ_{Ag} , the thickness of the BeO layer is d_{Be} , and the density of the Ag is D_{Ag} , then the attenuated signal of the first layer $N = 1$ is:

$$S_{Ag}(1) = D_{Ag} \exp\left(-\frac{d_{Be}}{\lambda_{Ag}}\right),$$

As shown in Figure B (a) below. To calculate the next layer, we need to take the attenuation through both the BeO layer and the first Ag layer into account. If the thickness of the Ag layer is d_{Ag} , then the attenuation of the second layer $N = 2$ is:

$$S_{Ag}(2) = D_{Ag} \exp\left(-\frac{d_{Be}}{\lambda_{Ag}}\right) \exp\left(-\frac{d_{Ag}}{\lambda_{Ag}}\right)$$

As each consecutive layer will be attenuated by the top Be layer, it follows that the final expression for the total Ag signal with the contribution from each layer is:

$$S_{Ag} = D_{Ag} \exp\left(-\frac{d_{Be}}{\lambda_{Ag}}\right) \sum_{N=1}^{\infty} \exp\left(-\frac{(N-1)d_{Ag}}{\lambda_{Ag}}\right)$$

Since the BeO layer is on the surface it is not attenuated, the Be signal is simply:

$$S_{Be} \propto D_{Be}$$

Where D_{Be} is the Be density. As the elements have been normalized by their photoionization cross section, the ratio of the signals gives:

$$\frac{S_{Ag}}{S_{Be}} = \frac{D_{Ag}}{D_{Be}} \exp\left(-\frac{d_{Be}}{\lambda_{Ag}}\right) \sum_{N=1}^{\infty} \exp\left(-\frac{(N-1)d_{Ag}}{\lambda_{Ag}}\right)$$

Here, $\frac{D_{Ag}}{D_{Be}} = 0.85$ is the ratio of the atomic density per layer, and $d_{Be} = 3.0 \text{ \AA}$ and $d_{Ag} = 2.36 \text{ \AA}$ is the atomic layer thickness for Ag and Be respectively. The XPS measurements were acquired using a Kratos XPS system with X-ray photon energy of 1486.6 eV. The electron kinetic energy for the Ag is therefore $\sim 1100 \text{ eV}$, and the electron inelastic mean free path of Ag at this energy is $\lambda_{Ag} = 15.2 \text{ \AA}$ [Tanuma, S. and Powell, C. J., Surf. Int. Anal. 43, 689-713 (2011)]. The calculation yields a value of $\frac{S_{Ag}}{S_{Be}} = 4.85$. If we use an escape depth of $\lambda_{Ag} = 14 \text{ \AA}$, then the calculation yields a ratio of $\frac{S_{Ag}}{S_{Be}} = 4.40$. Experimentally, we observe a value of 4.23. Given the uncertainty in the escape depth, the result is consistent with 1 ML of honeycomb BeO on the Ag substrate.

If we assume that there are two layers of BeO on the Ag surface (Figure B (b)), the calculation must be modified taking into account the attenuation of the Be through the top BeO layer, as well as the Ag attenuating through two layers of Be. Following the above logic, the equation becomes:

$$\frac{S_{Ag}}{S_{Be}} = \frac{D_{Ag}}{D_{Be}} \frac{\exp\left(-\frac{2d_{Be}}{\lambda_{Ag}}\right)}{\left(1 + \exp\left(-\frac{d_{Be}}{\lambda_{Be}}\right)\right)} \sum_{N=2}^{\infty} \exp\left(-\frac{(N-2)d_{Ag}}{\lambda_{Ag}}\right)$$

Where λ_{Be} is the inelastic mean free path of Be. With a kinetic energy of $\sim 1300 \text{ eV}$, we find $\lambda_{Be} = 25.1 \text{ \AA}$ [Tanuma and Powell]. This calculation gives a ratio of 2.57, which differs dramatically from our experimental observation by $\sim 40\%$. This analysis supports our assertion that the XPS signals indicate that our growth is indeed a monolayer.

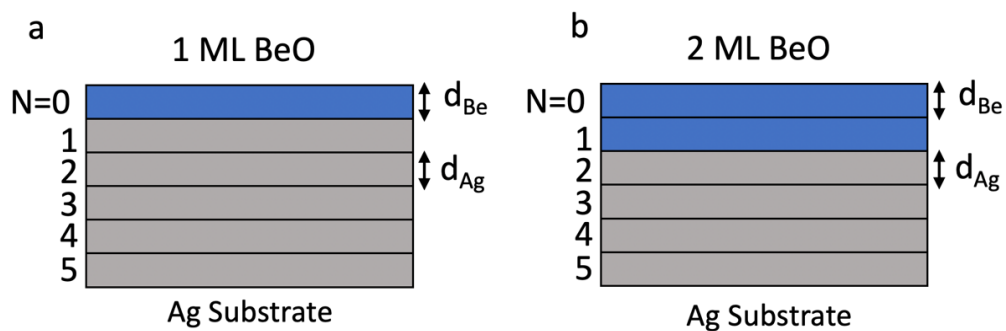


Figure B Schematic of the BeO surface on top of the atomic layers of the Ag substrate for monolayer (a) and bilayer (b) BeO. N is the layer of number, d_{Be} is the BeO layer thickness, and d_{Ag} is the Ag atomic layer thickness.

Appendix C: STM Calibration

The accuracy of the lattice constant determination using atomic STM images depends critically on calibration. This is achieved by using the STM image of Pb film with a known lattice constant of 3.50 \AA (Figure C). We use measurements along three close packed atomic rows (one of which is marked by white dashed line), yielding an average value of 2.61 \AA with a standard deviation of 0.08 \AA . Below the STM image is a line profile that corresponds to the white line. Note the Ag lattice constant is 2.89 \AA , a difference far larger than our experimental uncertainty.

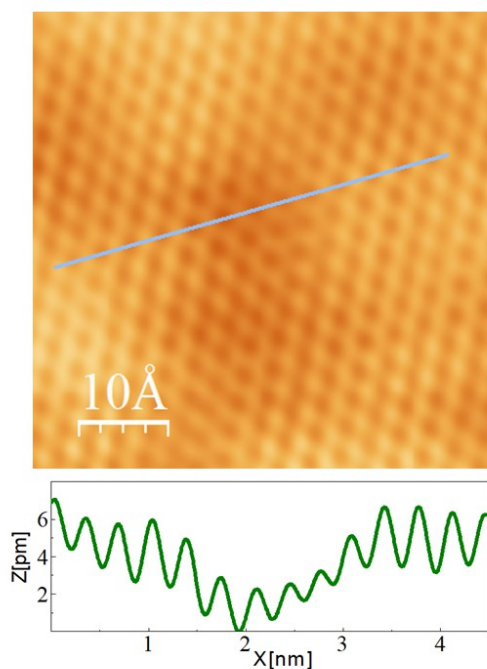


Figure C STM image with sample bias of -29 mV and 50.7 pAmp set point showing an atomic Pb film. Below is a line profile corresponding to the white line in the image. This image was processed using the WSXM software and used as a calibration for the atomic BeO.

Appendix D: Methods of BeO/Ag(111) First Principles Theoretical Calculation

Our first-principles calculations were performed using the Vienna ab-Initio simulation package (VASP) [171, 172] with the projector augmented wave method [173, 174]. The slab contains three layers of Ag atoms with the bottom two layers fixed and a vacuum region of about 16 Å. A plane-wave cut-off energy of 500 eV was used, and only the Gamma point was sampled for this large supercell. The optB86b functional including the van der Waals correction [175] was adopted for the structural relaxation. A dipole correction scheme was used to eliminate the long-range effect arising from the surface dipole between monolayer BeO and the Ag substrate. The atomic positions were fully relaxed until the force on each atom was smaller than 0.01 eV Å⁻¹. For the local work function calculation, we took the difference between the Fermi level and the electrostatic potential at the center of the vacuum above a specific region.

Appendix E: Methods of WS₂ S Vacancy First Principles DFT Calculation

DFT calculations were performed using Vienna Ab initio Simulation Package (VASP) [171, 172] in which Generalized gradient approximations (GGA) of Perdew-Burke-Ernzerhof (PBE) [176] have been adopted for exchange-correlation potential. A supercell of 6×6 WS₂ unit cell was used, with the lattice constant of unit cell 3.19 Å and a 20 Å thick vacuum was inserted. For each type of defect, the structure is relaxed with a quasi-Newton algorithm, which relaxes the ions into their instantaneous ground state. Relaxation is realized so that all forces are smaller than 0.01 eV/Å. During the self-consistent (SC) calculations the global break condition for the electronic SC-loop is set to be 10⁻⁷ eV and the cutoff energy for the plane wave basis set is 400 eV, k-point sampling is set to be 8×8×1 with a Gaussian smearing method, in which the smearing width is 0.05 eV.

The STM images were simulated with Quantum Espresso (QE) [177], in which the charge density is self-consistently calculated without the spin-orbit coupling, the pseudopotentials used in QE are Optimized Norm-Conserving Vanderbilt Pseudopotential, kinetic energy cutoff for wavefunctions was set to be 60 Ry and kinetic energy cutoff for charge density was 240 Ry. During the SC calculations the convergence threshold is 5×10⁻⁸ Ry. STM images were simulated with a with constant current mode and the bias of the sample in STM images is 1.1 V.

Appendix F: Methods of hBN/Ru(0001) and hBN/Se/Ru(0001) First Principles Theoretical Calculation

We have performed first-principles calculations with density functional theory (DFT) as implemented in the Vienna Ab initio Simulation Package (VASP) [171, 172]. We used the projector augmented wave (PAW) method [173, 174] to treat core electrons with a plane-wave cutoff energy of 400 eV. For the Se/Ru(0001) system, we used the Perdew-Burke-Ernzerhof (PBE) form [176] for the exchange correlation functional. The Monkhorst-Pack k-point mesh of $21 \times 21 \times 1$ was used for 1×1 reconstruction and scale down as the unit cell increases. For the h-BN/Se/Ru(0001) system, the periodic slab contained three Ru layers as the substrate. The dipole correction was adopted to compensate the dipole moment induced by asymmetric surfaces of the slab. For the h-BN/Ru(0001) system, the slab contained five layers of Ru with both sides covered by the h-BN layer. We used a supercell of $\sqrt{67} \times \sqrt{67}$ h-BN on $\sqrt{57} \times \sqrt{57}$ Ru(0001) with a small rotational angle of 5.63° between the h-BN monolayer and the Ru substrate. The Se layer concentration is about 10.5% ($= 6/57$). For both systems, the optB86b functional including the van der Waals correction [175] was adopted for the structural relaxation. The structure was fully relaxed until the force on each atom was smaller than $0.01 \text{ eV } \text{\AA}^{-1}$. The Monkhorst-Pack k-point mesh of $2 \times 2 \times 1$ was used.

References

1. R.P. Feynman, *There's Plenty of Room at the Bottom: An Invitation to Enter a New Field of Physics*. Resonance, 2011.
2. A.K. Geim and I.V. Grigorieva, Van der Waals heterostructures. *Nature*, 2013. **499**(7459): p. 419-25.
3. A.H. Castro Neto, et al., The electronic properties of graphene. *Reviews of Modern Physics*, 2009. **81**(1): p. 109-162.
4. K.S. Novoselov, et al., Electric field effect in atomically thin carbon films. *Science* 2004. **306**: p. 4.
5. G. Fiori, et al., Electronics based on two-dimensional materials. *Nat. Nanotechnol.*, 2014. **9**(10): p. 768-79.
6. D. Jariwala, et al., Emerging device applications for semiconducting two-dimensional transition metal dichalcogenides. *ACS Nano*, 2014. **8**: p. 19.
7. M. Chhowalla, D. Jena, and H. Zhang, Two-dimensional semiconductors for transistors. *Nat. Rev. Mat.*, 2016. **1**.
8. H. Zhang, et al., Epitaxial growth of two-dimensional insulator monolayer honeycomb BeO. *ACS Nano*, 2021. **15**(2): p. 2497-2505.
9. A. Splendiani, et al., Emerging photoluminescence in monolayer MoS₂. *Nano. Lett.*, 2010. **10**(4): p. 1271-5.
10. K.F. Mak, et al., Atomically thin MoS(2): a new direct-gap semiconductor. *Phys. Rev. Lett.*, 2010. **105**(13): p. 136805.
11. X. Xu, et al., Spin and pseudospins in layered transition metal dichalcogenides. *Nat. Phys.*, 2014. **10**(5): p. 343-350.
12. G. Binnig and H. Rohrer, Scanning tunneling microscopy. *Helvetica Physica Acta*, 1982. **55**: p. 9.
13. G. Binnig, et al., Surface studies by scanning tunneling microscopy. *Phys. Rev. Lett.*, 1982. **49**(1): p. 57-61.
14. G. Binnig, et al., 7×7 Reconstruction on Si(111) resolved in real space. *Phys. Rev. Lett.*, 1983. **50**(2): p. 120-123.
15. C.J. Chen, *Introduction to Scanning Tunneling Microscopy*. 2015, Oxford: Oxford University Press.
16. J. Bardeen, Tunneling from a many-particle point of view. *Phys. Rev. Lett.*, 1961. **6**(2): p. 57-59.
17. D.J. Griffiths, D.F. Schroeter, and P. Cambridge University, *Introduction to quantum mechanics*. 2019, Cambridge: Cambridge University Press.
18. J. Tersoff and D.R. Hamann, Theory and application for the scanning tunneling microscope. *Phys. Rev. Lett.*, 1983. **50**(25): p. 1998-2001.

19. J. Tersoff and D.R. Hamann, Theory of the scanning tunneling microscope. *Phys. Rev. B Condens Matter*, 1985. **31**(2): p. 805-813.
20. C. Zhang, et al., Probing critical point energies of transition metal dichalcogenides: surprising indirect gap of single layer WSe₂. *Nano. Lett.*, 2015. **15**(10): p. 6494-500.
21. B.C. Stipe, M.A. Rezael, and W. Ho, Single molecule vibrational spectroscopy and microscopy. *Science*, 1998. **280**: p. 4.
22. Q.-Y. Wang, et al., Interface-induced high-temperature superconductivity in single unit-cell FeSe films on SrTiO. *Chinese Physics Letters*, 2012. **29**(3).
23. M.F. Crommie, C.P. Lutz, and D.M. Eigler, Confinement of electrons to quantum corrals on a metal surface. *Science*, 1993. **262**: p. 3.
24. S. Gwo, et al., Direct mapping of electronic structure across Al_{0.3}Ga_{0.7}As/GaAs heterojunctions: Band offsets, asymmetrical transition widths, and multiple-valley band structures. *Phys. Rev. Lett.*, 1993. **71**(12): p. 1883-1886.
25. J.A Stroschio, R.M. Feenstra, and A.P. Fein, Electronic structure of the Si(111)2 x 1 surface by scanning-tunneling microscopy. *Phys. Rev. Lett.*, 1986. **57**(20): p. 2579-2582.
26. R.S. Becker, J.A. Golovchenko, and B.S. Swartzentruber, Electron interferometry at crystal surfaces. *Phys Rev Lett*, 1985. **55**(9): p. 987-990.
27. J.H. Coombs and J.K. Gimzewski, Fine structure in field emission resonances at surfaces. *J. of Microscopy*, 1988. **152**: p. 11.
28. Y. Pan, et al., Highly ordered, millimeter-scale, continuous, single-crystalline graphene monolayer formed on Ru (0001). *Adv. Mat.*, 2009. **21**(27): p. 2777-2780.
29. T.A. Chen, et al., Wafer-scale single-crystal hexagonal boron nitride monolayers on Cu (111). *Nature*, 2020. **579**(7798): p. 219-223.
30. B. Lalmi, et al., Epitaxial growth of a silicene sheet. *Appl. Phys. Lett.*, 2010. **97**(22).
31. Z.-L. Liu, et al., Various atomic structures of monolayer silicene fabricated on Ag(111). *New J. of Phys.*, 2014. **16**.
32. M.E. Dávila, et al., Germanene: a novel two-dimensional germanium allotrope akin to graphene and silicene. *New J. of Phys.*, 2014. **16**.
33. F.F. Zhu, et al., Epitaxial growth of two-dimensional stanene. *Nat. Mater.*, 2015. **14**(10): p. 1020-5.
34. J. Yuhara, et al., Large area planar stanene epitaxially grown on Ag(1 1 1). *2D Mater.*, 2018. **5**(2).
35. B. Feng, et al., Experimental realization of two-dimensional boron sheets. *Nat. Chem.*, 2016. **8**(6): p. 563-8.
36. G.P. Campbell, et al., Resolving the chemically discrete structure of synthetic borophene polymorphs. *Nano. Lett.*, 2018. **18**(5): p. 2816-2821.
37. , C.L. Freeman, et al., Graphitic nanofilms as precursors to wurtzite films: theory. *Phys. Rev. Lett.*, 2006. **96**(6): p. 066102.
38. H. Zheng, et al., Monolayer II-VI semiconductors: A first-principles prediction. *Phys. Rev. B*, 2015. **92**(11).

39. P. Tsipas, et. al., Evidence for graphite-like hexagonal AlN nanosheets epitaxially grown on single crystal Ag(111). *Appl. Phys. Lett.*, 2013. **103**(25).
40. X. Deng, D.C. Sorescu, and J. Lee, Single-layer ZnS supported on Au(111): A combined XPS, LEED, STM and DFT study. *Surf. Sci.*, 2017. **658**: p. 9-14.
41. C. Tusche, H.L. Meyerheim, and J. Kirschner, Observation of depolarized ZnO(0001) monolayers: formation of unreconstructed planar sheets. *Phys. Rev. Lett.*, 2007. **99**(2): p. 026102.
42. X. Deng, et al., Growth of single- and bilayer ZnO on Au(111) and interaction with Copper. *J. of Phys. Chem. C*, 2013. **117**(21): p. 11211-11218.
43. Q. Pan, et al., Reactivity of ultra-thin ZnO films supported by Ag(111) and Cu(111): A comparison to ZnO/Pt(111). *Catal. Lett.*, 2014. **144**(4): p. 648-655.
44. A. Continenza, R.M. Wentzcovitch, and A.J. Freeman, Theoretical investigation of graphitic BeO. *Phys. Rev. B Condens Matter*, 1990. **41**(6): p. 3540-3544.
45. A. Lichanot, et al., Theoretical study of the stability of beryllium oxide (110) and (001) surfaces in dense wurtzite and layered graphitic phases. *Phys. Rev. B Condens Matter*, 1995. **52**(24): p. 17480-17490.
46. P.B. Sorokin, A.S. Fedorov, and L.A. Chernozatonskiĭ, Structure and properties of BeO nanotubes. *Phys. of the Solid State*, 2006. **48**(2): p. 398-401.
47. H.L. Zhuang and R.G. Hennig, Computational identification of single-layer CdO for electronic and optical applications. *Appl. Phys. Lett.*, 2013. **103**(21).
48. T.V. Afanasieva, et al., Honeycomb BeO monolayer on the Mo(112) surface: LEED and DFT study. *Appl. Surf. Sci.*, 2018. **428**: p. 815-818.
49. T.V. Afanasieva, et al., Coadsorbed oligolayers of beryllium and oxygen on molybdenum (1 1 2) surface: Formation and chemical composition, atomic structure and evaporation. *Surf. Sci.*, 2019. **682**: p. 14-24.
50. L. Wang, et al., Synthesis of honeycomb-structured beryllium oxide via graphene liquid cells. *Angew. Chem. Int. Ed. Engl.*, 2020. **59**(36): p. 15734-15740.
51. F. Cheng, et al., Epitaxial growth of optically thick, single crystalline silver films for plasmonics. *ACS Appl. Mater. Interfaces*, 2019. **11**: p. 5.
52. S. Baumann, et al., Measuring the three-dimensional structure of ultrathin insulating films at the atomic scale. *ACS Nano*, 2015. **8**: p. 5.
53. I. Sebastian and S. Neddermeyer, Scanning tunneling microscopy on the atomic and electronic structure of CoO thin films on Ag(100). *Surf. Sci.*, 2000. **454-456**: p. 7.
54. W. Hebenstreit, et al., Atomic resolution by STM on ultra-thin films of alkali halides: experiment and local density calculations. *Surf. Sci.* 1999. **424**: p. 8.
55. A. Malashevich, E.I. Altman, and S. Ismail-Beigi, Imaging the buried MgO/Ag interface: Formation mechanism of the STM contrast. *Phys. Rev. B*, 2014. **90**(16).
56. K. Hermann, Periodic overlayers and moire patterns: theoretical studies of geometric properties. *J. Phys. Condens Matter*, 2012. **24**(31): p. 314210.
57. J. Baima, et al., Beryllium oxide nanotubes and their connection to the flat monolayer. *J. of Phys. Chem. C*, 2013. **117**(24): p. 12864-12872.

58. M. Shahrokhi and C. Leonard, Quasi-particle energies and optical excitations of wurtzite BeO and its nanosheet. *J. of All. and Comp.*, 2016. **682**: p. 254-262.
59. S. Valedbagi, et al., Ab initio calculations of electronic and optical properties of BeO nanosheet. *Elec. Mater. Lett.*, 2014. **10**(1): p. 5-11.
60. W. Wu, et al., Electronic and magnetic properties and structural stability of BeO sheet and nanoribbons. *ACS Appl. Mater. Interfaces*, 2011. **3**(12): p. 4787-95.
61. S. Zhang, et al., Defect structure of localized excitons in a WSe₂ Monolayer. *Phys. Rev. Lett.*, 2017. **119**(4): p. 046101.
62. C. Zhang, et al., Strain distributions and their influence on electronic structures of WSe₂-MoS₂ laterally strained heterojunctions. *Nat. Nanotechnol.*, 2018. **13**(2): p. 152-158.
63. J. Park, et al., Modification of surface-state dispersion upon Xe adsorption: A scanning tunneling microscope study. *Phys. Rev. B*, 2000. **62**.
64. Q. Zhang, et al., Tuning band gap and work function modulations in monolayer hBN/Cu(111) heterostructures with moire patterns. *ACS Nano*, 2018. **12**(9): p. 9355-9362.
65. S. Joshi, et al., Boron nitride on Cu(111): an electronically corrugated monolayer. *Nano. Lett.*, 2012. **12**(11): p. 5821-8.
66. Q. Zhang, et al., Bandgap renormalization and work function tuning in MoSe₂/hBN/Ru(0001) heterostructures. *Nat. Comm.*, 2016. **7**: p. 13843.
67. F. Schulz, et al., Epitaxial hexagonal boron nitride on Ir(111): A work function template. *Phys. Rev. B*, 2014. **89**(23).
68. H. Dil, et al., Surface trapping of atoms and molecules with dipole rings. *Science*, 2008. **319**: p. 3.
69. S. Manzeli, et al., 2D transition metal dichalcogenides. *Nat. Rev. Mater.*, 2017. **2**(8).
70. S. Wang, A. Robertson, and J.H. Warner, Atomic structure of defects and dopants in 2D layered transition metal dichalcogenides. *Chem. Soc. Rev.*, 2018. **47**: p. 20.
71. Z. Lin, et al., Defect engineering of two-dimensional transition metal dichalcogenides. *2D Mater.*, 2016. **3**(2).
72. Q. Liang, et al., Defect engineering of two-dimensional transition-metal dichalcogenides: applications, challenges, and opportunities. *ACS Nano*, 2021. **15**(2): p. 2165-2181.
73. W. Zhou, et al., Intrinsic structural defects in monolayer molybdenum disulfide. *Nano. Lett.*, 2013. **13**(6): p. 2615-22.
74. B. Schuler, et al., How substitutional point defects in two-dimensional WS₂ induce charge localization, spin-orbit splitting, and strain. *ACS Nano*, 2019. **13**(9): p. 10520-10534.
75. P. Vancso, et al., The intrinsic defect structure of exfoliated MoS₂ single layers revealed by scanning tunneling microscopy. *Sci. Rep.*, 2016. **6**: p. 29726.
76. S. Barja, et al., Identifying substitutional oxygen as a prolific point defect in monolayer transition metal dichalcogenides. *Nat. Comm.*, 2019. **10**(1): p. 3382.
77. D. Edelberg, et al., Approaching the intrinsic limit in transition metal diselenides via point defect control. *Nano. Lett.*, 2019. **19**(7): p. 4371-4379.

78. J. Hong, et al., Exploring atomic defects in molybdenum disulphide monolayers. *Nat. Comm.*, 2015. **6**: p. 6293.
79. X. Liu, et al., Point defects and grain boundaries in rotationally commensurate MoS₂ on epitaxial graphene. *J. of Phys. Chem. C*, 2016. **120**(37): p. 20798-20805.
80. H.-P. Komsa, et al., From point to extended defects in two-dimensional MoS₂: Evolution of atomic structure under electron irradiation. *Phys. Rev. B*, 2013. **88**(3).
81. J.-Y. Noh, H. Kim, and Y.-S. Kim, Stability and electronic structures of native defects in single-layer MoS₂. *Phys. Rev. B*, 2014. **89**(20).
82. H.-P. Komsa and A.V. Krasheninnikov, Native defects in bulk and monolayer MoS₂ from first principles. *Phys. Rev. B*, 2015. **91**(12).
83. S. Haldar, et al., Systematic study of structural, electronic, and optical properties of atomic-scale defects in the two-dimensional transition metal dichalcogenides MX₂ (M = Mo, W; X = S, Se, Te). *Phys. Rev. B*, 2015. **92**(23).
84. W.-F. Li, C. Fang, and M.A. van Huis, Strong spin-orbit splitting and magnetism of point defect states in monolayer WS₂. *Phys. Rev. B*, 2016. **94**(19).
85. S. Salehi and A. Saffarzadeh, Atomic defect states in monolayers of MoS₂ and WS₂. *Surf. Sci.*, 2016. **651**: p. 7.
86. W. Hu, et al., Synergetic effect of substitutional dopants and sulfur vacancy in modulating the ferromagnetism of MoS₂ monolayers. *ACS Appl. Mater. Interfaces*, 2019. **11**(34): p. 31155-31161.
87. S. Tongay, et al., Defects activated photoluminescence in two-dimensional semiconductors: interplay between bound, charged, and free excitons. *Sci. Rep.*, 2013. **3**: p. 2657.
88. T.Y. Jeong, et al., Spectroscopic studies of atomic defects and bandgap renormalization in semiconducting monolayer transition metal dichalcogenides. *Nat. Comm.*, 2019. **10**(1): p. 3825.
89. M.H. Naik and M. Jain, Substrate screening effects on the quasiparticle band gap and defect charge transition levels in MoS₂. *Phys. Rev. Mater.*, 2018. **2**(8).
90. D. Liu, et al., Sulfur vacancies in monolayer MoS₂ and its electrical contacts. *Appl. Phys. Lett.*, 2013. **103**(18).
91. M.A. Khan, et al., Electronic and optical properties of vacancy defects in single-layer transition metal dichalcogenides. *Phys. Rev. B*, 2017. **95**(24).
92. S. Yuan, et al., Effect of point defects on the optical and transport properties of MoS₂ and WS₂. *Phys. Rev. B*, 2014. **90**(4).
93. M. Pandey, et al., Defect tolerant monolayer transition metal dichalcogenides. *Nano. Lett.*, 2016. **16**: p. 6.
94. H. Qiu, et al., Hopping transport through defect-induced localized states in molybdenum disulphide. *Nat. Comm.*, 2013. **4**: p. 2642.
95. Z. Chu, et al., Unveiling defect-mediated carrier dynamics in monolayer semiconductors by spatiotemporal microwave imaging. *Proc. Natl. Acad. Sci, USA*, 2020. **117**(25): p. 13908-13913.
96. X. Wang, et al., Single-atom vacancy defect to trigger high-efficiency hydrogen evolution of MoS₂. *J. Am. Chem. Soc.*, 2020. **142**(9): p. 4298-4308.

97. J. Xie, et al., Defect-rich MoS₂ ultrathin nanosheets with additional active edge sites for enhanced electrocatalytic hydrogen evolution. *Adv. Mater.*, 2013. **25**(40): p. 5807-13.
98. H. Li, et al., Activating and optimizing MoS₂ basal planes for hydrogen evolution through the formation of strained sulphur vacancies. *Nat. Mater.*, 2016. **15**(3): p. 364.
99. D. Voiry, et al., The role of electronic coupling between substrate and 2D MoS₂ nanosheets in electrocatalytic production of hydrogen. *Nat. Mater.*, 2016. **15**(9): p. 1003-9.
100. J. Peto, et al., Spontaneous doping of the basal plane of MoS₂ single layers through oxygen substitution under ambient conditions. *Nat. Chem.*, 2018. **10**(12): p. 1246-1251.
101. Y. Wang, et al., Spin-valley locking effect in defect states of monolayer MoS₂. *Nano. Lett.*, 2020. **20**(3): p. 2129-2136.
102. P.K. Chow, et al., Defect-induced photoluminescence in monolayer semiconducting transition metal dichalcogenides. *ACS Nano*, 2015. **9**: p. 8.
103. V. Carozo, et al., Optical identification of sulfur vacancies: bound excitons at the edges of monolayer tungsten disulfide. *Sci. Adv.*, 2017. **3**.
104. Y.C. Lin, et al., Three-fold rotational defects in two-dimensional transition metal dichalcogenides. *Nat. Comm.*, 2015. **6**: p. 6736.
105. H.P. Komsa, et al., Two-dimensional transition metal dichalcogenides under electron irradiation: defect production and doping. *Phys. Rev. Lett.*, 2012. **109**(3): p. 035503.
106. J. Zhao, et al., Chain Vacancies in 2D Crystals. *Small*, 2017. **13**(1).
107. W.H. Blades, et al., Thermally induced defects on WSe₂. *J. of Phys. Chem. C*, 2020. **124**(28): p. 15337-15346.
108. M. Liu, et al., Temperature-triggered sulfur vacancy evolution in monolayer MoS₂ /Graphene heterostructures. *Small*, 2017. **13**(40).
109. B. Schuler, et al., Large spin-orbit splitting of deep in-gap defect states of engineered sulfur vacancies in monolayer WS₂. *Phys. Rev. Lett.*, 2019. **123**(7): p. 076801.
110. X. Zhou, et al., Periodic modulation of the doping level in striped MoS₂ superstructures. *ACS Nano*, 2016. **10**(3): p. 3461-8.
111. M. Mahjouri-Samani, et al., Tailoring vacancies far beyond intrinsic levels changes the carrier type and optical response in monolayer MoSe_{2-x} crystals. *Nano. Lett.*, 2016. **16**(8): p. 5213-20.
112. C. Gao, et al., Synergistic vacancy defects and mechanical strain for the modulation of the mechanical, electronic and optical properties of monolayer tungsten disulfide. *Phys. Chem. Chem. Phys.*, 2021. **23**(10): p. 6298-6308.
113. D.S. Wang, et al., Hybridized defects in solid-state materials as artificial molecules. 2020. **arXiv:2012.09187**.
114. J.K. Huang, et al., Large-area synthesis of highly crystalline WSe₂ monolayers and device applications. *ACS Nano*, 2014. **1**: p. 923-930.

115. Y.H. Chang, et al., Monolayer MoSe₂ grown by chemical vapor deposition for fast photodetection. *ACS Nano*, 2014. **8**: p. 8582-8590.
116. S. McDonnell, et al., Defect-dominated doping and contact resistance in MoS₂. *ACS Nano*, 2014. **8**(3): p. 8.
117. C.P. Lu, et al., Bandgap, mid-gap states, and gating effects in MoS₂. *Nano. Lett.*, 2014. **14**(8): p. 4628-33.
118. Y. Chen, et al., Tuning electronic structure of single layer MoS₂ through defect and interface engineering. *ACS Nano*, 2018. **12**(3): p. 2569-2579.
119. S. Mammadov, et al., Work function of graphene multilayers on SiC(0001). *2D Mater.*, 2017. **4**(1).
120. M.M. Ugeda, et al., Giant bandgap renormalization and excitonic effects in a monolayer transition metal dichalcogenide semiconductor. *Nat. Mater.*, 2014. **13**(12): p. 1091-5.
121. A. Raja, et al., Dielectric disorder in two-dimensional materials. *Nat. Nanotechnol.*, 2019. **14**(9): p. 832-837.
122. R.M. Feenstra and J.A. Stroscio, Tunneling spectroscopy of the GaAs(110) surface. *J. Vac.Sci. Technol. B*, 1987. **5**(4): p. 6.
123. K. Teichmann, et al., Controlled charge switching on a single donor with a scanning tunneling microscope. *Phys. Rev. Lett.*, 2008. **101**(7): p. 076103.
124. H. Schmidt, F. Giustiniano, and G. Eda, Electronic transport properties of transition metal dichalcogenide field-effect devices: surface and interface effects. *Chem. Soc. Rev.*, 2015. **44**(21): p. 7715-36.
125. A.V. Kolobov and J. Tominaga, *Two-dimensional transition-metal dichalcogenides*. Springer Ser. Materials. 2018: SPRINGER.
126. M. Chhowalla, et al., The chemistry of two-dimensional layered transition metal dichalcogenide nanosheets. *Nat. Chem.*, 2013. **5**(4): p. 263-75.
127. R. Hoffman, J.M. Howell, and A.R. Rossi, Bicapped tetrahedral, trigonal prismatic, and octahedral alternatives in main and transition group six-coordination. *J. of the Am. Chem. Soc.*, 1975. **98**: p. 8.
128. A. Kormányos, et al., k·p theory for two-dimensional transition metal dichalcogenide semiconductors. *2D Mater.*, 2015. **2**(2).
129. G.-B. Liu, et al., Three-band tight-binding model for monolayers of group-VIB transition metal dichalcogenides. *Phys. Rev. B*, 2013. **88**(8).
130. D. Xiao, et al., Coupled spin and valley physics in monolayers of MoS₂ and other group-VI dichalcogenides. *Phys. Rev. Lett.*, 2012. **108**(19): p. 196802.
131. Z.Y. Zhu, Y.C. Cheng, and U. Schwingenschlögl, Giant spin-orbit-induced spin splitting in two-dimensional transition-metal dichalcogenide semiconductors. *Phys. Rev. B*, 2011. **84**(15).
132. Y. Ma, et al., Metallic twin grain boundaries embedded in MoSe₂ monolayers grown by molecular beam epitaxy. *ACS Nano*, 2017. **11**(5): p. 5130-5139.
133. M.H. Chiu, et al., Determination of band alignment in the single-layer MoS₂/WSe₂ heterojunction. *Nat. Comm.*, 2015. **6**: p. 7666.

134. P. Rivera, et al., Observation of long-lived interlayer excitons in monolayer MoSe₂-WSe₂ heterostructures. *Nat. Comm.*, 2015. **6**: p. 6242.
135. S. Tongay, et al., Tuning interlayer coupling in large-area heterostructures with CVD-grown MoS₂ and WS₂ monolayers. *Nano. Lett.*, 2014. **14**(6): p. 3185-90.
136. Y. Gong, et al., Vertical and in-plane heterostructures from WS₂/MoS₂ monolayers. *Nat. Mater.*, 2014. **13**(12): p. 1135-42.
137. C. Zhang, et al., Interlayer couplings, moiré patterns, and 2D electronic superlattices in MoS₂/WSe₂ hetero-bilayers. *Sci. Adv.*, 2017. **3**.
138. Y.-H. Chu, et al., Atomic scale depletion region at one dimensional MoSe₂-WSe₂ heterointerface. *Appl. Phys. Lett.*, 2018. **113**(24).
139. C. Huang, et al., Lateral heterojunctions within monolayer MoSe₂-WSe₂ semiconductors. *Nat. Mater.*, 2014. **13**(12): p. 1096-101.
140. M.Y. Li, et al., Epitaxial growth of a monolayer WSe₂-MoS₂ lateral p-n junction with an atomically sharp interface. *Science*, 2015. **349**(6247): p. 4.
141. C. Gong, et al., Band alignment of two-dimensional transition metal dichalcogenides: application in tunnel field effect transistors. *Appl. Phys. Lett.*, 2013. **103**.
142. A. Allain, et al., Electrical contacts to two-dimensional semiconductors. *Nat. Mater.*, 2015. **14**(12): p. 1195-205.
143. M. Dendzik, et al., Substrate-induced semiconductor to-metal transition in monolayer WS₂. *Phys. Rev. B*, 2017. **96**(23).
144. A. Bruix, et al., Single-layer MoS₂ on Au(111): Band gap renormalization and substrate interaction. *Phys. Rev. B*, 2016. **93**(16).
145. S. Ulstrup, et al., Nanoscale mapping of quasiparticle band alignment. *Nat. Comm.*, 2019. **10**(1): p. 3283.
146. T. Le Quang, et al., Scanning tunneling spectroscopy of van der Waals graphene/semiconductor interfaces: absence of Fermi level pinning. *2D Materials*, 2017. **4**(3).
147. H.-P. Komsa and A.V. Krasheninnikov, Effects of confinement and environment on the electronic structure and exciton binding energy of MoS₂ from first principles. *Phys. Rev. B*, 2012. **86**(24).
148. A.V. Stier, et al., Probing the influence of dielectric environment on excitons in monolayer WSe₂: Insight from high magnetic fields. *Nano. Lett.*, 2016. **16**(11): p. 7054-7060.
149. Y. Xu, et al., Creation of moire bands in a monolayer semiconductor by spatially periodic dielectric screening. *Nat. Mater.*, 2021.
150. C. Steinke, T.O. Wehling, and M. Rösner, Coulomb-engineered heterojunctions and dynamical screening in transition metal dichalcogenide monolayers. *Phys. Rev. B*, 2020. **102**(11).
151. Y. Cho and T.C. Berkelbach, Environmentally sensitive theory of electronic and optical transitions in atomically thin semiconductors. *Phys. Rev. B*, 2018. **97**(4).
152. D.Y. Qiu, F.H. da Jornada, and S.G. Louie, Screening and many-body effects in two-dimensional crystals: Monolayer MoS₂. *Phys. Rev. B*, 2016. **93**(23).

153. J. Ryou, et al., Monolayer MoS₂ bandgap modulation by dielectric environments and tunable bandgap transistors. *Sci. Rep.*, 2016. **6**: p. 29184.
154. M. Rosner, et al., Two-dimensional heterojunctions from nonlocal manipulations of the interactions. *Nano. Lett.*, 2016. **16**(4): p. 2322-7.
155. L. Waldecker, et al., Rigid band shifts in two-dimensional semiconductors through external dielectric screening. *Phys. Rev. Lett.*, 2019. **123**(20): p. 206403.
156. A. Raja, et al., Coulomb engineering of the bandgap and excitons in two-dimensional materials. *Nat. Comm.*, 2017. **8**: p. 15251.
157. M.I.B. Utama, et al., A dielectric-defined lateral heterojunction in a monolayer semiconductor. *Nat. Elec.*, 2019. **2**(2): p. 60-65.
158. S.Y. Lee, et al., Large work function modulation of monolayer MoS₂ by ambient gases. *ACS Nano*, 2016. **10**(6): p. 6100-7.
159. M. Kang, et al., Universal mechanism of band-gap engineering in transition-metal dichalcogenides. *Nano. Lett.*, 2017. **17**(3): p. 1610-1615.
160. Z. Song, et al., Electronic properties of a 1D intrinsic/p-doped heterojunction in a 2D transition metal dichalcogenide semiconductor. *ACS Nano*, 2017. **11**(9): p. 9128-9135.
161. M. Corso, et al., Boron nitride nanomesh. *Science*, 2004. **303**: p. 4.
162. A. Goriachko, et al., Self-assembly of a hexagonal boron nitride nanomesh on Ru(0001). *Langmuir*, 2007. **23**: p. 2928-2931.
163. R. Laskowski and P. Blaha, Ab initio study of h-BN nanomeshes on Ru(001), Rh(111), and Pt(111). *Phys. Rev. B*, 2010. **81**(7).
164. T. Brugger, et al., Nanotexture switching of single-layer hexagonal boron nitride on rhodium by intercalation of hydrogen atoms. *Angew. Chem. Int. Ed. Engl.*, 2010. **49**(35): p. 6120-4.
165. A. Dong, et al., Factors controlling the CO intercalation of h-BN overlayers on Ru(0001). *Phys. Chem. Chem. Phys.*, 2016. **18**(35): p. 24278-84.
166. M.L. Ng, et al., Reversible modification of the structural and electronic properties of a boron nitride monolayer by CO intercalation. *Chemphyschem*, 2015. **16**(5): p. 923-7.
167. M. Wei, et al., Hydrogen intercalation of graphene and boron nitride monolayers grown on Pt(111). *Topics in Catal.*, 2015. **59**(5-7): p. 543-549.
168. Y. Yang, et al., Stability of BN/metal interfaces in gaseous atmosphere. *Nano Research*, 2014. **8**(1): p. 227-237.
169. Nipane, A., et al., Electrostatics of lateral p-n junctions in atomically thin materials. *J. of Appl. Phys.*, 2017. **122**(19).
170. H. Ilatikhameneh, et al., Dramatic Impact of Dimensionality on the Electrostatics of P-N Junctions and Its Sensing and Switching Applications. *IEEE Trans. on Nanotech.*, 2018. **17**(2): p. 293-298.
171. G. Kresse and J. Furthmuller, Efficiency of ab-initio total energy calculations for metals and semiconductors using a plane-wave basis set. *Comp. Mater. Sci.*, 1996. **6**: p. 15-50.

172. G. Kresse and J. Furthmuller, Efficient iterative schemes for ab initio total-energy calculations using a plane-wave basis set. *Phys. Rev. B*, 1996. **54**(16).
173. G. Kresse and D. Joubert, From ultrasoft pseudopotentials to the projector augmented-wave method. *Phys. Rev. B*, 1999. **59**(3).
174. P.E. Blochl, Projector augmented-wave method. *Phys. Rev. B Condens Matter*, 1994. **50**(24): p. 17953-17979.
175. J. Klimeš, D.R. Bowler, and A. Michaelides, Van der Waals density functionals applied to solids. *Phys. Rev. B*, 2011. **83**(19).
176. J.P. Perdew, K. Burke, and M. Ernzerhof, Generalized gradient approximation made simple. *Phys. Rev. Lett.*, 1996. **77**(18).
177. P. Giannozzi, et al., QUANTUM ESPRESSO: a modular and open-source software project for quantum simulations of materials. *J. Phys. Condens Matter*, 2009. **21**(39): p. 395502.